Seismic and Potential Field Constraints on Upper Crustal Architecture of Inner Bering Shelf, Offshore Southwestern Alaska

Rajesh Vayavur[1] and Andrew John Calvert[2]

[1]Laurentian University
[2]Simon Fraser University

December 3, 2023

Abstract

Southwestern Alaska encompasses a group of fault-bounded tectonostratigraphic terranes that were accreted to North America during the Mesozoic and Paleogene. To characterize the offshore extension of these terranes and several significant faults identified onshore, we reprocessed three intersecting multichannel deep seismic reflection profiles totaling ~750 line-km that were shot by the R/V Ewing across part of the inner Bering continental shelf in 1994. Since the uppermost seismic section is often contaminated by high amplitude water layer multiples from the hard and shallow seafloor, the migrated reflection images are supplemented with high-resolution P wave velocity models derived by traveltime tomography of the recorded first-arrivals to depths of up to 2000 m. Additionally, other geophysical datasets such as well logs, ship-board gravity, ship-board magnetics, satellite-altimetry gravity and air-borne magnetics are also incorporated into an integrated regional interpretation. We delineate the offshore extension of the major mapped geological elements, including the Togiak-Tikchik fault, East Kulukak fault, Chilchitna fault, Lake Clarke fault, Togiak terrane, Goodnews terrane, Peninsular terrane, Northern and Southern Kahiltna flysch deposits, and the Regional Suture Zone. We interpret the offshore Togiak-Tikichik fault to be a terrane bounding fault separating the Togiak terrane and Goodnews terrane. We also locate the offshore boundaries of the Regional Suture Zone using satellite gravity anomaly and air-borne magnetic data. Furthermore, we suggest that the sedimentary fill in the graben-like features offshore, as identified by seismic tomographic velocity models, is constituted by the deposits of Northern and Southern Kahiltna flysch.

Hosted file

980457_0_art_file_11625809_s4wx1m.docx available at https://authorea.com/users/704729/articles/690157-seismic-and-potential-field-constraints-on-upper-crustal-architecture-of-inner-bering-shelf-offshore-southwestern-alaska

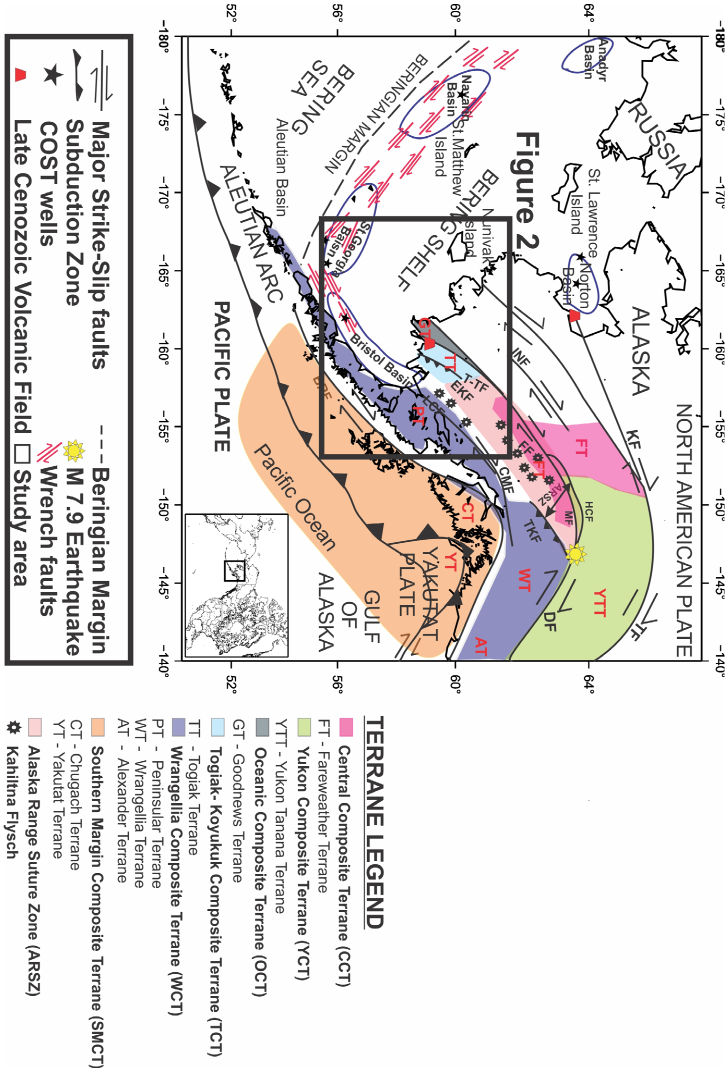
Figure 2
RUSSIA
ALASKA
NORTH AMERICAN PLATE
BERING SHELF
BERING SEA
BERINGIAN MARGIN
Aleutian Basin
ALEUTIAN ARC
PACIFIC PLATE
Pacific Ocean
YAKUTAT PLATE
GULF OF ALASKA
St. Lawrence Island
St. Matthew Island
Nunivak Island
Norton Basin
Anadyr Basin
Navarin Basin
St. George Basin
Bristol Basin
FT
YTT
WT
AT
CT
YT
PT
TT
GT
KF
TF
DF
TKF
CMF
INF
EKF
HCF
MF
ARSZ
Major Strike-Slip faults
Subduction Zone
COST wells
Late Cenozoic Volcanic Field
Beringian Margin
M 7.9 Earthquake
Wrench faults
Study area
TERRANE LEGEND
Central Composite Terrane (CCT)
FT - Fareweather Terrane
Yukon Composite Terrane (YCT)
YTT - Yukon Tanana Terrane
Oceanic Composite Terrane (OCT)
GT - Goodnews Terrane
Toglak- Koyukuk Composite Terrane (TCT)
TT - Togiak Terrane
Wrangellia Composite Terrane (WCT)
PT - Peninsular Terrane
WT - Wrangellia Terrane
AT - Alexander Terrane
Southern Margin Composite Terrane (SMCT)
CT - Chugach Terrane
YT - Yakutat Terrane
Alaska Range Suture Zone (ARSZ)
Kahiltna Flysch

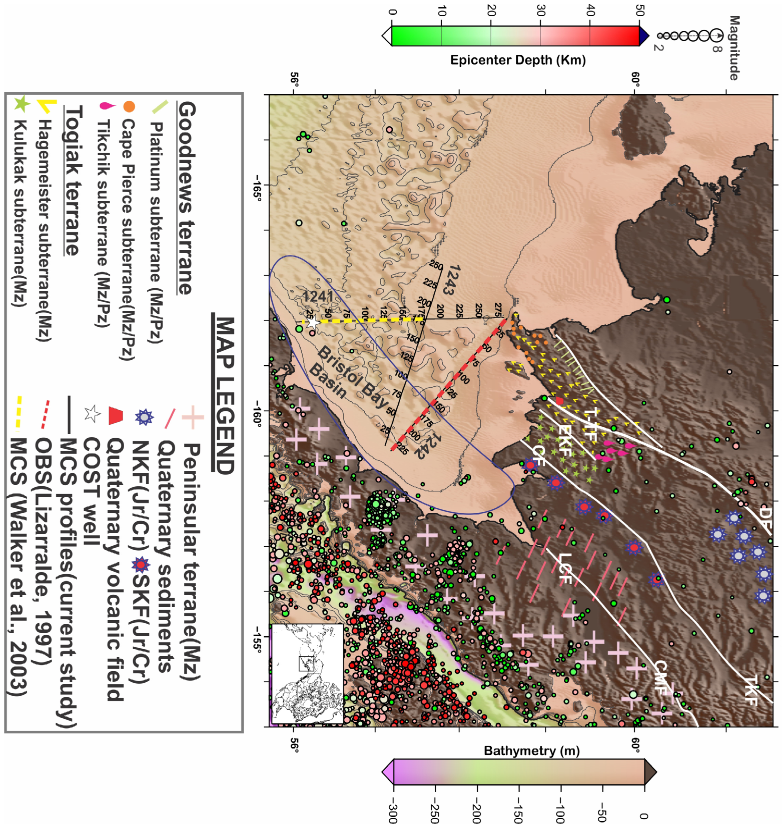

Magnitude
8
2
Epicenter Depth (Km)
0
10
20
30
40
50
Bathymetry (m)
0
-50
-100
-150
-200
-250
-300
-165°
-160°
-155°
56°
60°
1243
1242
1241
Bristol Bay Basin
DF
TKF
CMF
LGF
EKF
TLF
CF
MAP LEGEND
Goodnews terrane
Platinum subterrane (Mz/Pz)
Cape Pierce subterrane(Mz/Pz)
Tikchik subterrane (Mz/Pz)
Togiak terrane
Hagemeister subterrane(Mz)
Kulukak subterrane(Mz)
Peninsular terrane(Mz)
Quaternary sediments
NKF(Jr/Cr) SKF(Jr/Cr)
Quaternary volcanic field
COST well
MCS profiles(current study)
OBS(Lizarralde, 1997)
MCS (Walker et al., 2003)

2

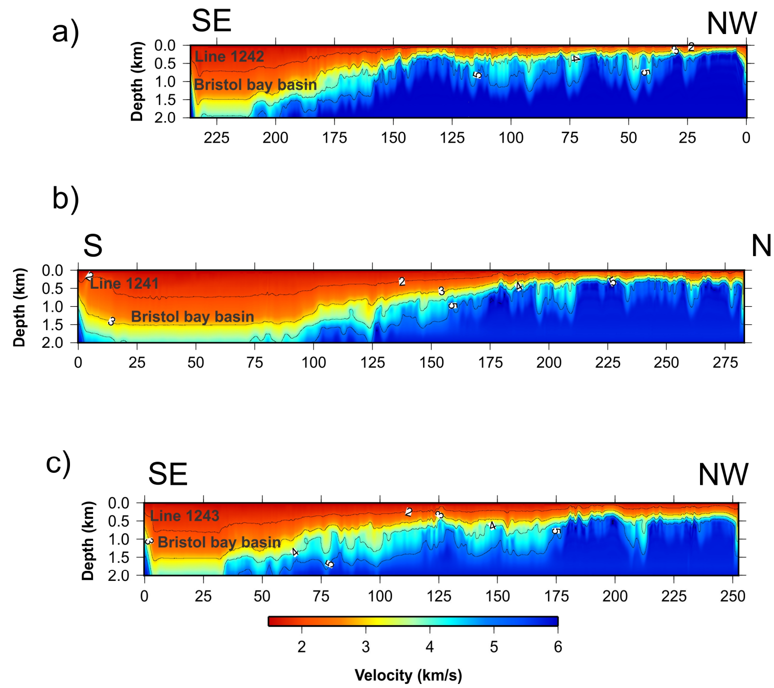

a)
SE
NW
Line 1242
Bristol bay basin
Depth (km)
b)
S
N
Line 1241
Bristol bay basin
Depth (km)
c)
SE
NW
Line 1243
Bristol bay basin
Depth (km)
Velocity (km/s)

3

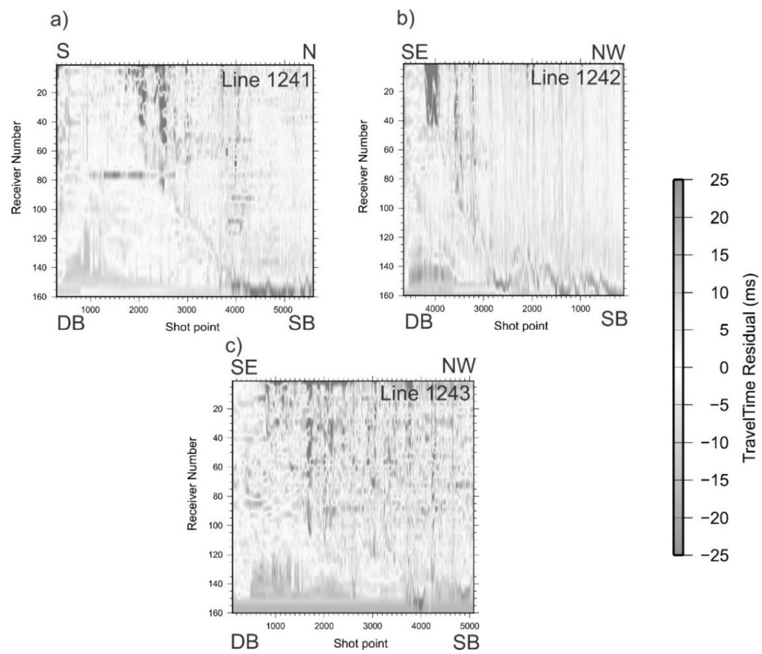

a)
S
N
Line 1241
Receiver Number
Shot point
DB
SB
b)
SE
NW
Line 1242
Receiver Number
Shot point
DB
SB
c)
SE
NW
Line 1243
Receiver Number
Shot point
DB
SB
TravelTime Residual (ms)

4

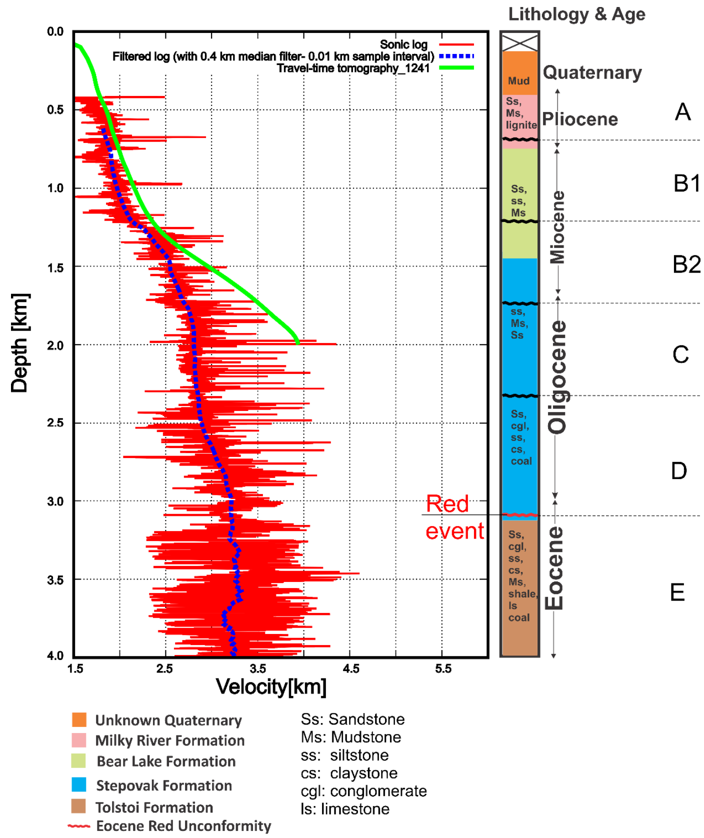
Lithology & Age
Sonic log
Filtered log (with 0.4 km median filter- 0.01 km sample interval)
Travel-time tomography_1241
Depth [km]
Velocity[km]
0.0
0.5
1.0
1.5
2.0
2.5
3.0
3.5
4.0
1.5
2.5
3.5
4.5
5.5
Red event
Mud
Ss, Ms, lignite
Ss, ss, Ms
ss, Ms, Ss
Ss, cgl, ss, cs, coal
Ss, cgl, ss, cs, Ms, shale, ls coal
Quaternary
Pliocene
Miocene
Oligocene
Eocene
A
B1
B2
C
D
E
Unknown Quaternary
Milky River Formation
Bear Lake Formation
Stepovak Formation
Tolstoi Formation
Eocene Red Unconformity
Ss: Sandstone
Ms: Mudstone
ss: siltstone
cs: claystone
cgl: conglomerate
ls: limestone

5

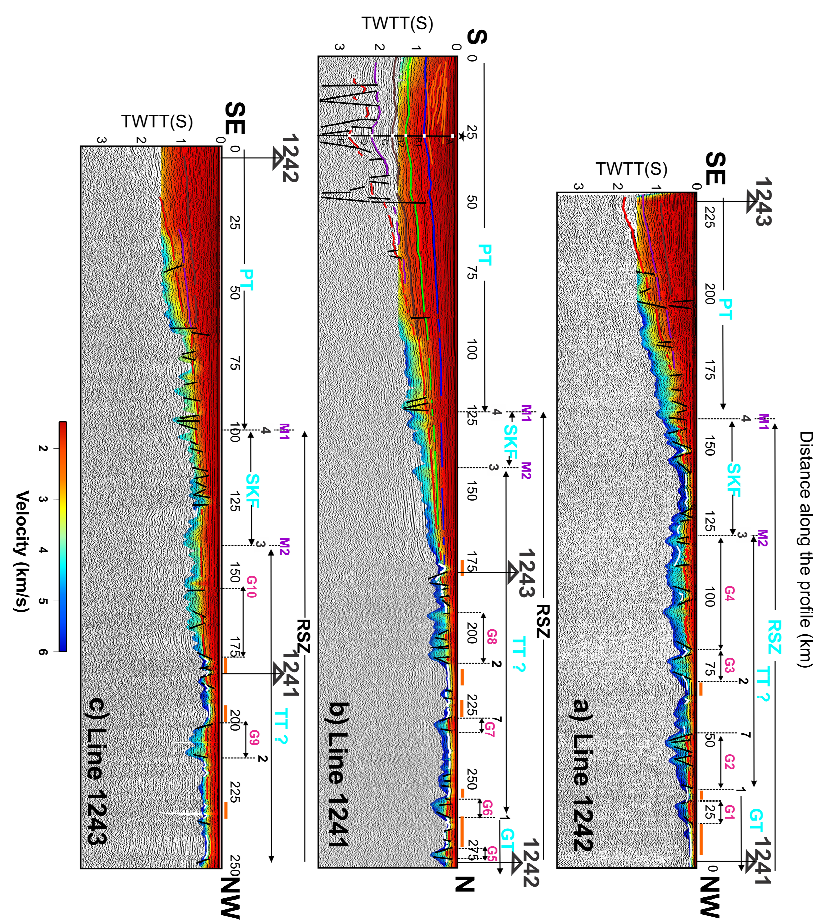
a) Line 1242
b) Line 1241
c) Line 1243
Distance along the profile (km)
TWTT(S)
Velocity (km/s)
SE
NW
S
N
PT
SKF
RSZ
TT ?
GT
M1
M2
G1
G2
G3
G4
G5
G6
G7
G8
G9
G10
1241
1242
1243

6

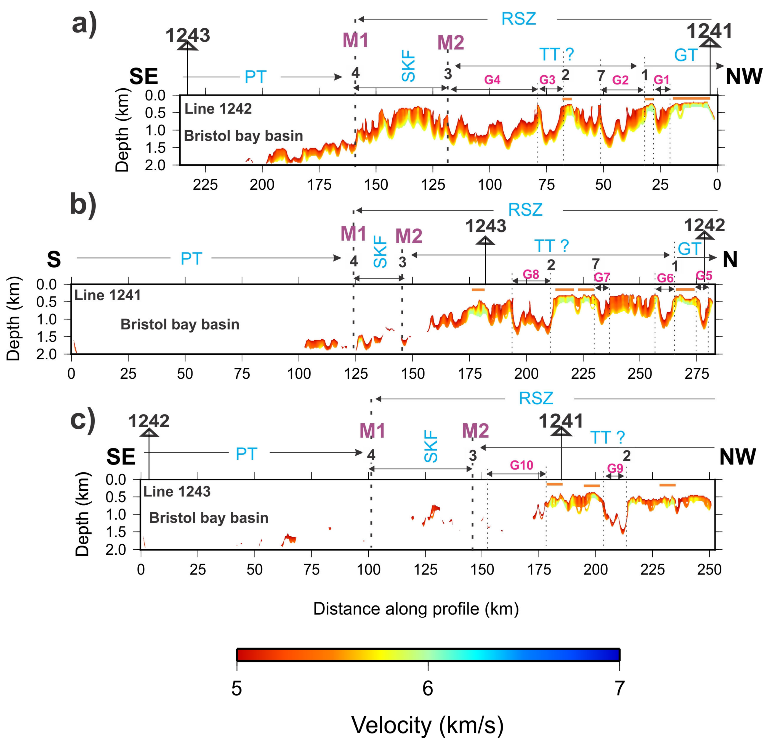

a)
b)
c)
Line 1242
Line 1241
Line 1243
Bristol bay basin
RSZ
PT
TT ?
GT
SKF
M1
M2
SE
NW
S
N
Depth (km)
Distance along profile (km)
Velocity (km/s)

7

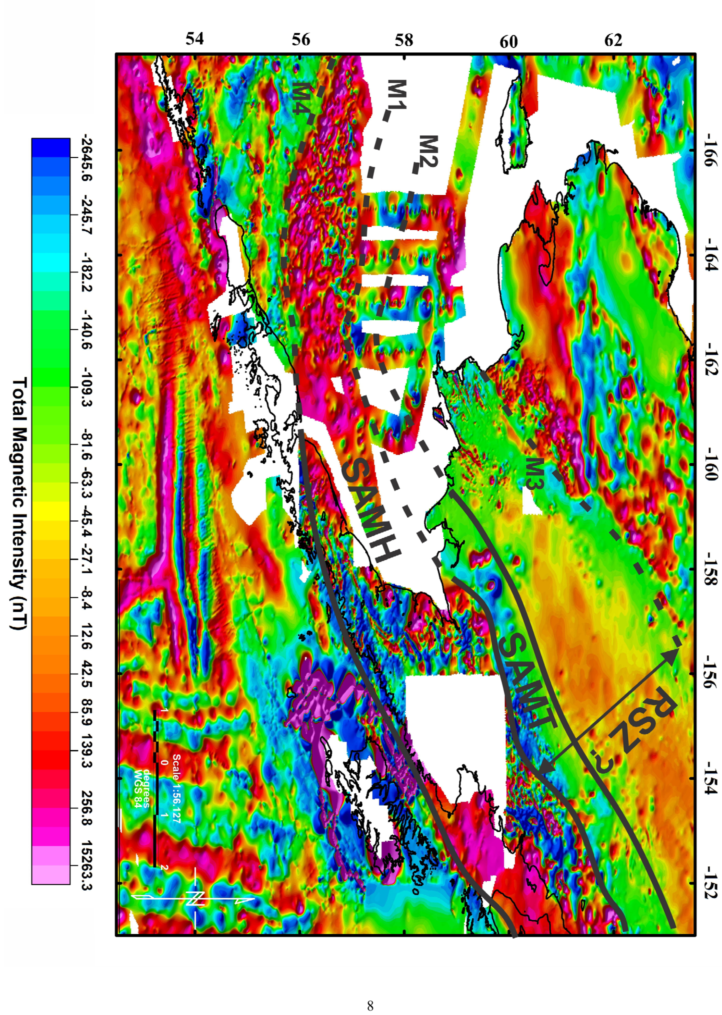
54
56
58
60
62
-166
-164
-162
-160
-158
-156
-154
-152
M1
M2
M3
M4
SAMH
SAMT
RSZ ?
Total Magnetic Intensity (nT)
-2645.6
-245.7
-182.2
-140.6
-109.3
-81.6
-63.3
-45.4
-27.1
-8.4
12.6
42.5
85.9
139.3
266.8
15263.3
8

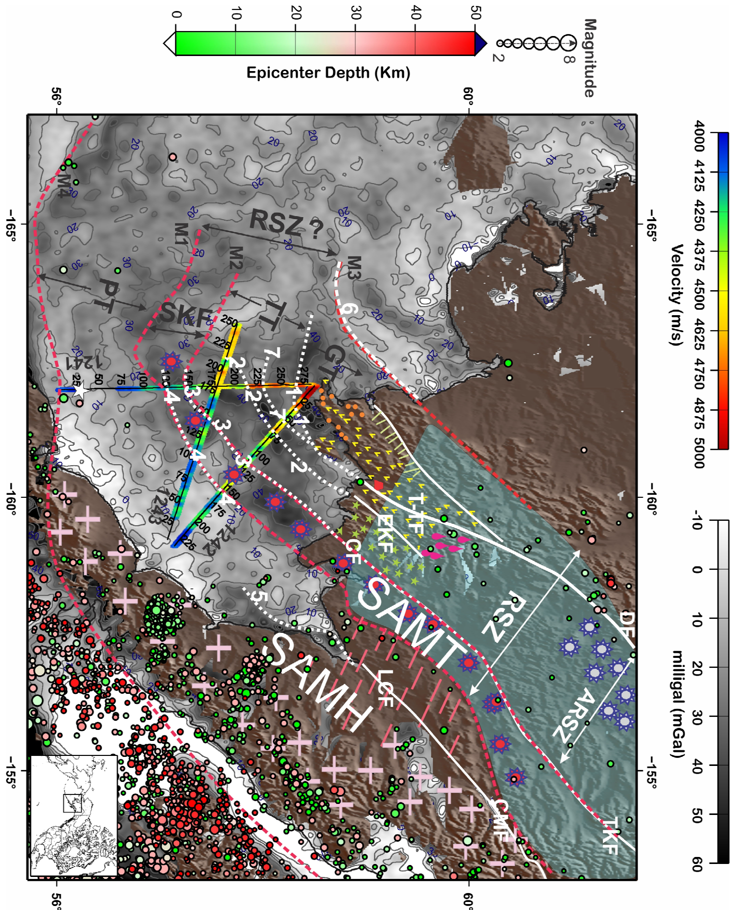

Magnitude
2
8
Epicenter Depth (Km)
0
10
20
30
40
50
Velocity (m/s)
4000 4125 4250 4375 4500 4625 4750 4875 5000
milligal (mGal)
-10
0
10
20
30
40
50
60
56°
60°
−165°
−160°
−155°
RSZ ?
M1
M2
M3
M4
PT
SKF
TT
GT
SAMT
SAMH
RSZ
ARSZ
DF
TKF
CMF
LCF
EKF
CF
TTF

9

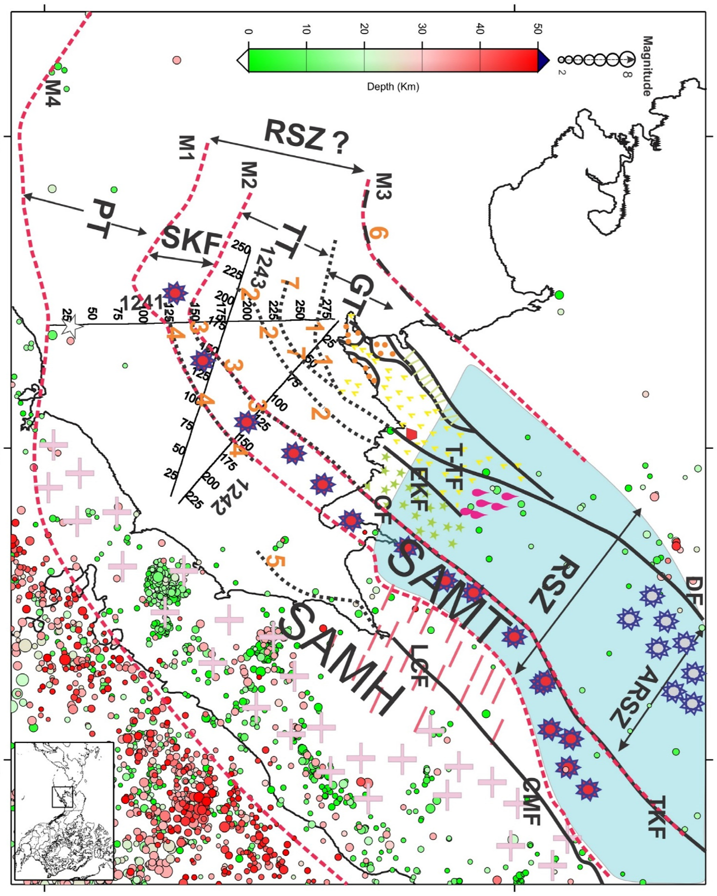

Magnitude
Depth (Km)
RSZ ?
PT
SKF
TT
GT
M1
M2
M3
M4
1241
1242
1243
T-TF
EKF
CF
SAMT
SAMH
LCF
CMF
RSZ
ARSZ
DF
TKF
56°
60°
-165°
-160°
-155°

10

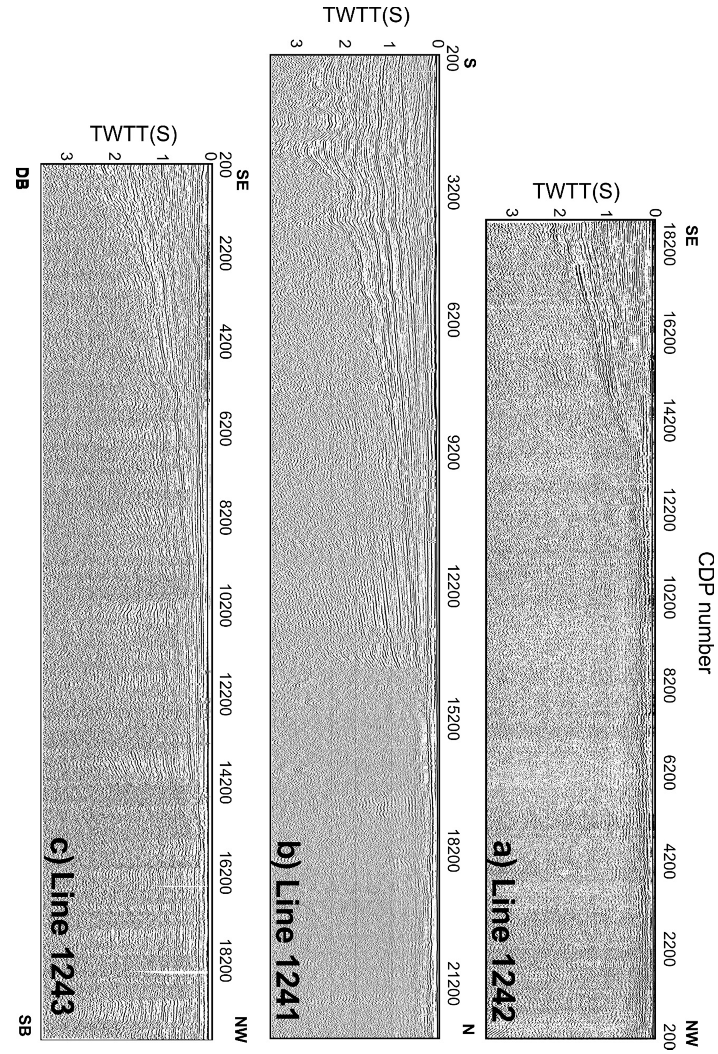
a) Line 1242
b) Line 1241
c) Line 1243
CDP number
TWTT(S)
SE
NW
S
N
DB
SB

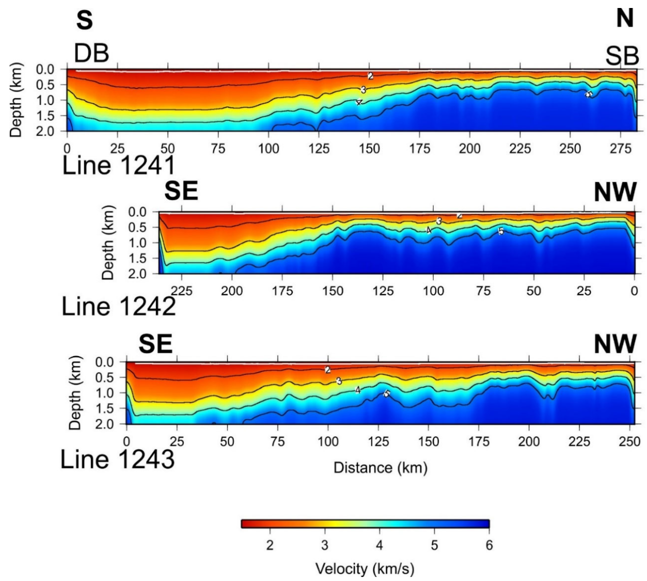
S
N
DB
SB
Depth (km)
Line 1241
SE
NW
Line 1242
SE
NW
Line 1243
Distance (km)
Velocity (km/s)

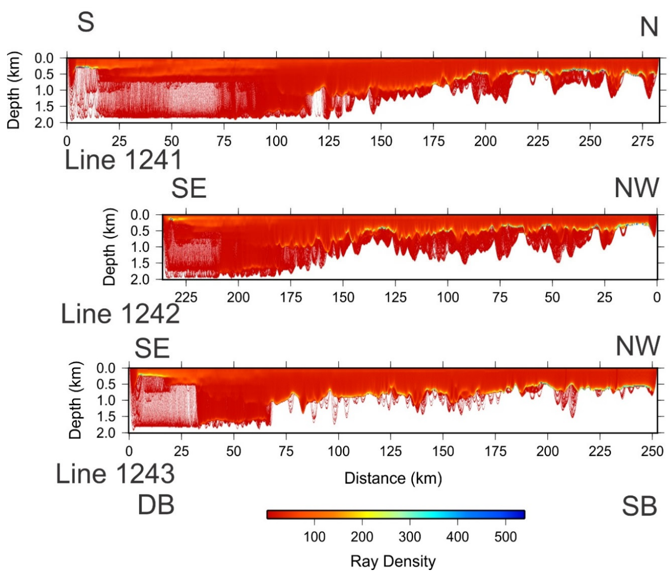
S
N
Depth (km)
0.0
0.5
1.0
1.5
2.0
0
25
50
75
100
125
150
175
200
225
250
275
Line 1241
SE
NW
Line 1242
SE
NW
Line 1243
Distance (km)
DB
SB
100
200
300
400
500
Ray Density

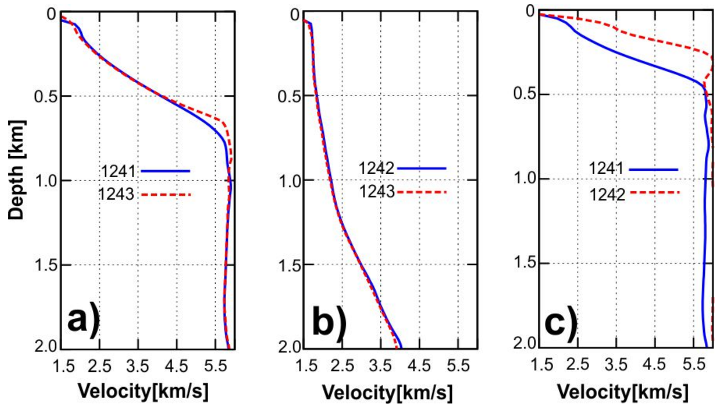

Depth [km]
0
0.5
1.0
1.5
2.0
1.5 2.5 3.5 4.5 5.5
Velocity[km/s]
1241
1243
a)
1242
1243
b)
1241
1242
c)

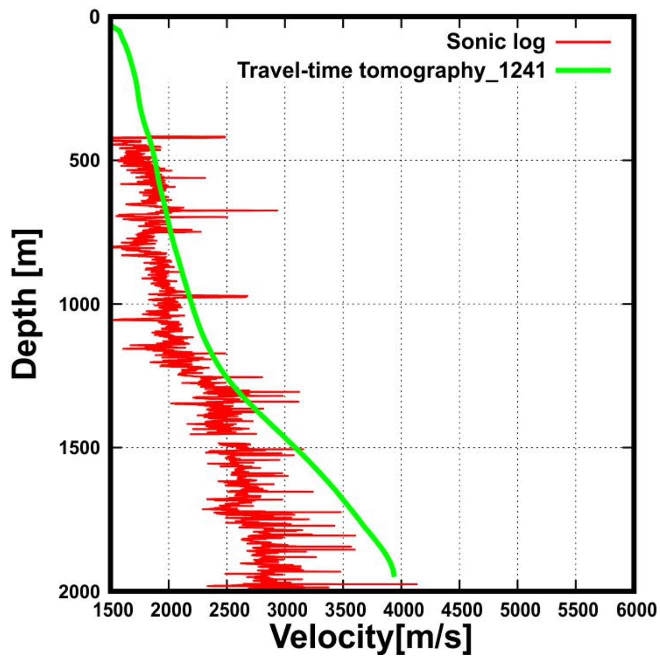
Sonic log
Travel-time tomography_1241
Depth [m]
0
500
1000
1500
2000
1500
2000
2500
3000
3500
4000
4500
5000
5500
6000
Velocity[m/s]

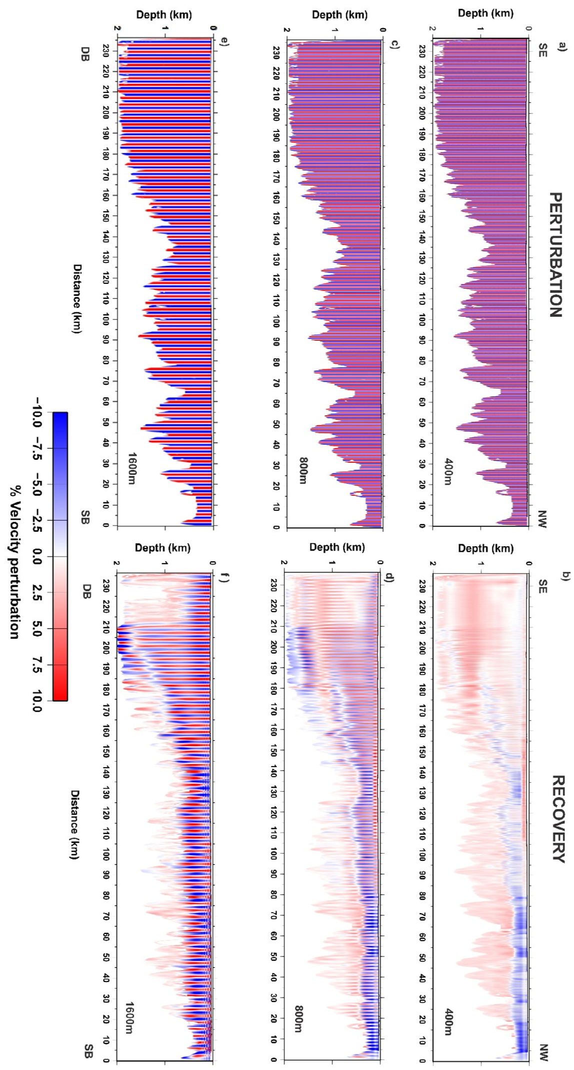
PERTURBATION
RECOVERY
a)
b)
c)
d)
e)
f)
SE
NW
DB
SB
Depth (km)
Distance (km)
400m
800m
1600m
−10.0 −7.5 −5.0 −2.5 0.0 2.5 5.0 7.5 10.0
% Velocity perturbation

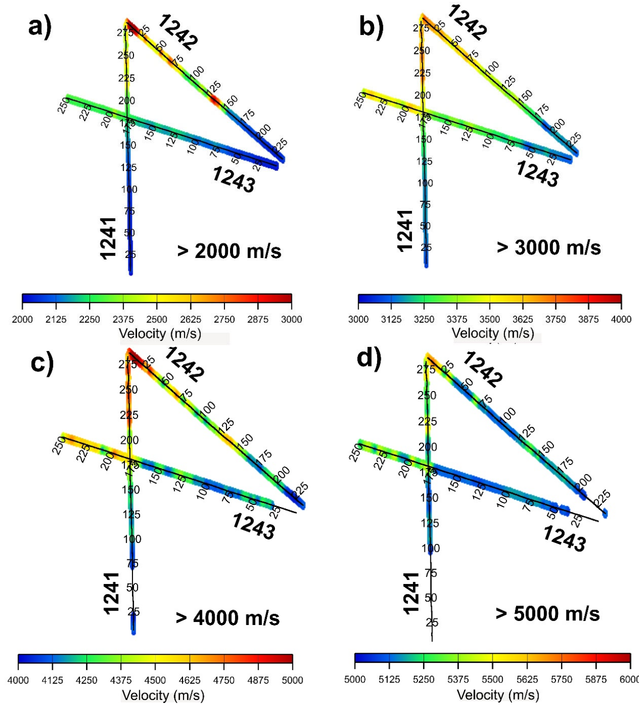

a)
1242
1241
1243
> 2000 m/s
Velocity (m/s)
b)
1242
1241
1243
> 3000 m/s
Velocity (m/s)
c)
1242
1241
1243
> 4000 m/s
Velocity (m/s)
d)
1242
1241
1243
> 5000 m/s
Velocity (m/s)

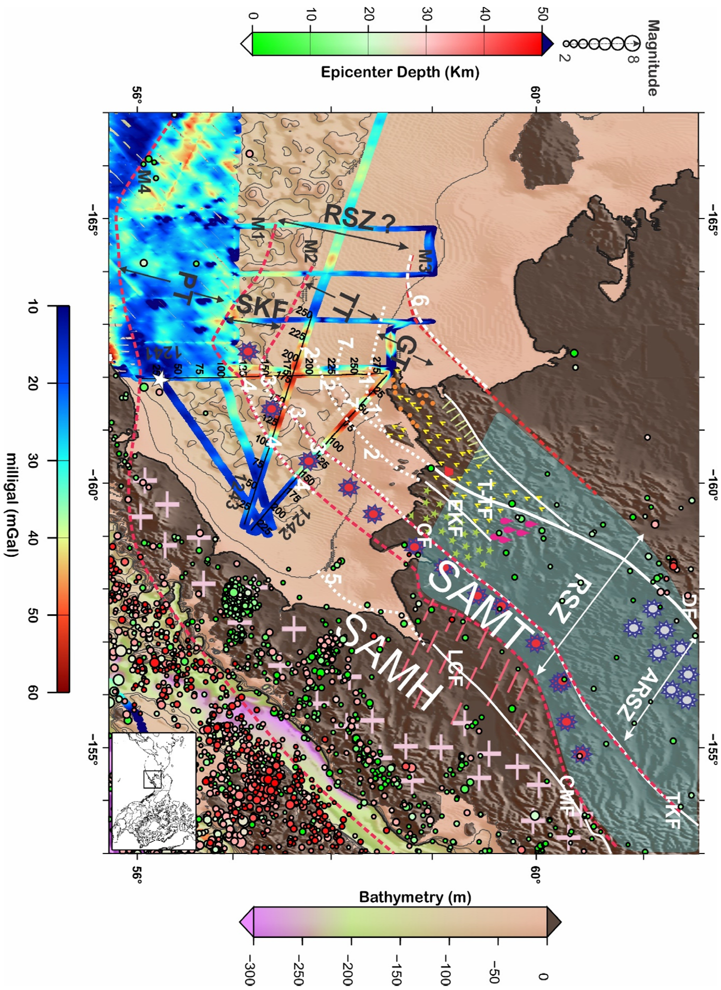
Magnitude
Epicenter Depth (Km)
milligal (mGal)
Bathymetry (m)
RSZ ?
PT
SKF
TT
GT
SAMT
SAMH
RSZ
ARSZ
TTF
EKF
CF
LCF
CMF
TKF
DF
M1
M2
M3
M4
1241
1242

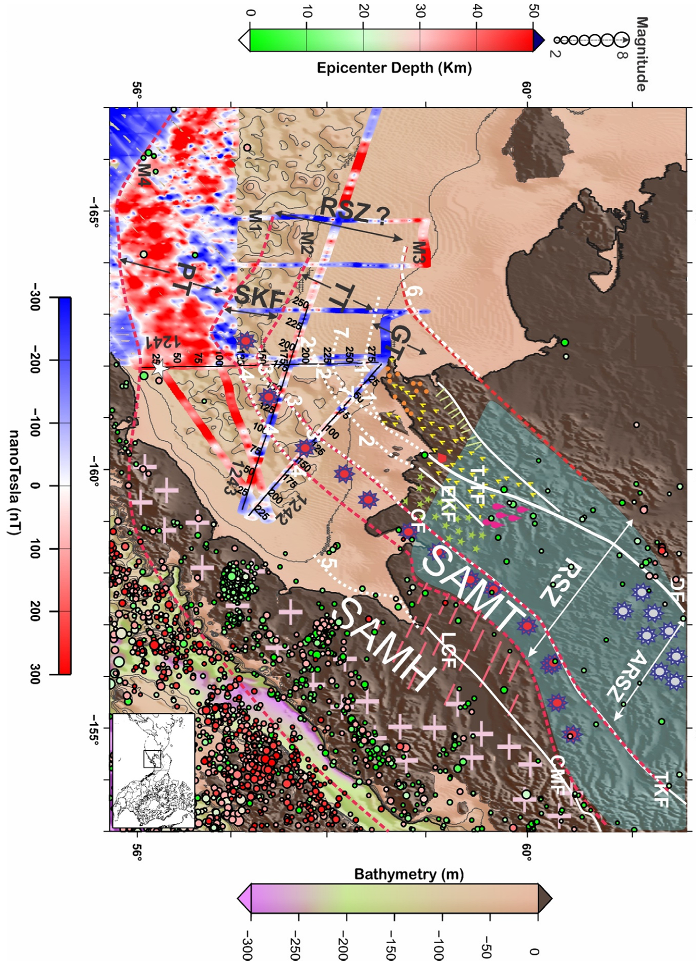

Magnitude
Epicenter Depth (Km)
nanoTesla (nT)
Bathymetry (m)
SAMT
SAMH
RSZ
ARSZ
RSZ ?
PT
SKF
TT
GT
LCF
EKF
CF
CMF
TKF
M1
M2
M3
M4
1241
1242
1243

Seismic and Potential Field Constraints on Upper Crustal Architecture of Inner Bering Shelf, Offshore Southwestern Alaska

Rajesh Vayavur[1], Andrew. J. Calvert[2]

[1]Formerly at Harquail School of Earth Sciences, Laurentian University, Sudbury, Canada.

[2]Simon Fraser University, Burnaby, British Columbia, Canada.

Corresponding author: Rajesh Vayavur (vayavur2005@gmail.com)

Key Points:

- The offshore extension of major terranes and faults of southwestern Alaska are poorly defined.
- Seismic imaging combined with well log, potential field, and geology datasets are used to constrain the major terrane boundaries and faults.
- Results provide evidence of offshore extension of major terranes and faults.

Abstract

Southwestern Alaska encompasses a group of fault-bounded tectonostratigraphic terranes that were accreted to North America during the Mesozoic and Paleogene. To characterize the offshore extension of these terranes and several significant faults identified onshore, we reprocessed three intersecting multichannel deep seismic reflection profiles totaling ~750 line-km that were shot by the R/V Ewing across part of the inner Bering continental shelf in 1994. Since the uppermost seismic section is often contaminated by high amplitude water layer multiples from the hard and shallow seafloor, the migrated reflection images are supplemented with high-resolution P wave velocity models derived by traveltime tomography of the recorded first-arrivals to depths of up to 2000 m. Additionally, other geophysical datasets such as well logs, ship-board gravity, ship-board magnetics, satellite-altimetry gravity and air-borne magnetics are also incorporated into an integrated regional interpretation. We delineate the offshore extension of the major mapped geological elements, including the Togiak-Tikchik fault, East Kulukak fault, Chilchitna fault, Lake Clarke fault, Togiak terrane, Goodnews terrane, Peninsular terrane, Northern and Southern Kahiltna flysch deposits, and the Regional Suture Zone. We interpret the offshore Togiak-Tikichik fault to be a terrane bounding fault separating the Togiak terrane and Goodnews terrane. We also locate the offshore boundaries of the Regional Suture Zone using satellite gravity anomaly and air-borne magnetic data. Furthermore, we suggest that the sedimentary fill in the graben-like features offshore, as identified by seismic tomographic velocity models, is constituted by the deposits of Northern and Southern Kahiltna flysch.

Plain Language Summary

The geological processes that have shaped the southwestern region of Alaska, as well as the neighboring Beringian shelf, involve the merging of various significant tectonostratigraphic terranes, the formation of volcanic arcs, and the creation of sedimentary basins spanning the Mesozoic to late Cenozoic eras. Determining the precise timing of terrane accretion, identifying the locations of the suture zones, and understanding their extension beneath the Bering shelf are ongoing research endeavors. Another significant unresolved issue in the geology of southwestern Alaska is the whereabouts of the offshore continuation of the faults separating the various terranes. We are able to identify the offshore extension of significant faults and terranes by seismic reflection imaging and near-surface p-wave velocity models generated using seismic traveltime tomography, integrated with complementary geological and potential field datasets.

1. Introduction

The complex tectonic evolution of southwestern Alaska and the adjacent Beringian shelf involved along-strike variation in subduction rate and dip, accretion of several large tectonostratigraphic terranes, formation of suture zones, development of magmatic arcs, and formation of sedimentary basins and a broad continental shelf between the Mesozoic to late Cenozoic (Jones et al., 1977; Coney et al., 1980; Miller et al., 2007, Trop and Ridgway, 2007). The exact timing of terrane accretion, the location of the suture zones, and their offshore extension beneath the Bering shelf is uncertain, and an area of ongoing research. Major onshore strike-slip faults (e.g. Denali and Tintina) whose orientation varies from southeast to southwest (Wirth et al., 2002) can be clearly identified on geological maps of southwestern Alaska. Though several models (Cross and Freymuller, 2008; Finzel (2011)) of Alaskan evolution have been proposed, it remains uncertain whether these faults (1) extend offshore across the entire Bering shelf from northeast to southwest, (2) rotate to form a trend parallel to the shelf edge, or (3) terminate under the inner Bering shelf.

This study aims to use tomographic velocity models and reflection interpretation of a seismic survey near the coast, together with potential field data and regional geology, to develop an integrated interpretation of the terrane boundaries and upper crustal structure of the Bering shelf offshore southwestern Alaska. Various individual and integrated geophysical maps (basement velocity displays, mean seismic velocity, ship-board gravity and magnetics, and satellite-altimetry gravity) of the study area were created and interpreted. The inner Bering shelf sedimentary stratigraphy is constrained by well log data, combined reflection/velocity images and previous studies. Well log data is used to correlate the ages and velocities of seismic stratigraphy in the basin, while the combined reflection and velocity images allow the geological interpretation to be extended across the basin, with the velocity models being especially useful where high amplitude, short-period multiples and noise contaminate reflection sections. The inner Bering shelf basement is mainly constrained by basement velocity displays that are used to identify faults, terranes, and small sub-basins. Mean velocities were estimated near the top of basement to better reveal lateral variations in velocity, and also to correlate identified faults from one line to another. Finally, potential field data were used to trace the onshore faults and terranes to the sparse seismic lines offshore. These new results clarify terrane accretion processes and current faulting models and will aid the interpretation of new passive seismic and GPS (global positioning system) data currently being acquired as part of the US Array (http://www.usarray.org/alaska).

2. Regional Tectonic Settings

2.1. Major strike-slip faults

The Denali and the Tintina fault systems are major tectonic features on geological maps of southern Alaska (Figure 1), being represented by curved, subparallel strike-slip faults whose orientation varies from southeast to southwest. The Togiak-Tikchik and Fairweather faults are the westernmost extensions of the Denali fault, whereas the Kaltag fault is the western extension of the Tintina fault. The Kaltag and the Fairweather faults postdate the era of terrane accretion, which was mostly middle Cretaceous in the area of these faults (Klemperer et al., 2002a). Many of the volcanic centers in western Alaska occur near the ends of the surface expressions of major strike-slip faults or along their projected traces (Wirth et al., 2002); for example, Figure 1 shows the Quaternary Togiak basalt field at the western terminus of the Denali Fault and the Saint Michael volcanic field near the end of the Kaltag Fault.

The Denali fault system extends ~1500 km from western Canada to near the edge of the Bering Sea. The 2002 M7.9 Denali fault earthquake occurred on the northern portion of the fault (Saltus et al., 2007), which is shown in Figure 1. This 2002 earthquake underlines the need to better understand the tectonics and geologic structure of the Denali fault and the Alaska Range orogen. In addition to its role in earthquake generation, the Denali fault facilitated the late Mesozoic and early Cenozoic northward translation and amalgamation of tectonostratigraphic terranes that form most of the Alaskan continental landmass (Fisher et al., 2007). Using geophysical data (e.g. seismic, gravity, and magnetic data), Fisher et al. (2007) interpreted the Denali fault as a sub-vertical fault that extends to at least 10 km depth in southcentral Alaska, but he also suggested that the fault may reach depths greater than 30 km based on magnetotelluric data.

Using GPS (global position system) data, Cross and Freymueller (2008) explained that interaction between a clockwise rotating Bering plate and a counter-clockwise rotating south-central Alaska block may be responsible for the reduced slip rate and lack of seismic activity on the western Denali fault, and for the development of a prominent foreland fold and thrust belt in the central Alaska Range. Using the same GPS data, Finzel (2011) proposed a kinematic plate model for Alaska, in which he explained that a wide zone of diffuse deformation, defines the boundary between the North American, Pacific and Bering plates, and relative rotation between the plates may be the source of much of the modern deformation. But none of the above models clearly explain whether the major faults (Denali and Tintina) extend offshore beneath the continental shelf or die out near the coastline.

2.2. Major composite terranes of southwestern Alaska

Southwestern Alaska can be broadly classified into six major composite terranes: the Yukon, Wrangelia, Togiak-Koyukuk, Oceanic, Central, and Southern Margin composite terranes (Plafker and Berg, 1994; Plafker et al., 1994; Saltus et.al., 1997) as shown in Figure 1. Most of these composite terranes are intruded and overlain by plutonic and volcanic rocks attributable to collisional orogenesis, arc formation, and magmatism (Nokleberg et al., 1994; Cole et al., 1999, 2006, Trop and Ridgway, 2007, Nokleberg and Richter, 2007). The present distribution of the terranes shows the severe effect of the counter-clockwise rotation and oroclinal bending of southern and southwestern Alaska which occurred predominantly in the late Cretaceous or Paleogene time (Hillhouse, 1987; Plafker et al., 1989; Worrall, 1991).

The Yukon composite terrane (YCT) (Figure 1) is composed of ductilely deformed, tectonically dismembered Proterozoic to Paleozoic metamorphic rocks, and the plutonic remnants of a volcanic arc (Plafker et al., 1994). The Togiak-Koyukuk composite terrane (TCT) (Plafker and Berg, 1994; Saltus et al., 1997) is a poorly exposed terrane consisting of Late Triassic through Early Cretaceous arc-related volcanic and volcaniclastic rocks, and their intrusive equivalents. These rocks are overlain by mid-Cretaceous and Paleogene volcanic and marine sedimentary rocks. The arc rocks also record imbrication, subduction, and low-grade Middle Jurassic metamorphism. The Oceanic composite terrane (OCT) (Plafker and Berg, 1994; Saltus et al., 1997) is composed mainly of oceanic basalt, sedimentary rocks, and minor ultramafic rocks, and the terrane is interpreted to be obducted fragments of paleo-Pacific crust that were thrust on to the continental margin before and during the accretion of the TCT in the Late Jurassic and Early Cretaceous (Plafker and Berg, 1994). The Central composite terrane (CCT) (Plafker and Berg, 1994; Saltus et al., 1997) is primarily made up of rifted, rotated, translated, and imbricated miogeoclinal fragments. This composite terrane consists of Late Proterozoic and Cambrian clastic deposits and also records the Late Precambrian to Ordovician emplacement of ultramafic and deep marine rocks.

The Wrangellia composite terrane (WCT) (Figure 1) represents the largest tectonostratigraphic terrane of southern and southwestern Alaska and is composed of upper Paleozoic and Mesozoic arc-related marine sedimentary, basaltic, and tholeiitic volcanic rocks plus limestone, argillite, and metabasalt, along with some later granitic arc-related intrusions (Plafker et al., 1994; Nokleberg et al., 1994). The Southern Margin composite terrane (SMCT) is juxtaposed against the outboard margin of the Wrangellia composite terrane. It is an accretionary complex formed as a result of Late Mesozoic and Cenozoic subduction and offscraping of sediments derived largely from the Wrangellia composite terrane to the north (Plafker et al., 1994; Nokleberg et al., 1994), but also includes the modern accretionary wedge and underthrusts Yakutat terrane (Figure 1).

In south-central Alaska, the Wrangellia composite terrane is juxtaposed against the Yukon composite terrane along a broad suture zone called the Alaska Range suture zone (ARSZ) (Ridgway et al., 2002; Trop and Ridgway, 2007) as shown in Figure 1. The ARSZ is one part of a much larger suture zone between the Wrangellia composite terrane and northwestern North America (Coney and Jones, 1985; Ridgway et al., 2002). The ARSZ consists of complexly deformed Kahiltna flysch units, and igneous and metamorphic rocks which are Jurassic-Cretaceous in age (Wallace et al., 1989; Ridgway et al., 2002; Trop and Ridgway, 2007). There are several major faults identified within this suture zone. The Hines Creek fault defines the boundary between the YCT, and the ARSZ and Talkeetna fault defines the boundary between the ARSZ and the WCT (Fitzgerald et al., 2014). The Denali fault, which is characterized by 400 km of right–lateral displacement in south-central Alaska, extends through this suture zone (Eiscbacher, 1976; Nokleberg et al., 1985; Trop and Ridgway, 2007).

2.3. Bering shelf and Eocene extension

In Cretaceous time, the southern edge of the Bering shelf was a south-facing convergent margin. A major tectonic reorganization in the middle to late Eocene time (Scholl et al., 1986; Worrall, 1991) transformed the Beringian margin (Figure 1) into a passive margin that now includes the Bering continental shelf, which is almost half the size of Alaska (Cooper et al., 1976; Marlow 1979; Marlow et. al., 1983; Fisher et. al., 1982). Following the major tectonic reorganization, a series of right-lateral strike-slip faults formed parallel to the now abandoned Beringian active margin (Figure 1) and marked the onset of Eocene extension. These strike-slip fault systems formed most of the Tertiary basins offshore southwestern Alaska namely, the Navarin, St. George, and Bristol Bay (also known as North-Aleutian) basins (Figure 1). A total of five COST (Continental Offshore Stratigraphic Test) wells were drilled into these shelf basins and suggested that adequate hydrocarbon reservoir beds of the late Cenozoic age probably exist within all the shelf basins (Turner et al., 1988; Marlow et al., 1994). The potential of these basins for hydrocarbon exploration has stimulated several marine geophysical and geological investigations. These studies were successful in delineating the major basins and also providing the geologic framework of the Bering shelf region. Worrall (1991) extensively studied the evolution of these shelf basins using the then-available seismic reflection sections.

3. Study area

Our study area lies in the inner Bering shelf of southwestern Alaska (Figure 1). Across most of the shelf, the seafloor is exceptionally flat, and the bathymetry of the shelf area is less than 100 m deep as shown in Figure 2. Bristol Bay basin also known as the North Aleutian basin, which forms part of the study area, extends more than 322 km across the southern Bering shelf. The basin is of late Mesozoic to early Cenozoic age and developed after the accretion of the terranes that formed the Alaska Peninsula at the end of the Mesozoic (Worrall, 1991; Marlow et al., 1994; Finzel et al., 2005). The maximum thickness of the basin is 6000 m, which occurs in the southeast (Finzel et al., 2005). The basin is asymmetrical and bounded to the northeast by highly deformed, locally intruded, metamorphosed Paleozoic and Mesozoic rocks (Hatten, 1971), and onshore to the southeast by the Black Hills uplift (Marlow et al., 1994).

The southern boundary of the Bristol Bay basin is mostly composed of Mesozoic and Cenozoic volcanic and plutonic basement rocks that form the core of the Alaska Peninsula (Worrall, 1991; Finzel et al., 2005). The northern boundary of the Bristol Bay basin, which lies beneath the Bering shelf may be formed by Mesozoic sedimentary, igneous, and metamorphic rocks (Marlow et al., 1994). Although there has been continued oil industry interest in the Bristol Bay region, federal prohibitions on oil and gas leasing in the North Aleutian basin have prevented new offshore exploration. The 1983 North Aleutian COST-1 well, which is the only well drilled in the Bristol Bay basin, penetrates to a total depth of 5.2 km, and is intersected by one of the seismic profiles of the present study (Figure 2). The well is characterized by cores and wireline logs that include both density and sonic logs. The data from these logs were used to constrain the ages of seismic reflectors and are useful in establishing the approximate timing and evolution of the basin, which will be further discussed in section 6.

The seismicity of southwestern Alaska for earthquakes of M≥2 of the past 100 years (data taken from the USGS earthquake catalog) is also shown in Figure 2. Analysis of gravity data in southern Alaska (Barnes, 1976; Saltus et al., 2007) indicates a Moho depth that varies from 25 km offshore southwest Alaska to 50 km in southcentral Alaska (Saltus et al., 2007). So only earthquakes shallower than 50 km are displayed to show seismicity within the crust. Southwestern Alaska and the Bering Sea shelf are characterized by low rates of seismicity.

3.1. Subterranes near the study area

In this section, we present the geology of the Goodnews and Togiak terranes (Figure 2) plus their sub-terranes, and also discuss the Peninsular terrane and Kahiltna flysch, which lie respectively to the south and northwest of our study area. The geology of the terranes was synthesized by Decker et al. (1994) following earlier work by Jones and Siberling (1979) and Box (1985).

The Togiak terrane is composed of volcanic flows, coarse volcaniclastic breccias, tuffs, and associated epiclastic rocks of Late Triassic through Early Cretaceous age. The terrane underwent only low-grade metamorphism and generally lacks a metamorphic fabric. Togiak terrane is divided into two sub-terranes: the Hagmeister and Kulukak subterranes (Figure 2). The Hagmeister subterrane consists of Late Triassic through Early Cretaceous basaltic to dacitic volcanic and volcaniclastic rocks deposited on Late Triassic ophiolitic rocks. The Kulukak subterrane consists predominantly of Jurassic volcaniclastic turbidites (Decker et al., 1994).

The Goodnews terrane (Figure 2) is an amalgamation of variably metamorphosed blocks of laminated tuff, chert, basalt, greywacke, limestone, gabbro, and ultramafic rocks (Decker et al., 1994). The terrane is divided into four subterranes namely Cape Peirce, Platinum, Nukluk, and Tikchik. In Figure 2, only three of the above four subterranes, which are relevant to this study, are shown. The Cape Peirce subterrane consists of foliated metamorphic rocks, which were derived from both sedimentary and igneous protoliths of probable Permian and Triassic ages. The Platinum subterrane consists of Early and Middle Jurassic non-foliated mafic flows, tuff, and volcaniclastic rocks. The Tikchik subterrane (Jone and Siberling, 1979) is a structurally complex assemblage of clastic rocks and chert of Paleozoic and Mesozoic age.

The Peninsular terrane is a Triassic to Jurassic island-arc complex that was accreted to the North American continent by the Early Cretaceous (Jones et al., 1987; Ridgway et al., 2002). This terrane includes mafic to andesitic flows, volcaniclastic rocks, limestone and mudstone. These rocks structurally overlap and are intruded by Jurassic plutonic rocks of the Talkeetna arc (Reed et al., 1983; Rioux et al., 2010). The plutonic rocks include gabbroic to granitic composition, but are dominated by quartz diorite and tonalite rocks (Detterman and Reed, 1980; Reed et al., 1983).

Hults et al. (2013) using a zircon age dating method suggested that the Kahiltna flysch can be divided into two belts, the NKF (Northen Kahiltna flysch belt) and SKF (Southern Kahiltna flysch belt) as shown in Figure 2. The zircon data reveal that the southern flysch belt was derived from the Wrangellia composite terrane, whereas the northern flysch belt was derived from the terranes that make up the paleo-Alaskan margin. The boundary between these two flysch belts is coincident with a large, deep geophysical magnetic gradient. The southwestern part of this geophysical gradient is coincident with the Chilchitna thrust fault as shown in Figure 2. Geophysical models place a deep, through-going, crustal-scale suture zone in the area between these two flysch belts. Ridgway et al. (2002) proposed that the entire flysch belt between the Talkeetna fault and the Hines Creek strand of the Denali fault represents a suture zone called the Alaska Range Suture Zone (ARSZ), which is shown in Figure 2.

4. Seismic survey

In 1994, three multi-channel seismic reflection profiles (lines 1241, 1242, 1243) were acquired by the R/V Ewing in the inner Bering shelf area as part of the Pacific to Bering Sea deep seismic experiment (Figure 2). The data were recorded by a 160-channel hydrophone streamer with near and far offsets of 255 m and 4230 m respectively, and shot with an 8400 cubic inch airgun array. The shot interval is approximately 50 m, and the receiver interval is 25 m. Record lengths varied from 16s to 17s. For the current study, line 1243 is truncated to the region of interest. A sub-section of line 1241, shown as a yellow dashed line in Figure 2, has already been studied by Walker et al. (2003) to understand the tectonic evolution of the Bristol Bay basin. Along line 1242, 6 WHOI ocean-bottom hydrophones (OBHs) and 2 USGS ocean-bottom seismometers (OBSs) recorded wide-angle arrivals from the R/V Ewing's source array for a deep crustal study (Lizarralde, 1997), shown as red dashed line in Figure 2. Vayavur and Calvert (2016) and Vayavur (2017) performed a comprehensive study on seismic noise in the study area (on line 1242) and its implications on seismic reflection and tomography imaging.

In this paper, we present the reprocessing of three intersecting multichannel seismic reflection lines (Appendix 1) 1241, 1242, and the eastern part of 1243 totaling ~750 km line length to identify faults and basement structure. Since the identification of sub-vertical faults at shallow depth is difficult due to low fold and interfering short-period multiples and dispersive guided waves generated by the hard, shallow seafloor, we used tomographic P-wave velocity models to infer the location of faults at <1-2 km depth. These velocities can be used for discriminating different lithologies: pre- versus post-extension sedimentary strata, felsic versus mafic terrane basement, and structures associated with faulting, e.g. basement offsets or grabens due to transtensional strike-slip motion.

5. Traveltime tomography of lines 1241, 1242, 1243

We used the Pronto first-arrival tomography code of Aldridge and Oldenburg (1993) which is based on a finite difference solution to the eikonal equation. Ray paths from each receiver back to the source are generated by following the steepest descent direction through the computed 2-D traveltime field. The nonlinear tomographic problem of inverting recorded traveltimes for a subsurface velocity model can be linearized and solved iteratively, in which an update perturbation to a velocity model is calculated from the traveltime misfit. Thus an initial starting model is required. So inversion is performed in two stages (Appendix 2).

Figure 3 displays the final velocity models of all the lines with the region of deep basement on the left. The line 1242 velocity model is displayed at the top, because it is nearest to coast, followed by models for line 1241 and line 1243. The depth of the igneous basement increases from 100-500 m in the north, where it is characterized by velocities >5000 m/s, to at least 6000 m beneath the North Aleutian basin in the south. At the northern end of the velocity models, low velocity rocks with velocities approximately equal to 4 km/s occur in depressions or graben-like basins within the upper part of the high velocity basement rocks. A more complete interpretation of the models are presented in section 6 in combination with well log and seismic reflection image.

Traveltime residuals for each shot-receiver pair (Figure 4) are plotted to indicate the quality of the fit to the observations of the calculated first-arrivals. Although the amplitude of the travel time residuals is > 25 ms in certain sections of the profile, values are generally < 5 ms. Clusters of slightly higher residuals were found where the basement is shallow i.e. towards northern end of all the seismic lines and at far channels. Vertical and horizontal bands in the traveltime residual plot indicate skipped shot points and killed receiver groups respectively. Slightly high residual values of 10-15 ms are associated with far offset receivers and also at the crossover point from the direct water wave to seafloor refraction (Calvert et al., 2003).

Since the study area consists of intersecting seismic lines, a comparison was made between 1D velocity profiles at line intersections to check the consistency of the final velocity models and also the robustness of traveltime tomography inversion (Appendix 3.1). To assess the quality of the traveltime tomographic inversion, a comparison was made between the sonic log recorded in the COST-1 well and a 1-D velocity profile extracted from the velocity model for line 1241 where it intersected the well (Appendix 3.2). We also compare the current tomographic velocity model from MCS line 1242 with an available interpreted offshore OBS refraction line (after Lizarralde, 1997) (Vayavur, 2017, section 5.3.2, page 115-117). The upper crustal velocity model from line 1242 is consistent with the deeper model from OBS refraction profile BA3, providing general support for this final velocity model derived from traveltime tomography. The final velocity models were further subjected to a series of corrugation tests (Appendix 4) to evaluate the resolution of the estimated final velocity models, and also the sensitivity of the tomographic inversion.

6. Well log and Seismic interpretation

6.1. Major formations in COST-1 well

As discussed in section 3, the North Aleutian COST-1 well, which lies on the south side of line 1241, is the only well drilled in the Bristol basin study area. This well has been extensively studied by many researchers (Turner et al., 1988; Walker et al., 2003; Finzel et al., 2005;

Sherwood et al., 2006; Finzel et al., 2009) both for hydrocarbon exploration and tectonic studies. The COST-1 well did not penetrate Mesozoic basement, but reached a total depth of ~5200 m in Lower Eocene rocks of the lower part of the Tolstoi Formation (Sherwood et al., 2006; Turner et al., 1988). The other major formations which overlie the Tolstoi formation are Stepovak, Bear Lake, and Milky River formations as shown in the lithological chart in Figure 5.

These formations are associated with three major phases of Cenozoic subsidence (Worrall, 1991; Walker et al., 2003; Finzel et al., 2005; Finzel et al., 2009): 1) Fault controlled subsidence caused by Paleocene and Eocene extensional and strike-slip faulting (Tolstoi formation), 2) Late Eocene to middle Miocene flexural subsidence caused by crustal loading due to development of the volcanic arc to the south (the Stepovak and Bear Lake formations), 3) Late Miocene to Holocene subsidence, which was driven mainly by sediment loading from the Alaska Peninsula (the Bear Lake and Milky river formations). The Bear lake formation is considered to have the highest reservoir potential in the gas rich frontier Bristol Bay basin (Finzel et al., 2009). The base of the Tolstoi formation is a prominent Paleocene unconformity that places the Tolstoi on a variety of older Mesozoic formations (Sherwood et al., 2006).

6.1.2. Velocity estimation from COST-1 sonic log

Using well-log correlation with seismic reflection data, Walker et al., (2003) has divided the stratigraphic column near the COST-1 well into six units A, B1, B2, C, D and E (Figure 5) separated by five principal unconformities. To estimate a characteristic velocity for these principal unconformities, we filtered the sonic log with a 0.4 km median filter at a 0.01 km sample interval as shown in Figure 5. The estimated velocities were then be used to pick various horizons in the velocity model when overlaid on migrated seismic reflection section which will be discussed in next section. The top of Unit E corresponds to the red event (Worrall, 1991), which is a major late Eocene unconformity, and the seismic interval velocity near this contact is estimated to be approximately 3.1 - 3.3 km/s. The top of Unit D, which is middle Oligocene, has a seismic velocity of approximately 2.8-3.1 km/s. The top of Unit C is of late Oligocene age, and has a velocity of approximately 2.6-2.8 km/s. The top of Unit B2 is middle Miocene and corresponds here to a seismic velocity of approximately of 2.2-2.5 km/s, whereas the top of Unit B1 is early Pliocene with a velocity of approximately 1.9-2.1 km/s. In Figure 5, the sonic log is compared to the 1-D vertical velocity profile from the traveltime tomography model at that location as discussed earlier.

6.2. Seismic interpretation of inner Bering shelf sediment stratigraphy from combined reflection/velocity section

In this section, the coincident post-stack migrated seismic reflection sections are combined with traveltime tomography velocity images to provide a unified interpretation of the near-surface geology. Figure 6 shows the overlay of velocity models on the migrated reflection sections. All three seismic sections (line 1241, 1242 and line 1243) show the northward thinning of the sedimentary section; in the south, the sedimentary thickness is 2-3 km, but in the north, it decreases to a few hundred metres. The previous study by Walker et al., (2003) on a small section of reflection line 1241, which used seismic-well log correlation at the COST-1 well to identify reflections that correlate well with the principal unconformities, forms the basis for our current stratigraphic interpretation of all three lines across the Bristol basin. The reflections identified by Walker et al., (2003) can be traced across the basin on line 1241, but are difficult to locate accurately on lines 1242 and 1243 due to the intermittent nature of some reflections.

To the south on line 1241, Unit E was deposited in a non-marine environment, and includes graben-like features (Walker et al., 2003), which are filled with sedimentary deposits derived from volcanic source rocks, probably by erosion of the Peninsular terrane to the south (Turner et al., 1988; Walker et al., 2003). This unit may represent a continuation of the Carapace sequence (Walker et al., 2003). The late Eocene unconformity is the red event, which marks the onset of extension (Worrall, 1991), and forms the upper boundary of unit E. In the study area, the red event is typically a prominent continuous reflector and observed in most seismic sections. This red event experienced a long erosional history, as indicated by the northward-onlap of late Eocene-Oligocene reflectors of units D and C (Walker et al., 2003). Immediately above the red event, unit D, comprises late Eocene through early Oligocene interbedded sandstone and shale. Unit C consists of late Oligocene interbedded sandstone and siltstone. Both these units, D and C, represent a general transition from non-marine to shallow marine depositional environments, and both units are derived from volcanic and metamorphic source rocks (Turner et al., 1988; Walker et al., 2003). The sedimentary sequences of Unit B are divided into two subunits B1 and B2, separated by a high amplitude reflector and have a similar depositional environment to units D and C. Strata of Unit B are late Oligocene, Miocene and early Pliocene in age (Walker et al., 2003). Unit A generally appears to downlap to the north and comprises unconsolidated volcaniclastic sediments of late Pliocene to Quaternary age (Turner et al., 1988; Walker et al., 2003).

The red event which was interpreted in the south, was traced updip into the areas of shallow basement in the north, in part, by following the ~3.1 km/s velocity contour estimated from the filtered sonic log, as discussed previously. In the north, the red event forms a disconformity above the graben-like features (discussed in the next section) that are filled with older stratified pre-red sediments with velocities ranging from 3.3 – 4.5 km/s. The origin of these older pre-red rocks may be the northern Kahiltna flysch (NKF) sediments of Hults et al. (2013) or the Carapace sequence of Worrall (1991). The highly deformed rocks denoted by SKF on line 1242 in Figure 6, may represent southern Kahiltna flysch sedimentary deposits. These deposits were probably derived from the Wrangellia and Peninsular arc terranes to the south, so they exhibit slightly higher velocities, i.e. around 4.5- 4.8 km/s, in comparison to northern Kahiltna flysch deposits, which were derived from terranes of North America affinity (Hults et al., 2013). The southern Kahiltna flysch deposits coincides with SAMT (Saltus et al., 1999; 2003; 2007) denoted by magnetic boundaries M1 and M2 (Figure 6). SKF deposits when traced onto other lines using potential field data seem to be buried below a thick layer of sediments on lines 1241 and 1243.

6.3. Seismic interpretation of inner Bering shelf basement structures

The combined seismic image (Figure 6) reveals several important basement features. Generally, all three seismic reflections sections (line 1241, 1242 and line 1243) show the northward shoaling of the basement. On the post-stack migrated seismic section, the basement reflection is difficult to identify accurately, because it is commonly obscured by strong multiples and coherent noise. Therefore, the basement location is mainly interpreted by using the overlaid velocity image. Generally, high velocity rocks where velocity exceeds 5 km/s are interpreted to be basement. In the north, the interpreted basement on line 1241 and line 1242 is overlain by a thin layer (i.e. $\leq$0.3 km) of sediments, but on line 1243, the thickness of the sediments is approximately 1 km. To the south, the basement is not well constrained by velocity due to the limited depth of ray coverage and hence not traced.

6.3.1. Basement characterization

To characterize the basement velocities in the north more accurately, the final velocity models were first masked with the corresponding ray coverage and plotted with a velocity scale of 5.0-7.0 km/s as shown in Figure 7. As stated earlier, the basement velocity along the profiles is mostly characterised by a value of ~5.0 km/s, but in some places basement velocity increases to ~5.9-6.0 km/s, as shown by orange lines in Figure 6 and Figure 7, which probably indicates Mesozoic igneous basement. Elsewhere velocities inferred at relatively large depths may be less reliable due to the limited ray coverage. Rocks with a relatively high velocity of ~6.0 km/s, which occur on line 1242 between 0-30 km distance and on line 1241 at 260-275 km, might represent ophiolitic rocks of the Cape-Pierce subterrane of the Goodnews terrane (Figure 7). The above basement velocity seems to be consistent with the basement velocity estimated by the nearby OBS refraction survey (Lizarralde, 1997). Togiak terrane basement may lie between the southern Kahiltna flysch basement and Goodnews terrane basement. The Peninsular terrane basement may lie to south of the southern Kahiltna flysch basement (Figure 7), and this will be further constrained by potential field data.

In addition, a total of 10 graben-like features G1, G2…G10 were identified at the top of the basement as shown in Figure 7. These features appear to be mostly fault-bounded and are near the seafloor on lines 1241 and 1242, but buried more deeply on line 1243. Faults which are inferred from small reflection offsets on migrated sections coincide with the location of faults inferred using lateral velocity discontinuities. Faults denoted by numbers 1-3 are interpreted as the offshore extensions of major onshore faults (e.g. 1-Togiak-Tikchik fault, 2-East Kulukak fault and 3-Chilchitna fault), while the origin of the fault denoted by 4 is unknown. The Togiak-Tikchik fault denoted by 1 probably offsets the Cape-Pierce subterrane basement creating graben-like feature G2 on line 1242 and G6 on line 1241, whereas the fault denoted by 2 may represent the offshore extension of East Kulukak fault; however, it is unclear from both these images (Figure 6 and Figure 7) whether these faults extend vertically into the subsurface or are listric. Faults 3 and 4 appear to bound and thrust the SKF deposits as shown in Figure 7. The correlation of the near-surface locations of the above faults from one line to another line is further constrained by potential field data, mainly by satellite altimeter gravity data which will be discussed later.

6.3.2. Line-to-Line correlation of basement – sediment contacts

To correlate basement – sediment contacts from one line to another and trace them across the shelf, mean velocity slices of all the lines are derived (Appendix 5) and overlaid on the topographic map (Figure 9). We have chosen Figure A7c as the final mean velocity slice for interpretation and displayed it on a topographic map using a velocity scale of 4-5 km/s as shown in Figure 9. Towards the north end of the seismic profiles, higher mean velocities >4.8 km/s are punctuated by low mean velocities < 4400 m/s which probably indicate fault-bounded graben-like features, also identified on vertical sections of the velocity models in Figure 7. The faults identified on these vertical sections, which were inferred from velocity discontinuities correlate from line to line as shown in Figure 9 by the dotted lines. The T-TF fault denoted by 1 probably intersects line 1242 at ~30 km and line 1241 at ~260 km. The EKF fault denoted by 2 probably intersects line 1242 at ~65 km, line 1241 at ~210 km and line 1243 at ~215 km. The CF fault denoted by 3 probably intersects line 1242 at ~120 km, line 1243 at ~135 km and line 1241 at ~140 km. The unknown fault denoted by 4 probably intersects line 1242 at ~160 km, line 1243 at ~110 km and line 1241 at ~120 km. The tracing of these faults between the lines is further constrained by potential field data, mainly by satellite altimetry gravity data (Figure 9) and to some extent by shipboard potential field datasets (see Figure A8 and Figure A9 of Appendix).

7. Potential field data

To provide further constraints on subsurface structures in the vicinity of the tomography velocity models, potential field data from ship-board gravity and magnetic surveys and from regional datasets such as satellite altimetry gravity measurements and airborne magnetics were used. Potential field geophysical surveys are particularly useful for geologic interpretation in offshore settings where bedrock exposures are remote and covered by quaternary sedimentary deposits. Lateral variations in gravity and magnetic anomalies are the result of lateral contrasts in rock density and rock magnetic properties (susceptibility and remnant magnetisation) respectively. These contrasts may occur across geologic structures such as faults or folds, across lithological or stratigraphic contacts, or variations resulting from major facies changes in a single stratigraphic unit. In the following section, we discuss the regional satellite altimetry gravity and airborne magnetic datasets. The ship-board data (gravity and magnetic) description and their corresponding individual maps are presented in the Appendix 6.

7.1. Air-borne magnetic data

Two aeromagnetic grids of Alaska: a composite grid and a merged grid were compiled at 1 km spacing. The composite grid includes all surveys at their original flight elevations, but the merged grid displays surveys which have been mathematically continued to a common flight height of 300 m above ground level (Meyer and Saltus, 1995). The offshore Bering shelf data were first compiled by Godson (1994); most of this compilation was performed by hand re-contouring analog maps and then digitizing them. The updated merged grid of North America magnetic anomaly was freely available to download from USGS mineral resources website (https://mrdata.usgs.gov/magnetic/). Figure 8 shows updated North America aeromagnetic anomaly merged grid plotted using Seequent's Oasis Montaj software package.

Using the merged grid, Saltus et al. (1999) interpreted probable offshore extensions of the southern Alaska magnetic domains westward onto the Bering Shelf as shown in black lines in Figure 8. To focus on the deep, crustal-scale features in the magnetic compilation, Saltus et al. (2003) performed upward continuation by 10 km of the merged aeromagnetic compilation map. The features discussed in this section can be clearly identified on that map. The Southern Alaska magnetic high (SAMH) and southern Alaska magnetic trough (SAMT) are two prominent domains which are laterally continuous features (~2500 km), with deep magnetic features (Figure 8). The high amplitude magnetic anomaly of the SAMH is attributable to the mafic rocks of the accreted Wrangellia and Peninsular terranes (Saltus et al., 2003, 2007). The 2002 M7.9 Denali earthquake occurred on the portion of the Denali fault that marks the northern boundary of the SAMH, the south boundary of which closely follows the Border Ranges fault system (BRFS) (Saltus et al., 2003, 2007). The SAMT is a 30 to 100 km wide crustal scale feature bordered to the south by the SAMH. The SAMT does not have a uniform character, but instead has distinct eastern and western portions on either side of a central gap (Saltus et al., 2003). The central portion of SAMT coincides with the Alaska range suture zone (ARSZ) (Brennan et al., 2011) and the western part of the SAMT largely coincides with deformed Mesozoic rocks of the Kahiltna flysch (Saltus et al., 1997; Saltus et al., 2003; Saltus et al., 2007). In Figure 8, M1, M2 and M4 represents offshore boundaries of the SAMH and SAMT domains (Saltus et al., 1999; Saltus et al., 2003), whereas M3 proposed from the current study denotes the possible offshore boundary of rocks with a neutral magnetic character. Boundary M3 coincides with feature 6 on the satellite altimetry gravity map (Figure 9). The region between M3 and M1, may indicate the offshore extension of a deep crustal-scale feature which we define here as a regional suture zone (RSZ), which includes the entire Alaska Range suture zone (ARSZ) of Ridgway et al. (2002) and the interior neutral magnetic domain shown in Figure 8.

7.2. Satellite altimetry gravity data

The global 1-minute grid high resolution free air gravity anomaly data from satellite measurements was compiled by Sandwell et al. (2014) and is freely available for download from the site (http://topex.ucsd.edu/cgi-bin/get_data.cgi). Gravity models derived from satellite measurements can be helpful in delineating long wavelength features from deeper sources. These models are powerful tools for mapping tectonic structures, especially in ocean basins where topography is buried by water and a thick layer of sediments (Sandwell et al., 2014). However, it is important to verify the above data with corresponding ship-board measurements. In the present context, the satellite altimetry gravity highs (Figure 9) closely match the ship-board gravity highs (Figure A8 of Appendix), and altimetry map (Figure 9) provides a valuable constraint on the geometry of some interpreted terranes and faults.

A combined interpretation was made, by overlaying the mean velocities on satellite altimetry gravity data (Figure 9). Free air gravity anomaly of the satellite-altimetry dataset is used for interpretation, as the Bouguer correction is assumed to be negligible because of relatively flat seafloor over the inner Bering shelf. Seven curved features with steep gravity gradients were identified as shown in Figure 9, and are numbered 1-7. These features are continuous and can be easily traced from one seismic line to another. Features 1- 4 can be traced offshore onto all the lines and indicate the probable extension of major faults: 1- Togiak-Tikchik fault, 2- East

Kulukak fault, 3- Chilchitna fault, 4- unknown. The location of these faults is consistent with faults inferred from the velocity discontinuities. The contact indicated by number 5, cannot be traced onto the seismic lines, which suggests that this feature characterized by a gravity high does not extend west of 159^{o} W or its presence is obscured by the thick basin fill. The arcuate long wavelength feature denoted by number 6, north of the seismic profiles may indicate a deep-seated crustal anomaly or perhaps a laterally extensive shallow source, correlates with the air-borne magnetics boundary M3 as discussed earlier. Because of the bend in the shape of T-TF fault offshore, slip may have been distributed along a splay fault, denoted by fault ‘7’ (Figure 9).

8. Offshore extension of major geological elements

8.1. Togiak-Tikchik fault

The current study constrains the offshore extension of the Togiak-Tikchik dextral strike-slip fault in southwestern Alaska by using tomographic velocity, satellite-derived gravity data, subsurface geology and previous geophysical studies. The Togiak-Tikchik fault, which is fault 1 in Figure 9, is a dextral strike-slip fault, and considered to be the westernmost extension of the Denali fault. The offshore location of the fault is inferred from a velocity discontinuity identified on the vertical sections of the tomographic velocity models shown in Figure 7. The velocity discontinuity also coincides with a steep gravity gradient on the satellite altimetry gravity anomaly map (Figure 9). Using this characteristic feature, the fault was traced offshore intersecting line 1242 at ~30 km and line 1241 at ~260 km.

Onshore southwestern Alaska, the Togiak-Tikchik fault appears to be an intra-terrane fault cross-cutting the Hagmeister sub-terrane of the Togiak terrane. But on line 1242 and line 1241, it appears to be a terrane bounding fault between the Hagmeister subterrane (of the Togiak terrane) and the Cape Pierce subterrane (of the Goodnews terrane), because on velocity models of line 1242 and line 1241, it vertically offsets the ophiolitic basement rocks of the Cape Pierce subterrane creating a graben-like feature (G2 on line 1242; and G6 on line 1241 in Figure 6, 7). This interpretation is consistent with the deep crustal OBS refraction velocity model of Lizarralde (1997) where a variation in basement velocity from 6.0 km/s to 5.6 km/s was observed at around 30 km. The Togiak-Tikchik fault might extend to a depth of 5-6 km based on the low velocity gradient observed in the OBS velocity model near the location of fault; seismicity data indicates that this fault is relatively inactive, especially beneath the Bering shelf offshore. Onshore, there are three shallow earthquakes with M≥4 recorded in the early 1990s along the trace of fault, as seen in Figure 9. Perhaps due to its curved geometry offshore, slip may have been distributed along a splay fault, denoted by fault ‘7’ (Figure 9), which intersects line 1242 at ~55 km and line 1241 at ~230 km. However, it is important to note that there could be other possible interpretations of Togiak-Tikchik fault: For example, the single fault may have terminated near the coast, and evolved into a number of splays offshore. Pratt (2012) showed that when a large strike-slip fault terminates, it commonly distributes in three stress regime (extension, shear and thrust). In the present context, the Togiak-Tikchik fault may behave in the same way, which is suggested by the line 1242 velocity model that indicates multiple splays denoted by features 1 and 7 (Figure 9). An alternative interpretation is that fault 1 may curve onshore, and not merge with Togiak-Tikchik fault.

8.2. Togiak terrane and Goodnews terrane

The Togiak terrane is composed of volcanic flows, coarse volcanoclastic breccias, tuffs and associated epiclastic rocks of Late Triassic through Early Cretaceous age, whereas the Goodnews terrane is considered to be an amalgamation of variably metamorphosed blocks of laminated tuff, chert, basalt, greywacke, limestone, gabbro and ultramafic rocks (Decker et. al., 1994). In the current study, both the above terranes are mainly constrained by tomographic velocity and satellite gravity map. Based on the interpretation of the T-TF (Togiak-Tikchik fault) as discussed earlier, we suggest that the Togiak terrane may lie south of this fault, i.e. the region between ‘M2’ and the T-TF fault denoted by ‘1’ in Figure 9, whereas the Goodnews terrane lies to the north of the T-TF fault. The satellite gravity map indicates that dense rocks are associated with a gravity anomaly >40 mgal, as shown in Figure 9, and this anomaly may be due to Goodnews terrane ophiolitic ultramafic rocks, which are common in this terrane.

8.3. East Kulukak fault

The EKF (East Kulukak fault) fault is one of the poorly documented faults of southwestern Alaska. On previously published geologic maps (Plafker and Berg, 1994; Wilson et al., 2013) of Alaska, It is generally shown as a thrust fault, but it is unclear whether this fault is a sub-terrane boundary fault between the Hagmeister and Kulukak sub-terranes as shown in Figure 9. In the current study, this fault was constrained by both tomographic velocity and satellite-derived gravity data and it is denoted by ‘2’ in Figure 9, but the fault doesn’t have a strong expression on the satellite gravity map. The EKF fault probably intersects line 1242 at ~65 km, line 1241 at ~210 km and line 1243, denoted by the dotted line at ~215 km.

8.4. Lake Clarke fault

The LCF (Lake Clarke fault) is a right lateral strike-slip fault onshore southwestern Alaska and considered to be the westernmost extension of the Castle Mountain fault (CMF). Aeromagnetic data over the fault reveal a north-trending band of magnetic anomalies that are right-laterally offset across the fault by approximately 26 km (Haeussler and Saltus, 2005). In the present study, the LCF is denoted by ‘5’, and its offshore extension is constrained mainly by satellite derived gravity data, as shown in Figure 9. The fault coincides with a steep gravity gradient, and may involve reverse motion (Christie-Blick and Biddle, 1985), i.e. thrusting, as it deviates into a more southerly orientation offshore southwestern Alaska. The LCF, cannot be traced onto the seismic lines, which indicates that the fault could terminate in the north-eastern part of the Bristol Bay basin or may extend south of the seismic reflection profiles.

8.5. Kahiltna flysch & Chilchitna fault

Using zircon geochronolgy, Hults et al. (2013) suggested that the Kahiltna flysch can be divided into two belts, the NKF (Northen Kahiltna flysch belt) and SKF (Southern Kahiltna flysch belt) as shown in Figure 2,9. The zircon data reveals that the southern flysch belt was derived from the Wrangellia composite terrane (Figure 1), whereas the northern flysch belt was derived from the terranes that make up the paleo-Alaskan margin. The CF (Chilchitna thrust fault) fault denoted by ‘3’ divide both NKF and SKF sedimentary deposits. In the current study, the location of the Kahiltna flysch is well constrained by the tomographic velocity models and aeromagnetic data. In the tomographic velocity models (Figure 6,7), the southern Kahiltna flysch (SKF) sedimentary deposits are associated with slightly higher velocities ~4800 m/s compare to northern Kahiltna flysch ~3300-4500 m/s. Here I suggest that the northern Kahiltna flysch (NKF) forms the sedimentary deposits found in the graben-like features identified on vertical sections of the tomographic velocity models (G1- G10 in Figure 6,7).

The southern Kahiltna flysch coincides with the southern Alaska magnetic trough (SAMT) aeromagnetic domain, and extends offshore where it is bounded by magnetic boundaries M1 and M2 (Figure 8) based on the interpretation of Saltus et al. (1999) discussed previously. The northern boundary M2 of the SAMT coincides with the Chilchitna fault (fault denoted by 3), whereas fault ‘4’ (unknown fault) coincides with southern boundary M1 of the SAMT across the seismic profiles, which may indicate that SKF is fault bounded. The CF fault denoted by 3 intersects line 1242 at ~120 km, line 1241 at ~140 km and line 1243 at ~135 km. The unknown fault denoted by 4 intersects line 1242 at ~160 km, line 1241 at ~120 km and line 1243 at ~110 km.

8.6. Peninsular terrane

The Peninsular terrane (Figure 1) is a Triassic to Jurassic island-arc complex that was accreted to the North America continent by the Early Cretaceous (Jones et al., 1987; Ridgway et al., 2002). These older terrane rocks show much less seismic character and are overlain by the Carapace strata (Worrall, 1991). Walker et al. (2003) using gravity modelling and seismic studies predicted that the Peninsular terrane probably extends north to km 175 on line 1241. They also estimated the Peninsular basement density to be 2.76 g/cm^3 immediately below the Eocene grabens by using gravity modelling studies. In the current study, the Peninsular terrane was mainly constrained by aeromagnetic data. The southern Alaska magnetic high (SAMH) spatially coincides with the Peninsular terrane in southwestern Alaska. The broad magnetic character of the SAMH crust is due to the mafic rocks of the Wrangellia and Peninsular arcs (Saltus et al., 2007). In Figure 9, the Peninsular terrane is defined as the region between the M1 and M4 aeromagnetic boundaries based on the interpretation of Saltus et al. (1999; 2003; 2007). However, it is important to note that these boundaries only predict the approximate surface location of the terrane. Magnetic boundary M1 coincides with unknown fault ‘4’ on line 1242, line 1241 and line 1243. The oroclinal geometry of the interpreted Peninsular terrane is probably associated with its accretion to the North American continent (Worrall, 1991).

8.7. Regional suture zone

In southcentral Alaska, Ridgway et al. (2002) proposed that the entire flysch belt between the Talkeetna fault and the Hines creek strand of the Denali fault represents a suture zone called as Alaska Range Suture Zone (ARSZ) (Figure 1). ARSZ coincides with the central portion of SAMT (Brennan et al., 2011) as previously described in section 7.1. Brennan et al. (2011) suggested that the ARSZ is a part of regional suture zone (RSZ) that extends from British Columbia to southwestern Alaska, but did not provide any boundaries for RSZ. The current study suggests possible boundaries for the RSZ which are mainly constrained by aeromagnetic data and satellite-derived gravity data. M3 in Figure 8 denotes the possible northern offshore boundary, M3, of the region of neutral magnetic character, which coincides with feature ‘6’ of the satellite altimetry gravity anomaly map (Figure 9). The region between the M3 and M2 magnetic boundaries may indicate the offshore extension of the RSZ (regional suture zone) which includes the entire ARSZ and the interior neutral magnetic domain (Figure 8).

9. Conclusions

The results provide evidence of the likely locations of the offshore extensions of the major geological elements of southwestern Alaska (Figure 10), and were derived from a wide range of geophysical data: seismic, ship-board gravity, ship-board magnetic, satellite altimetry gravity and airborne magnetics. Various individual and integrated geophysical maps (mean seismic velocity, ship-board gravity, ship-board magnetics and satellite-altimetry gravity) of the study area were created for use in this integrated interpretation. Based on the current study, we suggest the following:

1. Togiak-Tikchik fault (T-TF) extends offshore onto lines 1242 and 1241, and is a terrane bounding fault between the Hagmeister subterrane (Togiak terrane) and the Cape Pierce subterrane (Goodnews terrane)

2. East Kulukak fault (EKF) is a thrust fault that extends offshore and cross-cuts all seismic lines

3. Lake Clarke fault (LCF) extends offshore and curves into the northeastern part of the Bristol Bay basin

4. Chilchitna fault (CF) extends offshore, crosscuts all the seismic lines and coincides with the northern boundary of the southern Alaska magnetic trough (SAMT)

5. The unknown fault identified in the inner Bering shelf offshore, may be the possible extension of the onshore Mulchatna fault (Anderson et al., 2017),

6. Southern Kahiltna flysch (SKF) coincides with the southern Alaska magnetic trough (SAMT) aeromagnetic domain, and the northern Kahiltna flysch (NKF) forms the sedimentary fill of the graben-like features revealed by the vertical sections of the tomographic velocity models

7. Peninsular terrane coincides with the southern Alaska magnetic high (SAMH), and its northern boundary crosscuts all seismic lines

8. Togiak terrane extends offshore where it is defined by the region between T-TF and the northern boundary of SAMT

9. Goodnews terrane extends offshore and lies to north of the Togiak-Tikchik fault

10. Regional suture zone extends offshore and includes the entire ARSZ and the interior neutral magnetic domain.

Appendix:

1. Seismic Reflection Processing

The data processing was carried out using the Landmark Graphics ProMAX software package, and a typical seismic reflection processing sequence was used for all the seismic lines. Following the application of the acquisition geometry, the data were subject to trace editing, i.e. killing of noisy traces, and then band-pass filtering at 0-4-50-60 Hz based on a series of filter panel tests. To mute the direct wave and refractions, a laterally variable top mute was picked every 5 km from individual shot gathers; for example, when reflections are obscured by strong acoustic dispersive guided and Scholte waves, the mute stepped later at near offset traces, but when the reflections are not contaminated with noise, a simple near-liner mute function was used. Spherical divergence (1/distance) and time raised to power amplitude corrections (exponent of 0.5) were used to recover the amplitude decay of reflections in the dataset. A single deconvolution operator design window was picked from just below the first arrivals to later in the section. After testing different deconvolution algorithms (spiking deconvolution, ensemble deconvolution, minimum phase predictive deconvolution) with various parameters, a minimum phase predictive deconvolution with an operator length of 240ms and a gap of 24ms was applied to suppress the short period reverberations.

Then, a polygonal F-K filter was applied to eliminate coherent noise from the dataset. To mitigate artifact creation, an AGC (Automatic Gain Control) with an operator length of 500 ms was implemented before applying the F-K filter, which was then subsequently reversed. The deconvolved, F-K filtered gathers were then sorted to CDP (common depth point) gathers for velocity analysis. Velocity analysis was carried out using semblance velocity spectra every 250 CDP. Normal move-out correction was applied and final stack sections were created. In addition to the above processing steps, the final stacks from all the lines were subjected to further post–stack processing: predictive deconvolution with a 120 ms operator length and 12 ms gap was applied to suppress some remnant multiples in the section. For post-stack migration two algorithms, F-K phase-shift and Kirchhoff migration were tested. Post-stack Kirchhoff time migration with a maximum frequency of 60 Hz and maximum 45^0 dip angle was applied to all the lines because this algorithm is able to handle both vertical and laterally varying velocities along the seismic profiles reasonably well. The final migrated seismic reflection sections (Figure A1) were then scaled for display.

2 Tomographic inversion

The vertical and horizontal spacing of the velocity grid was 25 m. The starting model was extended to 10 horizontal grid points on either side of the models. Velocities above the seafloor were set to a constant value of 1480 m/s, a value which was estimated from the direct wave. Velocities just below the seafloor were assumed to linearly increase with depth. To ensure that the velocity models are tied at their intersection point, the same gradient of 3 m/s was chosen for all seismic lines.

A smooth 2-D starting velocity model (Figure A2) for all the seismic lines was generated by running the tomographic inversion for 3 iterations with strong smoothing constraints. We then tested various second derivative regularizing constraints for all the lines and selected the same regularizing smoothing constraint operator i.e. 1000*1000 (Pronto parameter) for all the lines to ensure consistency between intersecting lines. With these constraint values, the main structure of the final velocity models did not change significantly in the final iteration. In the next stage, the inversion was run using 30 iterations with the second derivative regularizing constraint operator relaxed to 1000*100, which reduced the RMS (root mean square) traveltime residuals from 60 ms to 15 ms for line 1241, 50 ms to 16 ms for line 1242, and 50 ms to 15 ms for line 1243. Additionally, a 50 * 50 m convolutional smoothing operator was applied to the updated slowness model between iterations to limit the introduction of any short wavelength variations into the velocity model. Plots of the ray density (Figure A3) in the final velocity models of all the lines indicate that rays are generally concentrated at the top of high velocity rocks where they are close to the seafloor, e.g. at depths of 500 – 700 m in the northern half of the models. However, in this region there are some locations where the rays penetrate more deeply, to depths greater than 1 km, due to the local presence of rocks with lower seismic velocities. Towards the southern ends of the models, the ray density increases in the upper 500 m, because the higher velocity rocks lie at depths >2000 m, which is beyond the depth of first-arrival penetration, and the recorded first-arrivals correspond to relatively shallow refractions.

3 Model consistency

3.1 1D profiles at line intersections

The two intersections, i.e. between 1241-1242 and 1242-1243 occur near the edges of the model. So to avoid discrepancies arising because of edge effects, the 1-D velocity profiles at these two intersections were chosen ~5 km away from the intersection point. Overall, the extracted 1D velocity profiles are generally similar (Figure A4) except a small difference was observed < 500 m depth at intersection 1241-1242 due to relatively higher velocities of line 1242 because of presence of ultramafic rocks at that location.

3.2. Well-tie with line 1241

In order to further assess the quality of the traveltime tomographic inversion, a comparison was made between the sonic log recorded in the COST-1 well and a 1-D velocity profile extracted from the velocity model for line 1241 where it intersected the well (Figure A5). Generally, a good match exists between the estimated velocities from traveltime inversion of line 1241 and sonic velocities from well log up to a depth of 1300 m, showing the reliability of the results. A mismatch, is however, evident below 1300 m, suggesting the model is not reliable below that depth, where the velocity model depth is not well constrained by rays. The relatively low sonic velocities compared to model velocities observed throughout the depth is may be due to borehole damage, velocity anisotropy and higher rock porosities in the vicinity of well. The possible reason for higher model velocities is because of strong lateral smoothing applied to the model at the inversion stage.

4. Corrugation tests

From the ray density (Figure A3), it is clear that propagating rays are concentrated in the high velocity rocks of the shallow basement, and for this reason the top of the basement and the overlying sediment velocities are likely to be well constrained by the traveltimes observations; the number of rays passing through a single 25 m by 25 m cell is usually over 100 and in places approaches 300. In other parts of the model where the basement is deep, the ray density falls below 75 and the degree of constraint is more difficult to assess. In the present context, the issue of lateral resolution in the final velocity model was addressed in a semi quantitative fashion by performing a corrugation test, essentially a 1-D version of a 2-D checkerboard test (Calvert et. al., 2003); the latter does not provide much useful information on vertical resolution when applied in the presence of large vertical velocity gradient in the vertical plane (Calvert et. al., 2003).

A series of corrugation tests was carried out to evaluate the resolution of the estimated final velocity models, and also the sensitivity of the tomographic inversion. Since the results of the corrugation tests are broadly similar for all three seismic lines, I show the results of these tests for line 1242, and discuss the implications for resolving features in the velocity models. The corrugation test typically consists of adding a small perturbation to the final velocity model, and then computing synthetic traveltimes by forward modelling all receivers and sources used in the inversion, followed by an inversion of these synthetic traveltimes using the same parameters as for the field data. The final velocity model is then subtracted from this inverted corrugation velocity model, leaving the regenerated corrugations shown in Figure A6 (b, d, and f). The resolution of the recovered model, both laterally, and as a function of depth, is then estimated based on how well the perturbed model is recovered. The ability to resolve velocity perturbations of a particular half-width (half of wavelength) or size varies throughout an estimated final velocity model, and it is usually greatest where a large number of propagation ray paths intersect at wide range of azimuths. The resolution tends to be poor if propagation ray paths are parallel to one another at a particular point in the model.

A perturbation to superimpose on the final velocity model was created that comprised a 1-D sinusoidal variation with a maximum amplitude that was 10% of the final model below the seafloor, but the velocity in the water layer was not varied. In the tests three different half-widths of sinusoidal variation were tested, 400 m, 800 m and 1600 m (Figure A6(a,c,e)). The velocity perturbation with a half-width of 400 m is very poorly recovered, but the perturbation with a half width of 800 m was recovered well to a depths of 200 m where the top of the basement was shallow, and to depths of 900 m where the basement was much deeper. With a half-width of 1600 m, the superimposed perturbation was recovered to approximately 500 m depth where the basement is shallow, but down to almost 2000 m where it is deep. The above tests reveal that the ability to resolve velocity anomalies at increasing depth. The main focus of the interpretation is the larger-scale velocity variations, particularly where the basement is shallow. Therefore regions of lower velocity in the models that extend laterally over at least 1600 m are well constrained.

5. Derivation of Mean velocity slices

To distinguish different terranes and locate structural variation associated with top of the igneous basement, mean tomographic velocities were calculated over various depth ranges to characterize the lateral velocity variation (Figure A7). When displayed in map view, the mean velocity can be used to reveal lateral variations in velocity, allowing the correlation of velocity discontinuities and near-surface geology from one line to another.

The mean velocity over a shallow depth range (from 0-125 m below the seafloor) does not reveal any significant lateral variations in velocity along profiles 1241, 1242 and 1243. So, I tested four different scenarios for selecting an optimal velocity contour to serve as a starting depth for estimating the mean velocity over a 125 m depth range: 1) 2000 m/s 2) 3000 m/s 3) 4000 m/s 4) 5000 m/s as shown in Figure A7. Higher mean velocities indicate where the interval velocity has increased rapidly below the specified isovelocity contour. From Figure A7, it can be clearly seen that by selecting the 2000 m/s and 3000 m/s contours, estimated mean velocities are less than 3800 m/s, and are associated mostly with sediments. In contrast, the 4000 m/s velocity contour yields higher mean velocities that reveal lateral velocity variations close to the top of basement; the largest mean velocities, e.g. 5000 m/s at the north end of line 1242, indicate a rapid downward increase in seismic velocity that probably corresponds closely to the sediment-basement interface; lower velocities, e.g. 4200-4400 m/s near 100 km on line 1242, show a less rapid downward increase in velocity that likely marks the location of high velocity sedimentary rocks just above the igneous basement, such as pre-Eocene sedimentary rocks filling the graben-like structures. Using the 5000 m/s contour produces a comparable degree of lateral velocity variation to the 4000 m/s contour where the basement is shallow, but is less reliable where the basement is deep due to limited ray penetration.

6. Ship-board data

Along with multichannel seismic reflection data (lines 1241, 1242 and 1243), ship-board gravity and magnetic data were also collected during the 1994 Maurice Ewing "EW9409" cruise. These datasets are useful in delineating short-wavelength anomalies originating from sources at shallow-depths. And sometimes, shiptrack datasets serve as ground truth for the calibration of satellite-derived global grids (Sandwell et al., 2014). Apart from the current cruise trackline, we have also included gravity and magnetic datasets from other near-by cruise tracklines: BBAY212 (1970), L576BS (1976), L982BS (1982). But, in the following figures, the L982BS trackline data are not shown, because of its inconsistency with near-by tracklines.

6.1. Gravity

The ship-board free-air gravity anomaly plotted in Figure A8 suggests significant lateral variation in the density of rocks along the seismic profiles. The gravity low <30 mGal observed towards the south of the seismic lines indicates the presence of a thick layer of Quaternary sediment cover. The gravity high >40 mGal may indicate the presence of high density Mesozoic igneous basement. Most discontinuities in the gravity anomaly map coincide with faults inferred from the tomographic velocity models as indicated by numbers 1-4 on Figure A8.

6.2. Magnetic

The ship-board residual magnetic field intensity is overlain on top of the topographic map in Figure A9. The lateral extent of residual magnetic field anomalies depends mainly on the depth to the source. The shallower the depth of a body, the higher the amplitude, the shorter the wavelength, and the sharper the gradients of the anomaly.

In the Figure A9, magnetic highs > 200 nT were observed towards the south end of the seismic profiles as denoted by feature 'A', which may indicate mafic and ultramafic rocks of the Peninsular arc terrane. This is consistent with airborne magnetic data discussed previously. To the north, shorter wavelength anomalies with sharper gradients were observed which may be due to lateral variations of shallow intrusive igneous rocks. These features are generally consistent with the strong lateral variation of velocities along the seismic profiles. Faults 1-4 which are inferred from velocity discontinuities coincide with sharp magnetic gradients as shown in Figure A9.

Acknowledgments

This project was carried out at Simon Fraser University as part of PhD thesis funded by the Natural Sciences and Engineering Research Council of Canada. We thank David F Aldridge and Douglas Oldenburg for giving permission to use the tomography code PRONTO. We used Landmark Graphics ProMAX for seismic data processing, Seismic Unix for plotting velocity models and Generic Mapping Tools (GMT) for plotting geophysical maps. We thank Dr Nathan Hayward for helpful comments and suggestions. We also thank Prof. Richard Smith for providing Seequent Geosoft license for plotting airborne magnetic data.

Data Availability Statement

Multi-channel seismic reflection data, ship-board gravity and magnetic datasets used in this study are publicly available on the Marine Geoscience Data System repository and can be downloaded through (https://www.marine-geo.org/tools/search). Seismicity data are freely available through USGS earthquake catalogue and can be accessed with the following URL (https://earthquake.usgs.gov/earthquakes/search).The global 1-minute grid satellite-derived free-air gravity anomaly is freely available for download through the following URL (https://topex.ucsd.edu/cgi-bin/get_data.cgi), (Sandwell et al., 2014). North America magnetic anomaly is freely available to download from USGS mineral resources website (https://mrdata.usgs.gov/magnetic/) or can also be accessed through Seequent Geosoft public DAP server (https://dap.geosoft.com). Seafloor bathymetry and topography data were downloaded from the Global Multi-Resolution Topography dataset through the National Geophysical Data Center website with following link (https://ngdc.noaa.gov/mgg/topo/). COST-1 well log is available from National Geophysical Data Center well log catalogue (https://ngdc.noaa.gov/mgg/announcements/welllogs.html). PRONTO traveltime tomographic inversion code is available from (Aldridge and Oldenburg (1993), https://www.geo.umass.edu/faculty/wclement/ProntoDocs/Docs/pronto.html). Seismic data processing was carried out using Halliburton Landmark Graphics ProMAX software commercial package (https://www.halliburton.com/en/software). 2D checkerboard test code is available from (Calvert et.al., 2003). Most map figures were produced using the Generic Mapping Tools package (GMT) version 5 (Wessel et al., 2013). Seismic velocity models are plotted using Seismic Unix open source software package downloaded using the following URL (https://github.com/JohnWStockwllJr/SeisUnix).

References

Aldridge, D. F., and Oldenburg, D. (1993), Two-dimensional tomography inversion with finite-difference traveltimes: Journal of Seismic Exploration, 2, 257–274.

Anderson, E.D., Monecke, T., Hitzman, M.W., Zhou, W. and Bedrosian, P.A. (2017), Mineral Potential Mapping in an Accreted Island-Arc Setting Using Aeromagnetic Data: An Example from Southwest Alaska: Economic Geology, 112, 375-396.

Barnes, D.F. (1976), Bouguer gravity map of Alaska: U.S. Geological Survey Open-File Report, 76-70, scale 1:2,500,000 with text and inset maps.

Box, S. E. (1985), Terrane analysis of the northern Bristol Bay region, southwestern Alaska: U.S. Geological Survey Circular, 967, 32-37.

Brennan, P.R., Gilbert, H. and Ridgway, K.D. (2011), Crustal structure across the central Alaska Range: Anatomy of a Mesozoic collisional zone: Geochemistry, Geophysics, Geosystems., 12, Q04010.

Calvert, A. J., Fisher M. A. and Johnson S. P. (2003), Along-strike variations in the shallow seismic velocity structure of the Seattle fault zone: Evidence for fault segmentation beneath Puget Sound: Journal of Geophysical Research, 102, 5119-5133.

Chang, J. M., Feeley, T. C. and Deraps, M. R. (2009), Petrogenesis of basaltic volcanic rocks from the Pribilof Islands, Alaska, by melting of metasomatically enriched depleted lithosphere, crystallization differentiation, and magma mixing: Journal of Petrology, 50, 2249-2286.

Christie-Blick, N., and Biddle, K. T. (1985), Deformation and basin formation along strike-slip faults: Society of Economic Paleontologists and Mineralogists Special Publication 37, 1-34.

Cole, R.B., Nelson, S.W., Layer, P.W., and Oswald, P.J. (2006), Eocene volcanism above a depleted mantle slab window in southern Alaska: Geological Society of America Bulletin, 118, 140–158.

Cole, R.B., Ridgway, K.D., Layer, P.W., and Drake, J. (1999), Kinematics of basin development during the transition from terrane accretion to strike-slip tectonics, Late Cretaceous early Tertiary Cantwell Formation, south central Alaska: Tectonics, 18, 1224–1244.

Coney, P.J., and Jones, D.L. (1985), Accretion tectonics and crustal structure in Alaska: Tectonophysics, 119, 165–283.

Coney, P.J., Jones, D.L. and Monger, J.W. (1980), Cordilleran suspect terranes: Nature, 288, 329-333.

Cooper, A.K., Scholl, D.W. and Marlow, M.S., (1976), Plate tectonic model for the evolution of the eastern Bering Sea Basin: Geological Society of America Bulletin, 87, 1119-1126.

Cross, R.S. and Freymueller, J.T. (2008), Evidence for and implications of a bering plate based on geodetic measurements from the aleutians and western Alaska: Journal of Geophysical Research, 113, B07405.

Decker, J., Bergman, S. C., Blodgett, R. B., Box, S. E., Bundtzen, T. K., Clough, J. G., Coonrad, W. L., Gilbert, W. G., Miller, M. L., Murphy, J. M., Robinson, M. S., and Wallace, W. K. (1994), Geology of southwestern Alaska: in Plafker, G., and Berg, H. C., eds., The Geology of Alaska: Boulder, Colorado, Geological Society of America, The Geology of North America, G-1.

Detterman, R.L. and Reed, B.L. (1980), Stratigraphy, structure, and economic geology of the Iliamna quadrangle: Alaska (No. 1368-B). Govt. Print. Off.

Eisbacher, G.H. (1976), Sedimentology of the Dezadeash flysch and its implications for strike-slip faulting along the Denali fault, Yukon Territory and Alaska: Canadian Journal of Earth Sciences, 13, 1495–1513.

Finzel, E. S., Ridgway, K. D., Reifenstuhl, R. R., Blodgett, R. B., White, J. M., and Decker, P. L. (2009), Stratigraphic framework and estuarine depositional environments of the Miocene Bear Lake Formation, Bristol Bay Basin, Alaska: onshore equivalents to potential reservoir strata in a frontier gas-rich basin: American Association of Petroleum Geologists Bulletin, 93, 379-405.

Finzel, E.S. (2011), Kinematics of a diffuse North America-Pacific-Bering plate boundary in Alaska and western Canada: Geology, 39, 835-838.

Finzel, E.S., Reifenstuhl, R.R., Decker, P.L., and Ridgway, K.D. (2005), Sedimentology, stratigraphy, and hydrocarbon reservoir—source rock potential, using surface and subsurface data, of Tertiary and Mesozoic strata, Bristol Bay basin and Alaska Peninsula: Alaska Division of Geological & Geophysical Surveys Preliminary Interpretive Report, 4, 1-67.

Fisher, M.A. Pellerin, L. Nokleberg, W.J. Ratchkovski, N.A. Glen, J.M.G. (2007), Crustal structure of the Alaska Range orogen and Denali fault along the Richardson Highway: Geological Society of America Special Paper, 431, 43-53.

Fisher, M.A., Patton Jr, W.W. and Holmes, M.L. (1982), Geology of Norton Basin and continental shelf beneath northwestern Bering Sea, Alaska: American Association of Petroleum Geologists Bulletin, 66, 255-285.

Fitzgerald, P.G., Roeske, S.M., Benowitz, J.A., Riccio, S.J., Perry, S.E. and Armstrong, P.A. (2014), Alternating asymmetric topography of the Alaska range along the strike-slip Denali fault: Strain partitioning and lithospheric control across a terrane suture zone: Tectonics, 33, 1519-1533.

Godson, R.H. (1994), Composite magnetic anomaly map of Alaska and adjacent offshore areas, in Plafker, George, and Berg, H.C., eds., The Geology of Alaska: Geological Society of America, 1 sheet, scale 1:2,500,000.

Haeussler, P.J., and Saltus, R.W. (2005), 26 km of offset on the Lake Clarke Fault since late Eocene time, in Haeussler, P.J., and Galloway, J.P., eds., Studies by the U.S. Geological Survey in Alaska, 2004: U.S. Geological Survey Professional Paper 1709-A, 1-4.

Hatten, C.W. (1971), Petroleum potential of Bristol Bay basin, Alaska: American Association of Petroleum Geologists Memoir, 15, 105-108.

Hillhouse, J.W. (1987), Accretion of southern Alaska: Tectonophysics, 139, 107–122.

Hults, C.P., Wilson, F.H., Donelick, R.A. and O’Sullivan, P.B. (2013), Two flysch belts having distinctly different provenance suggest no stratigraphic link between the Wrangellia composite terrane and the paleo-Alaskan margin: Lithosphere, 5, 575-594.

Jones D.L., Silberling N.J., Coeny P.J. and Plafker G. (1987), Lithotectonic terrane map of Alaska (west of the 41st meridian): U.S. Geological Survey Miscellaneous Field Studies Map MF-1874-A, scale 1:2,500,000.

Jones, D. L, and Silberling, N. J. (1979), Mesozoic stratigraphy; The key to tectonic analysis of southern and central Alaska: U.S. Geological Survey Open-File Report 79- 1200, 1-41.

Jones, D.L., Silberling, N.J., and Hillhouse, J. (1977), Wrangellia-A displaced terrane in northwestern North America: Canadian Journal of Earth Sciences, 14, 2565–2577.

Klemperer, S.L., Miller, E.L., Grantz, A., Scholl, D.W. and Bering-Chukchi Working Group, (2002a), Crustal structure of the Bering and Chukchi shelves: Deep seismic reflection profiles across the North American continent between Alaska and Russia, in Tectonic Evolution of the Bering Shelf – Chukchi Sea –Arctic Margin and Adjacent Landmasses, edited by E. L. Miller, A. Grantz, and S. L. Klempere: Geological Society of America Special Papers, 360, 1 – 24.

Lizarralde, D. (1997), Crustal Structure of rifted and convergent Margins: The US East Coast and Aleutian Margins: Ph.D. thesis, MIT/WHOI joint program, nMassachusetts Inst of Tech Cambridge.

Marlow, M. S., Cooper, A.K. and Fisher, M.A. (1994), Geology of the eastern Bering Sea continental shelf: The Geology of North America, vol G-1 ,in: G Plafker, H.C Berg, Editors , The Geology of Alaska, Geological Society of America, Boulder, CO, 271–284.

Marlow, M.S., 1979, Hydrocarbon prospects in Navarin basin province, northwest Bering Sea shelf: Oil and Gas Journal, October, 29, 190-196.

Marlow, M.S., Cooper, A.K. and Childs, J.R. (1983), Tectonic evolution of Gulf of Anadyr and formation of Anadyr and Navarin basins: American Association of Petroleum Geologists Bulletin, 67, 646-665.

Meyer, J.F., Jr., and Saltus, R.W. (1995), Merged aeromagnetic map of interior Alaska: U.S. Geological Survey Geophysical Investigations Map 1014, 2 sheets, scale 1:500,000.

Miller, M.L. Bradley, D.C. Bundtzen, T.K. Blodgett, R.B. Pessagno, E.A. Tucker, R.D. Harris, A.G. (2007), The restricted Gemuk Group: A Triassic to Lower Cretaceous succession in southwestern Alaska: Geological Society of America Special Paper, 431, 273-305.

Nokleberg, W.J. and Richter, D.H. (2007), Origin of narrow terranes and adjacent major terranes occurring along the Denali fault in the Eastern and Central Alaska Range, Alaska: Geological Society of America Special Papers, 431, 129-154.

Nokleberg, W.J., Jones, D.L., and Silberling, N.J. (1985), Origin and tectonic evolution of the Maclaren and Wrangellia terranes, eastern Alaska Range, Alaska: Geological Society of America Bulletin, 96, 1251–1270.

Nokleberg, W.J., Plafker, G., and Wilson, F.H. (1994), Geology of south-central Alaska: in Plafker, G., and Berg, H.C., eds., The geology of Alaska: Boulder, Colorado, Geological Society of America, Geology of North America, G-1, 311–366.

Plafker, G., and Berg, H.C. (1994), Overview of the geology and tectonic evolution of Alaska: in Plafker, G., and Berg, H.C., eds., The Geology of Alaska: Boulder, Colorado: Geological Society of America, Geology of North America, G-1, 989–1021.

Plafker, G., Moore, J.C., and Winkler, G.R. (1994), Geology of the southern Alaska margin: in Plafker, G., and Berg, H.C., eds., The Geology of Alaska: Boulder, Colorado: Geological Society of America, Geology of North America, G-1, 389–449.

Plafker, G., Nokleberg, W.J., and Lull, J.S. (1989), Bedrock geology and tectonic evolution of the Wrangellia, Peninsular, and Chugach terranes along the trans-Alaska crustal transect in the northern Chugach Mountains and southern Copper River basin: Journal of Geophysical Research, 94, 4255–4295.

Pratt, T.L. (2012), Large-scale splay faults on a strike-slip fault system: The Yakima folds, Washington State: Geochemistry, Geophysics, Geosystems. 13, Q11004.

Reed B.L., Miesch A.T. and Lanphere M.A. (1983), Plutonic rocks of Jurassic age in the Alaska-Aleutian Range batholith: Chemical variations and polarity: Geological Society of America Bulletin, 94, 1232–1240.

Ridgway, K.D., Trop, J.M., Nokleberg, W.J., Davidson, C.M., and Eastham, K.R. (2002), Mesozoic and Cenozoic tectonics of the eastern and central Alaska Range: Progressive basin development and deformation in a suture zone: Geological Society of America Bulletin, 114, 1480–1504.

Rioux M.B., Mattinson J.M., Hacker B., Kelemen P.B., Blusztajn J., Hanghoj K. and Gehrels G. (2010), Intermediate to felsic middle crust in the accreted Talkeetna arc, the Alaska Peninsula and Kodiak Island, Alaska: An analogue for low-velocity middle crust in modern arcs: Tectonics, 29, TC3001.

Saltus, R.W., Hill, P.L., Connard, G.G., Hudson, T.L., and Barnett, A. (1999), Building a Magnetic View of Alaska: U.S. Geological Survey Open-File Report 99-0418.

Saltus, R.W., Hudson, T.L. and Wilson, F.H. (2003), Geophysical identification and geological implications of the southern Alaska magnetic trough: US Department of the Interior, US Geological Survey.

Saltus, R.W., Hudson, T.L., and Wilson, F.H. (2007), The geophysical character of southern Alaska—Implications for crustal evolution, in Ridgway, K.D., Trop, J.M., Glen, J.M.G., and O’Neill, J.M., eds., Tectonic Growth of a Collisional Continental Margin: Crustal Evolution of Southern Alaska: Geological Society of America Special Paper 431, 1–20.

Saltus, R.W., Meyer, J.F., Barnes, D.F., and Morin, R.L. (1997), Tectono-geophysical domains of interior Alaska as interpreted from new gravity and aeromagnetic data compilations: in

Dumoulin, J.A., and Gray, J.E., eds., Geologic studies in Alaska by the U.S. Geological Survey, 1995: U.S. Geological Survey Professional Paper 1574, 157-171.

Sandwell, D.T., Müller, R.D., Smith, W.H., Garcia, E. and Francis, R. (2014), New global marine gravity model from CryoSat-2 and Jason-1 reveals buried tectonic structure: Science, 346, 65-67.

Scholl, D.W., Vallier, T.L. and Stevenson, A.J. (1986), Terrane accretion, production, and continental growth: A perspective based on the origin and tectonic fate of the Aleutian–Bering Sea region: Geology, 14, 43-47.

Sherwood, K.W., Larson, J., Comer, C.D., Craig, J.D. and Reitmeier, C. (2006), North Aleutian Basin OCS planning area: assessment of undiscovered technically-recoverable oil and gas, as of 2006. (https://www.boem.gov/uploadedFiles/BOEM/About_BOEM/BOEM_Regions/Alaska_Region/Resource_Evaluation/North-Aleutian-Basin-Assessment-Report.pdf)

Trop, J.M., and Ridgway, K.D. (2007), Mesozoic and Cenozoic tectonic growth of southern Alaska: A sedimentary basin perspective, in Ridgway, K.D., Trop, J.M., Glen, J.M.G., and O'Neill, J.M., eds., Tectonic Growth of a Collisional Continental Margin: Crustal Evolution of Southern Alaska: Geological Society of America Special Paper, 431, 55–94.

Turner, R. F. (1988), Geological and operational summary, North Aleutian Shelf COST No. 1 Well, Bering Sea, Alaska: 1-256, U.S. Dept. of the Interior, Mineral Management Service, Alaska OCS Region, Anchorage.

Vayavur, R. (2017). Seismic and potential field constraints on the shallow crustal structure of inner Bering shelf, offshore southwestern Alaska, Ph.D. thesis, Simon Fraser University, 155 p.

Vayavur, R., and Calvert, A. J. (2016), "Mitigation of guided wave contamination in waveform tomography of marine seismic reflection data from southwestern Alaska," Geophysics 81: B101-B118

Walker, K.T., McGeary, S.E., and Klemperer, S.L. (2003), Tectonic evolution of the Bristol Bay basin, southeast Bering Sea: Constraints from seismic reflection and potential field data: Tectonics, 22, 19.

Wallace, W.K., Hanks, C.L., and Rogers, J.F. (1989), The southern Kahiltna terrane: Implications for the tectonic evolution of southwestern Alaska: Geological Society of America Bulletin, 101, 1389–1407.

Wessel, P., Smith, W. H. F., Scharroo, R., Luis, J and Wobbe, F., (2013), Generic Mapping Tools: Improved version Released, EOS Trans. AGU, 94(45), p. 409-410, 2013.

Wilson, F.H., Hults, C.P., Mohadjer, Solmaz, and Coonrad, W.L., comps. (2013), Reconnaissance geologic map of the Kuskokwim Bay region, southwest Alaska: U.S. Geological Survey Scientific Investigations Map 3100, 1-46.

Wirth, K. R., Grandy, J., Kelley, K. and Sadofsky, S. (2002), Evolution of crust and mantle beneath the Bering Sea region: evidence from xenoliths and late Cenozoic basalts: Geological Society of America Special Papers., 360, in: E.L Miller, A Grantz, S.L Klemperer, Editors, Tectonic Evolution of the Bering Shelf-Chukchi Sea-Arctic Margin and Adjacent Landmasses, 167–194.

Worrall, D.M. (1991), Tectonic history of the Bering Sea and the evolution of Tertiary strike-slip basins of the Bering Shelf: Geological Society of America Special Papers, 257, 1-120.

Figure Captions

Figure 1. Composite terranes of southern Alaska (Terranes modified after Plafker and Berg, 1994). DF-Denali fault, TF-Tintina fault, FF-Fairweather fault, KF-Kaltag fault, INF-Iditarod-Nixon Fork fault, CMF-Castle mountain fault, T-TF-Togiak-Tikchik fault, BRF-Border Ranges fault, HCF- Hines Creek fault, MF-Mckinley fault, TKF-Talkeetna thrust fault, EKF-East Kulukak fault, LCF-Lake Clarke fault. Faults modified after Chang et al. (2009). Alaska Range Suture Zone (ARSZ) and Kahiltna Flysch adapted after (Ridgway et al., 2002).

Figure 2. Topography of the study area with seismicity overlaid. Alaska Range Suture Zone (ARSZ), North Kahiltna Flysch (NKF), and South Kahiltna Flysch (SKF) adapted after (Hults et al., 2013). White star offshore denotes COST well. DF (Denali fault), T-TF (Togiak-Tikchik fault), CMF (Castle Mountain fault), and LCF (Lake Clarke fault) are right-lateral strike-slip faults. EKF (East Kulukak fault), TKF (Talkeetna thrust fault), and CF (Chilchitna fault) are thrust faults.

Figure 3. Final velocity models obtained after final stage of tomographic inversion.

Figure 4. Traveltime residual plots a) line 1241 b) line 1242 c) line 1243. DB: deep basement, SB: shallow basement.

Figure 5. Velocity from COST-1 well sonic log (truncated to 4 km), and after median filtering and sub-sampling to 0.01 km sample interval. Velocity at the red event unconformity was estimated to be approximately 3.1 – 3.3 km/s. There is a good match with the tomographic velocity model above 1.3 km, but the deeper model is not well constrained. The corresponding lithostratigraphy chart was taken from BOEM (Bureau of Ocean Energy Management) 2009 report (https://www.boem.gov/About-BOEM/BOEM-Regions/Alaska-Region/Resource-Evaluation/north-aleutian-shelf-COST.aspx). Letters A, B1, B2, C, D, and E denote the units identified by Walker et al., (2003) using well log correlation with seismic.

Figure 6. Joint interpretation of velocity images overlaid on migrated seismic reflection sections a) line 1242 b) line 1241 c) line 1243. Black star on line 1241 denotes the location of COST-1

well log. A, B1, B2, C, D, and E denotes the units identified by Walker et al., (2003). Small white squares denotes the intersection point of layer boundaries with well log. Black lines on seismic reflection sections denote faults inferred from small reflection offsets and white line represents interpreted basement. Numbers 1-4, 7 represent faults identified from velocity discontinuities. The orange lines denote location of high velocity rocks with velocities equal to 5.9 - 6.0 km/s. The inverted arrows represent the locations of line intersections, G1-G10 represents graben-like features, and M1, M2 represent aeromagnetic boundaries, PT-Peninsular Terrane, SKF-South Kahiltna Flysch, TT-Togiak terrane, GT- Goodnews terrane, RSZ – Regional Suture Zone.

Figure 7. Basement characterization along the seismic profiles: a) 1242 b) 1241 c) 1243 done by using traveltime inversion velocity constraints. The orange lines denote location of high velocity rocks with velocities equal to 5.9 - 6.0 km/s. Numbers 1-4 and 7 represent faults identified from velocity discontinuities. The inverted arrows represent the locations of line intersections, G1-G10 represents graben-like features, M1 and M2 represents aeromagnetic boundaries, PT-Peninsular Terrane, SKF-South Kahiltna Flysch, TT-Togiak terrane, GT- Goodnews terrane, RSZ – Regional Suture Zone.

Figure 8. Residual total intensity magnetic anomaly map of Alaska. The thick red lines M2, M1 and M4 are boundaries of SAMT and SAMH magnetic domains modified after (Saltus et al., 1999; Saltus et al., 2003). The dotted line M3 is proposed northern boundary of the interior neutral magnetic domain from the present work. RSZ- regional suture zone, SAMT- southern Alaska magnetic trough, SAMH –southern Alaska magnetic high.

Figure 9. Overlay of mean velocities on satellite derived free air gravity anomaly map. The color circles represents earthquake epicenters. White numbers denote possible offshore extensions: 1- T-TF (Togiak-Tikchik dextral strike-slip fault), 2- EKF (East Kulukak thrust fault), 3- CF (Chilchitna thrust fault), 4- unknown fault and 5- LCF (Lake Clarke dextral strike-slip fault), 6- arcuate feature which indicate possible offshore extension of regional suture zone boundary (RSZ), 7- possible splay fault of (T-TF)Togiak-Tikchik dextral strike-slip fault. The white dotted lines offshore represent predicted directions of major geological elements constrained by data from seismic, potential-field (ship-board, airborne, satellite) and regional geology. DF- Denali fault, CMF- Castle Mountain fault, PT-peninsular terrane, SKF-southern Kahiltna flysch, TT-Togiak terrane, GT- Good news terrane, SAMT-southern Alaska magnetic trough, SAMH-southern Alaska magnetic high, ARSZ-Alaska range suture zone, M1-M4 red dotted lines denote aeromagnetic boundaries. The numbers along the profiles denotes the distance in km. For the legend, refer to Figure 2.

Figure 10. Simplified map showing probable offshore extensions of major geologic elements of southwestern Alaska. Black dotted lines denote the offshore continuation of faults mapped onshore: 1- T-TF (Togiak-Tikchik dextral strike-slip fault), 2-EKF (East Kulukak thrust fault), 3- CF (Chilchitna thrust fault), 4 – unknown fault and 5- LCF (Lake Clarke dextral strike-slip fault), 6-arcuate feature which indicate possible offshore extension of regional suture zone boundary (RSZ), 7- possible splay fault of (T-TF)Togiak-Tikchik dextral strike-slip fault. The dashed red lines are the predicted boundaries of major geological elements constrained by data from seismic, potential-field (ship-board, airborne, satellite) and regional geology. DF- Denali fault, CMF- Castle Mountain fault, PT-Peninsular terrane, SKF-Southern Kahiltna Flysch, TT-

Togiak terrane, GT- Good news terrane, SAMT-southern Alaska magnetic trough, SAMH-southern Alaska magnetic high, ARSZ-Alaska range suture zone, M1-M4 denote aeromagnetic boundaries. The color circles represents earthquake epicenters. The numbers along the profiles denotes the distance in km. For the legend, refer to Figure 2.

Figure A1. Post-stack migrated time sections: a) line 1242 b) line 1241 c) line 1243. DB: deep basement, SB: shallow basement

Figure A2. 2-D starting models for lines 1241, 1242, and 1243. DB: Deep basement, SB: Shallow basement.

Figure A3. Ray density maps for lines 1241, 1242, and 1243. DB: Deep basement, SB: Shallow basement.

Figure A4. 1-D profiles at intersection point of lines a) 1241-1243 b) 1242-1243 c) 1241-1242.

Figure A5. Comparison of COST-1 well sonic log with velocities estimated at well location of line 1241.

Figure A6. Corrugation tests for line 1242 using a 1-D vertical sinusoidal perturbation below the seafloor: a) original perturbation with 400 m half-width in area of ray coverage, b) recovered 400 m perturbation, c) original perturbation with 800 m half-width in area of ray coverage, d) recovered 800 m perturbation, e) original perturbation with 1600 m half-width in area of ray coverage, f) recovered 1600 m perturbation. DB: deep basement, SB: shallow basement

Figure A7. Mean velocity along the profiles 1241, 1242 and 1243 estimated using different velocity contours a) 2000 m/s b) 3000 m/s c) 4000 m/s d) 5000 m/s as initial depth. The velocities below these contours are averaged over a thickness of 125 m. Mean velocity estimated using 4000 m/s shows good lateral velocity variation of the subsurface. No data along the profiles indicates absence of ray coverage. The numbers along the profiles denotes the distance in km.

Figure A8. Overlay of ship-board gravity anomaly on topography map. The color circles represent earthquake epicenters. White numbers denote the possible offshore extensions: 1- T-TF (Togiak-Tikchik dextral strike-slip fault), 2-EKF (East Kulukak thrust fault), 3- CF (Chilchitna thrust fault), 4- unknown fault and 5- LCF (Lake Clarke dextral strike-slip fault), 6-arcuate feature which indicate possible offshore extension of regional suture zone boundary (RSZ), 7-possible splay fault of (T-TF) Togiak-Tikchik dextral strike-slip fault. The white dotted lines offshore are predicted directions of major geological elements constrained by data from seismic, potential-field (ship-board, airborne, satellite) and regional geology. DF- Denali fault, CMF-Castle Mountain fault, PT- peninsular terrane, SKF- southern Kahiltna flysch, TT- Togiak terrane, GT- Good news terrane, SAMT- southern Alaska magnetic trough, SAMH- southern Alaska magnetic high, ARSZ- Alaska range suture zone, M1-M4 red dotted lines denote aeromagnetic boundaries. The numbers along the profiles denotes the distance in km. For the legend, refer to Figure 2

Figure A9. Overlay of ship-board residual magnetic anomaly map on topography map. The color circles represent earthquake epicenters. White numbers denote the possible offshore extensions: 1- T-TF (Togiak-Tikchik dextral strike-slip fault), 2-EKF (East Kulukak thrust fault), 3- CF (Chilchitna thrust fault), 4- unknown fault and 5- LCF (Lake Clarke dextral strike-slip fault), 6-arcuate feature which indicate possible offshore extension of regional suture zone boundary (RSZ), 7- possible splay fault of (T-TF) Togiak-Tikchik dextral strike-slip fault. The white dotted lines offshore are predicted directions of major geological elements constrained by data from seismic, potential-field (ship-board, airborne, satellite) and regional geology. DF-Denali fault, CMF- Castle Mountain fault, PT- peninsular terrane, SKF- southern Kahiltna flysch, TT- Togiak terrane, GT- Good news terrane, SAMT- southern Alaska magnetic trough, SAMH- southern Alaska magnetic high, ARSZ- Alaska range suture zone, M1-M4 red dotted lines denote aeromagnetic boundaries. The numbers along the profiles denotes the distance in km. For the legend, refer to Figure 2.

Figure 1.

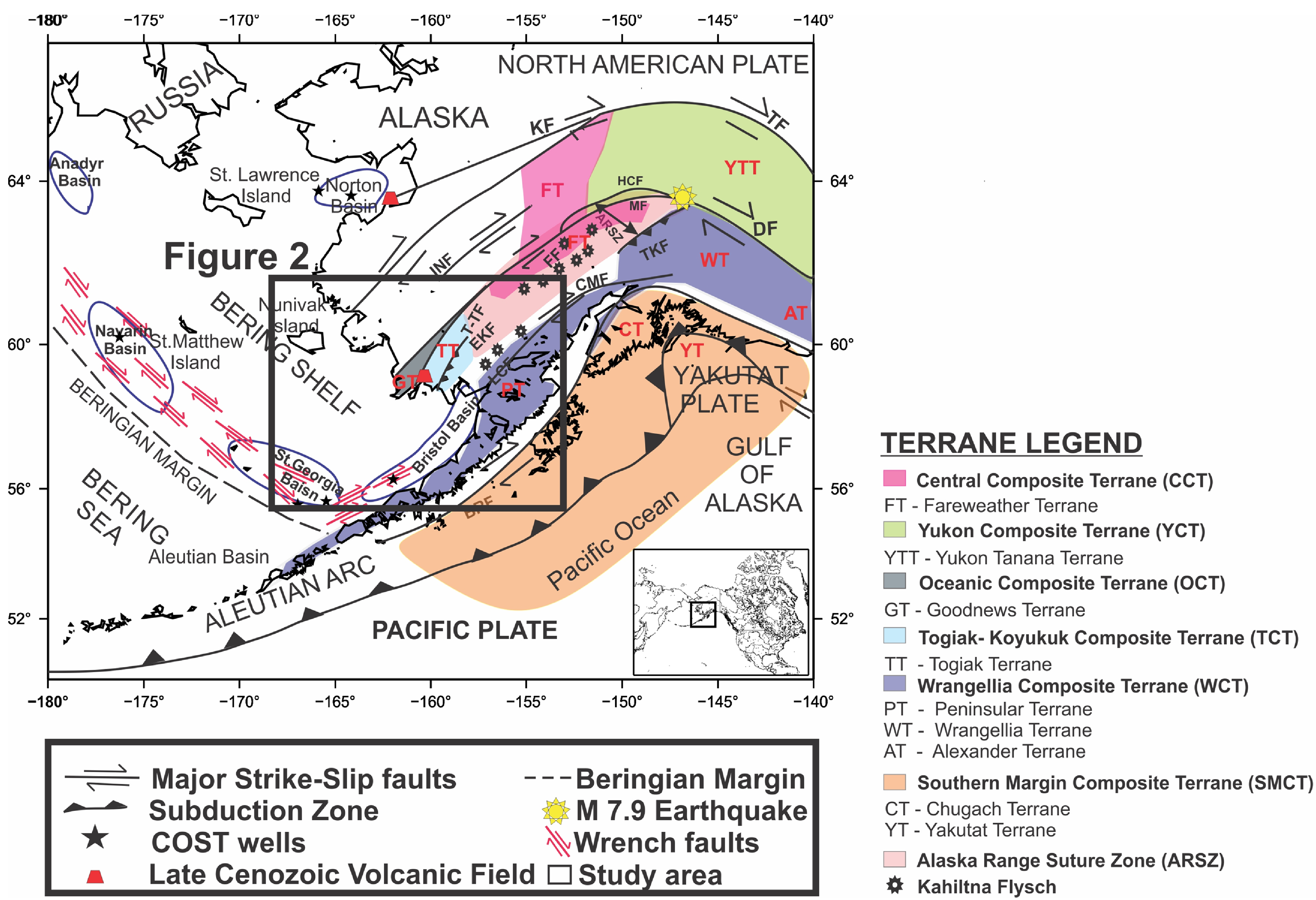
Figure 2
RUSSIA
ALASKA
NORTH AMERICAN PLATE
Anadyr Basin
St. Lawrence Island
Norton Basin
Navarin Basin
St.Matthew Island
Nunivak Island
BERING SHELF
BERINGIAN MARGIN
BERING SEA
Aleutian Basin
St.Georgia Baisn
Bristol Basin
ALEUTIAN ARC
PACIFIC PLATE
Pacific Ocean
YAKUTAT PLATE
GULF OF ALASKA
KF
TF
INF
HCF
MF
ARSZ
DF
FF
CMF
TKF
T-TF
EKF
LCF
FT
YTT
WT
AT
TT
GT
PT
CT
YT
−180° −175° −170° −165° −160° −155° −150° −145° −140°
64° 60° 56° 52°
Major Strike-Slip faults
Subduction Zone
COST wells
Late Cenozoic Volcanic Field
Beringian Margin
M 7.9 Earthquake
Wrench faults
Study area
TERRANE LEGEND
Central Composite Terrane (CCT)
FT - Fareweather Terrane
Yukon Composite Terrane (YCT)
YTT - Yukon Tanana Terrane
Oceanic Composite Terrane (OCT)
GT - Goodnews Terrane
Togiak- Koyukuk Composite Terrane (TCT)
TT - Togiak Terrane
Wrangellia Composite Terrane (WCT)
PT - Peninsular Terrane
WT - Wrangellia Terrane
AT - Alexander Terrane
Southern Margin Composite Terrane (SMCT)
CT - Chugach Terrane
YT - Yakutat Terrane
Alaska Range Suture Zone (ARSZ)
Kahiltna Flysch

Figure 2.

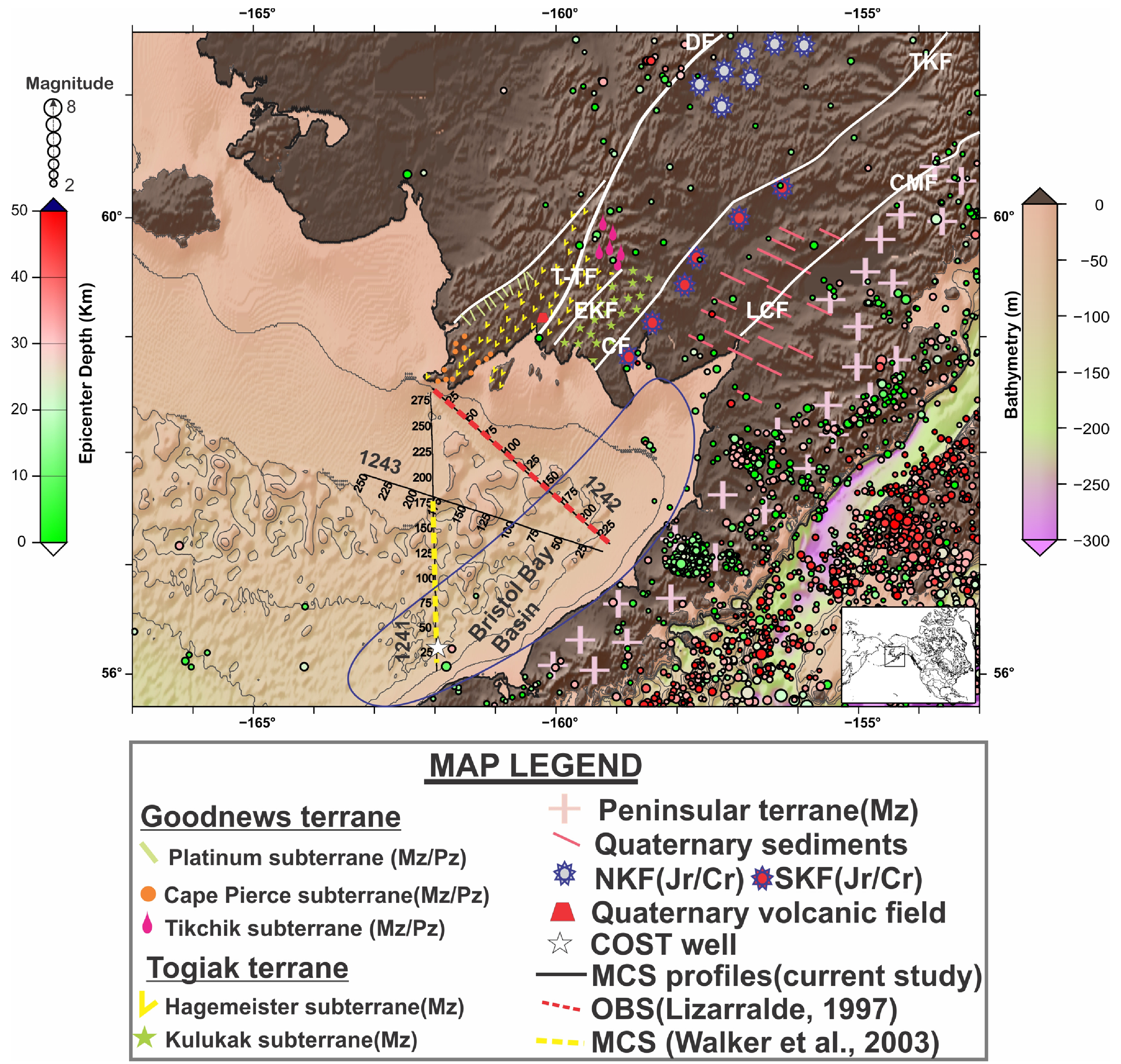
Magnitude
8
2
Epicenter Depth (Km)
0
10
20
30
40
50
Bathymetry (m)
0
−50
−100
−150
−200
−250
−300
−165°
−160°
−155°
60°
56°
DF
TKF
CMF
T-TF
EKF
CF
LCF
1243
1242
1241
Bristol Bay
Basin
MAP LEGEND
Goodnews terrane
Platinum subterrane (Mz/Pz)
Cape Pierce subterrane(Mz/Pz)
Tikchik subterrane (Mz/Pz)
Togiak terrane
Hagemeister subterrane(Mz)
Kulukak subterrane(Mz)
Peninsular terrane(Mz)
Quaternary sediments
NKF(Jr/Cr) SKF(Jr/Cr)
Quaternary volcanic field
COST well
MCS profiles(current study)
OBS(Lizarralde, 1997)
MCS (Walker et al., 2003)

Figure 3.

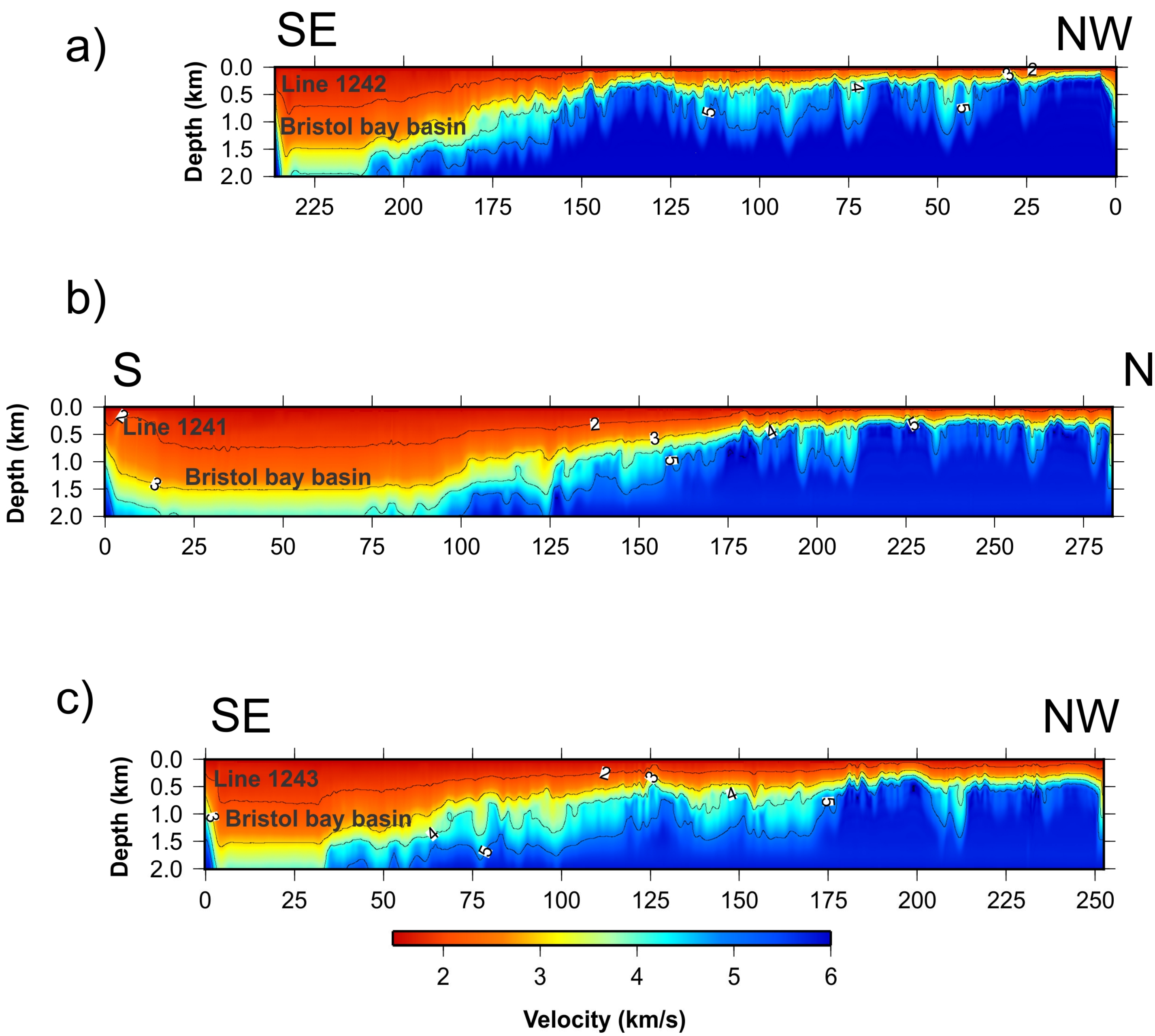

a)
SE
NW
Line 1242
Bristol bay basin
Depth (km)
0.0
0.5
1.0
1.5
2.0
225
200
175
150
125
100
75
50
25
0
b)
S
N
Line 1241
Bristol bay basin
Depth (km)
0.0
0.5
1.0
1.5
2.0
0
25
50
75
100
125
150
175
200
225
250
275
c)
SE
NW
Line 1243
Bristol bay basin
Depth (km)
0.0
0.5
1.0
1.5
2.0
0
25
50
75
100
125
150
175
200
225
250
2
3
4
5
6
Velocity (km/s)

Figure 4.

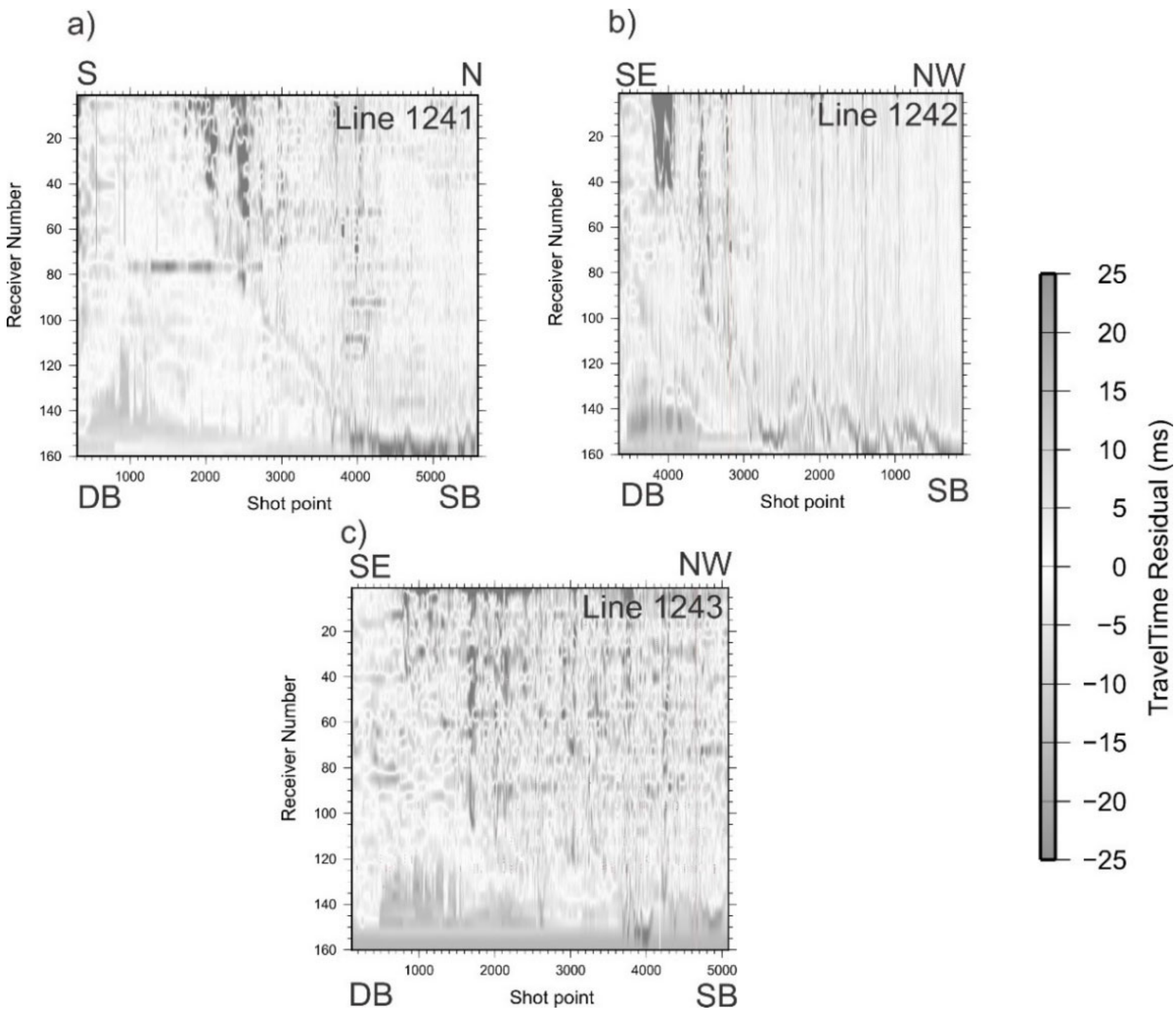
a)
S
N
Line 1241
Receiver Number
Shot point
DB
SB
b)
SE
NW
Line 1242
Receiver Number
Shot point
DB
SB
c)
SE
NW
Line 1243
Receiver Number
Shot point
DB
SB
TravelTime Residual (ms)

Figure 5.

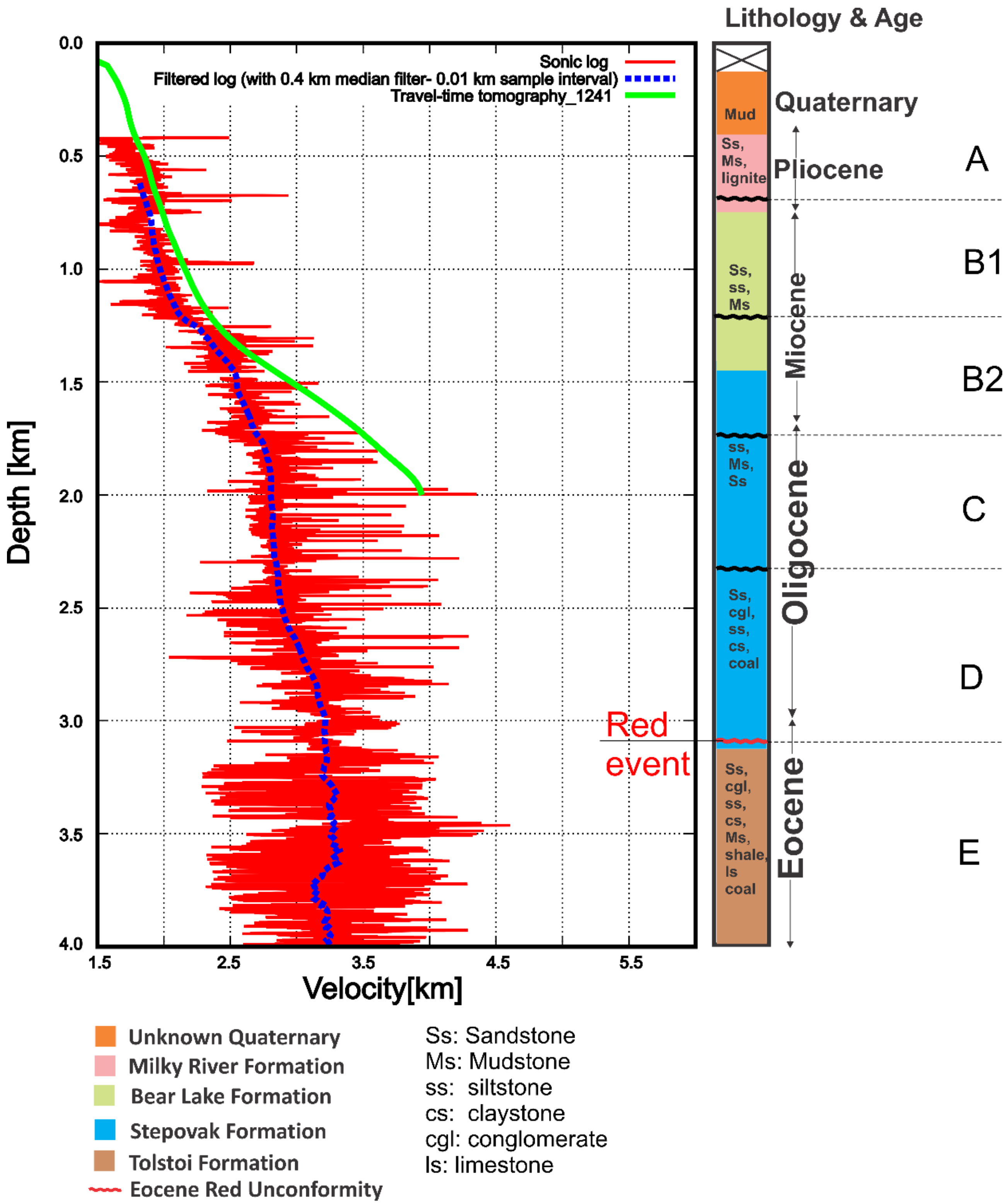

Lithology & Age
Sonic log
Filtered log (with 0.4 km median filter- 0.01 km sample interval)
Travel-time tomography_1241
Depth [km]
Velocity[km]
Mud
Ss, Ms, lignite
Ss, ss, Ms
ss, Ms, Ss
Ss, cgl, ss, cs, coal
Ss, cgl, ss, cs, Ms, shale, ls coal
Quaternary
Pliocene
Miocene
Oligocene
Eocene
A
B1
B2
C
D
E
Red event
Unknown Quaternary
Milky River Formation
Bear Lake Formation
Stepovak Formation
Tolstoi Formation
Eocene Red Unconformity
Ss: Sandstone
Ms: Mudstone
ss: siltstone
cs: claystone
cgl: conglomerate
ls: limestone

Figure 6.

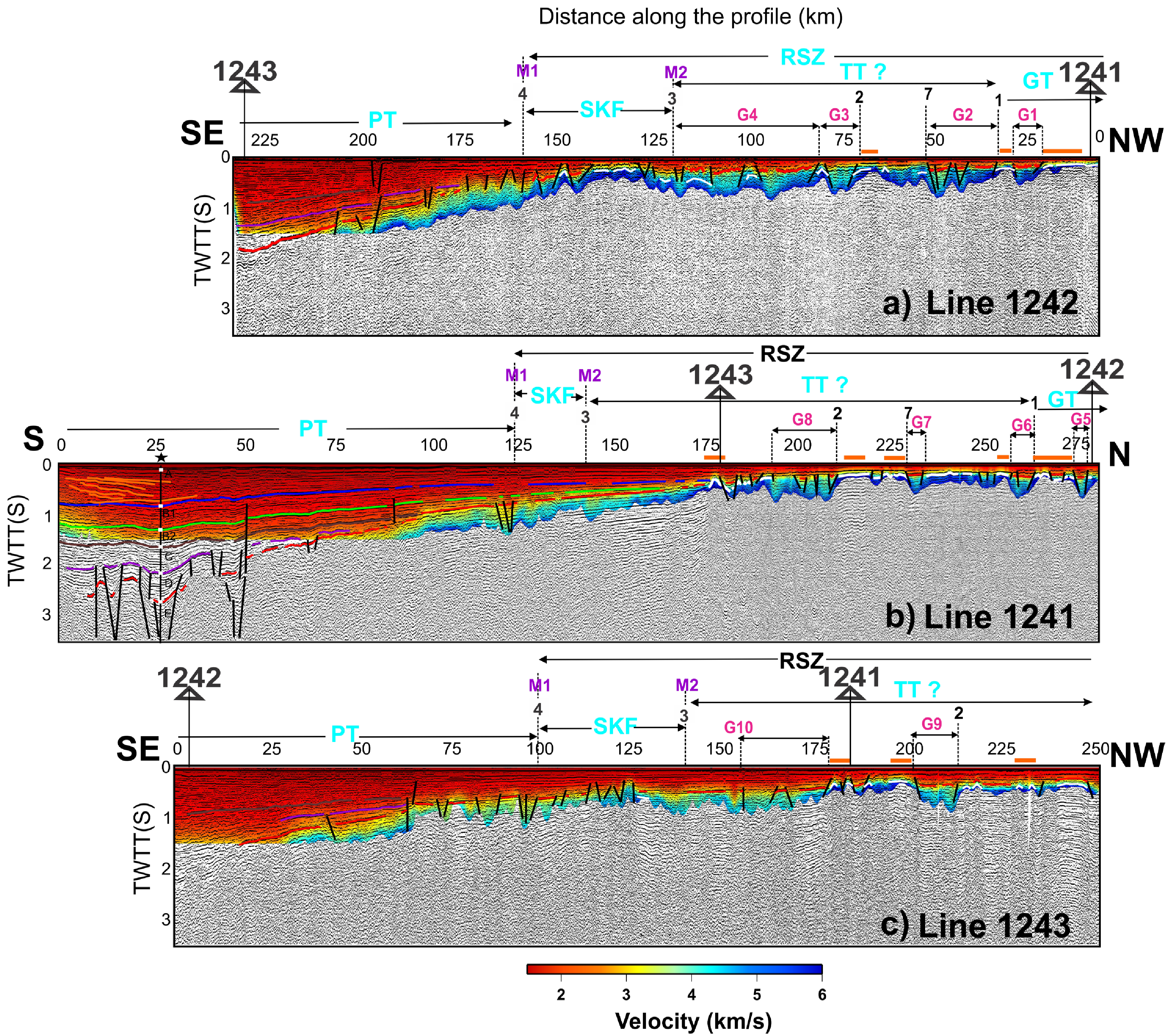

Distance along the profile (km)
a) Line 1242
b) Line 1241
c) Line 1243
TWTT(S)
SE
NW
S
N
1241
1242
1243
RSZ
PT
SKF
TT ?
GT
M1
M2
G1
G2
G3
G4
G5
G6
G7
G8
G9
G10
Velocity (km/s)

Figure 7.

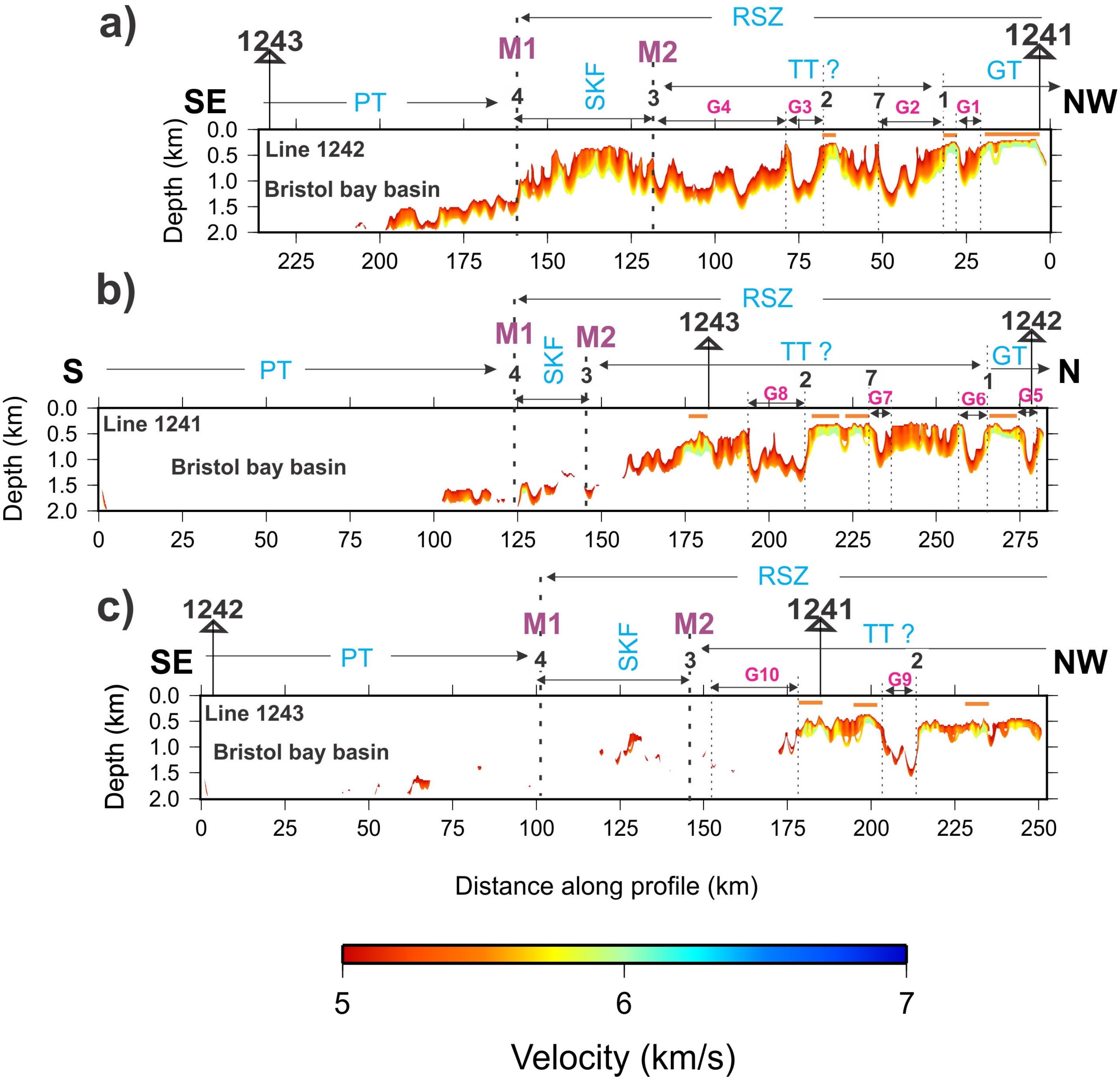
a)
RSZ
1243
M1
M2
TT ?
1241
GT
SE
PT
SKF
4
3
G4
G3
2
7
G2
1
G1
NW
Depth (km)
0.0
0.5
1.0
1.5
2.0
Line 1242
Bristol bay basin
225
200
175
150
125
100
75
50
25
0
b)
RSZ
M1
M2
1243
1242
S
PT
SKF
TT ?
GT
N
4
3
2
7
1
G8
G7
G6
G5
Depth (km)
Line 1241
Bristol bay basin
0
25
50
75
100
125
150
175
200
225
250
275
c)
RSZ
1242
M1
M2
1241
TT ?
SE
PT
SKF
NW
4
3
2
G10
G9
Depth (km)
Line 1243
Bristol bay basin
0
25
50
75
100
125
150
175
200
225
250
Distance along profile (km)
5
6
7
Velocity (km/s)

Figure 8.

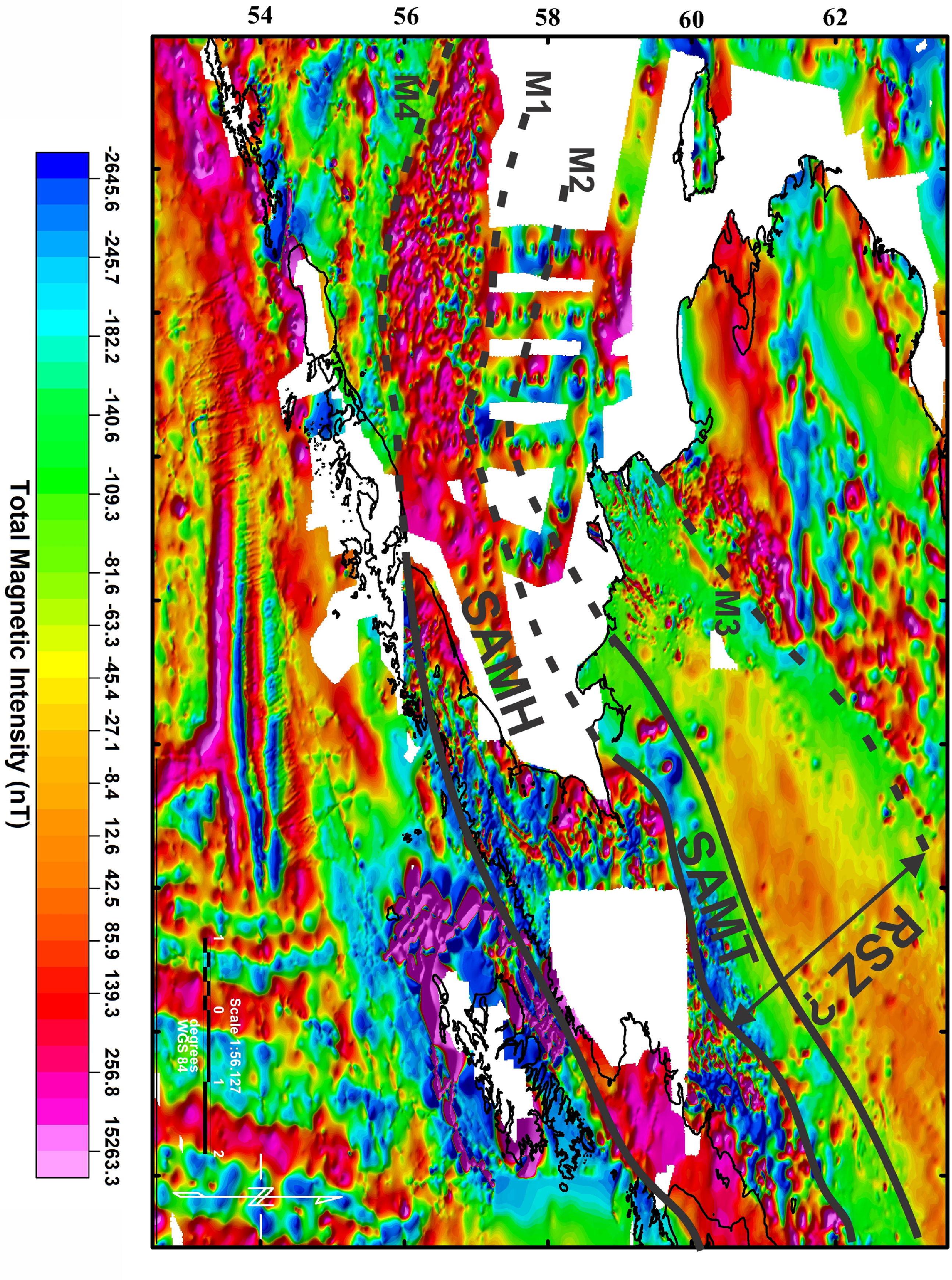
Total Magnetic Intensity (nT)
-2645.6
-245.7
-182.2
-140.6
-109.3
-81.6
-63.3
-45.4
-27.1
-8.4
12.6
42.5
85.9
139.3
256.8
15263.3
54
56
58
60
62
-166
-164
-162
-160
-158
-156
-154
-152
M1
M2
M3
M4
SAMH
SAMT
RSZ ?
Scale 1:56,127
degrees
WGS 84

Figure 9.

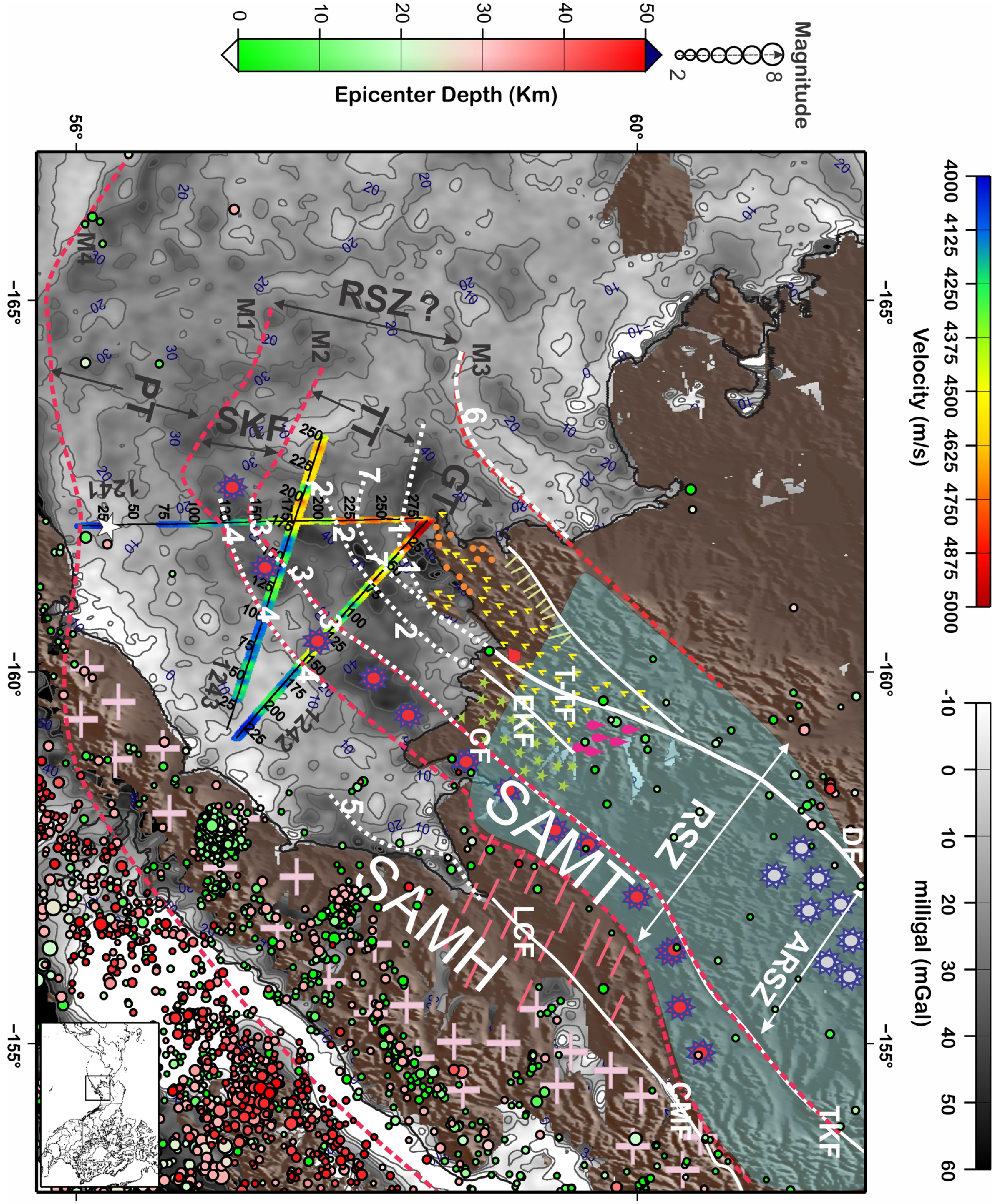

Magnitude
2
8
Epicenter Depth (Km)
0
10
20
30
40
50
Velocity (m/s)
4000
4125
4250
4375
4500
4625
4750
4875
5000
milligal (mGal)
-10
0
10
20
30
40
50
60
56°
60°
−165°
−160°
−155°
RSZ ?
M1
M2
M3
M4
PT
SKF
TT
GT
T-TF
EKF
CF
LCF
CMF
SAMT
SAMH
RSZ
ARSZ
DF
TKF
1241
1242
1243

Figure 10.

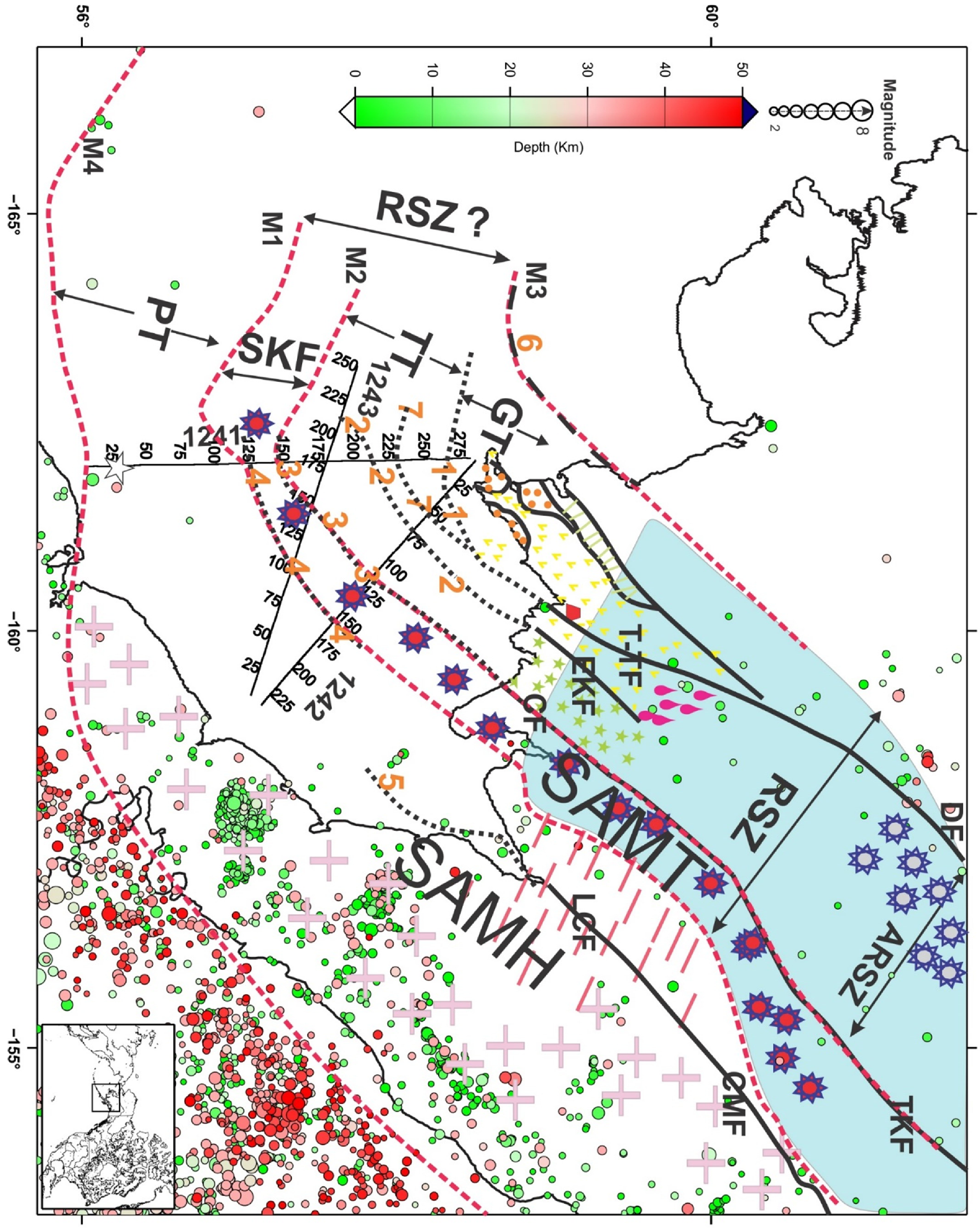

Magnitude
8
2
Depth (Km)
0
10
20
30
40
50
56°
60°
-165°
-160°
-155°
RSZ ?
M1
M2
M3
M4
PT
SKF
TT
GT
1241
1242
1243
SAMT
SAMH
RSZ
ARSZ
DF
TKF
CMF
LCF
CF
EKF
T-AF

Figure A1.

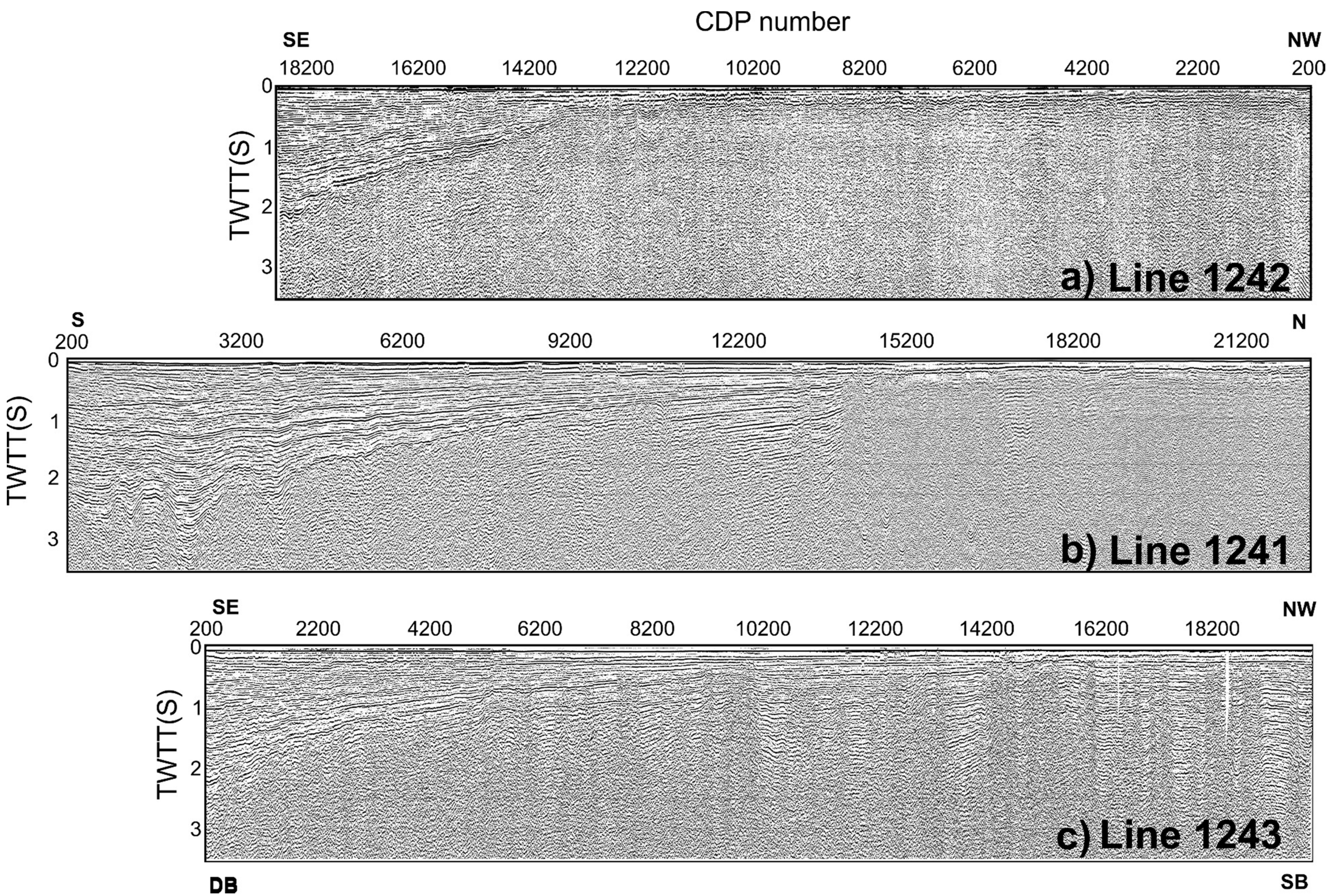
CDP number
SE
NW
18200 16200 14200 12200 10200 8200 6200 4200 2200 200
TWTT(S)
0 1 2 3
a) Line 1242
S
N
200 3200 6200 9200 12200 15200 18200 21200
TWTT(S)
0 1 2 3
b) Line 1241
SE
NW
200 2200 4200 6200 8200 10200 12200 14200 16200 18200
TWTT(S)
0 1 2 3
c) Line 1243
DB
SB

Figure A2.

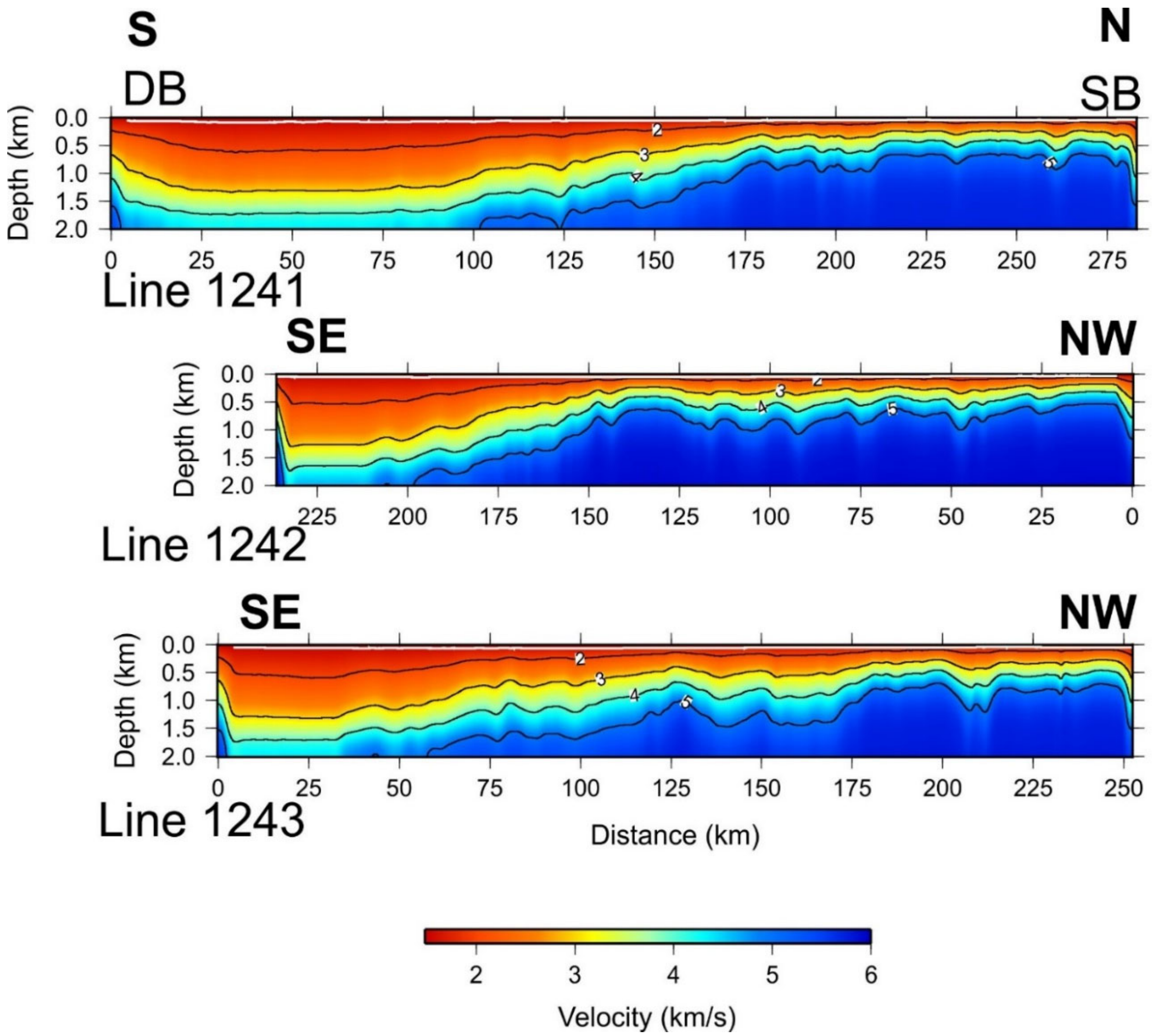
S
N
DB
SB
Depth (km)
Line 1241
SE
NW
Line 1242
SE
NW
Line 1243
Distance (km)
Velocity (km/s)

Figure A3.

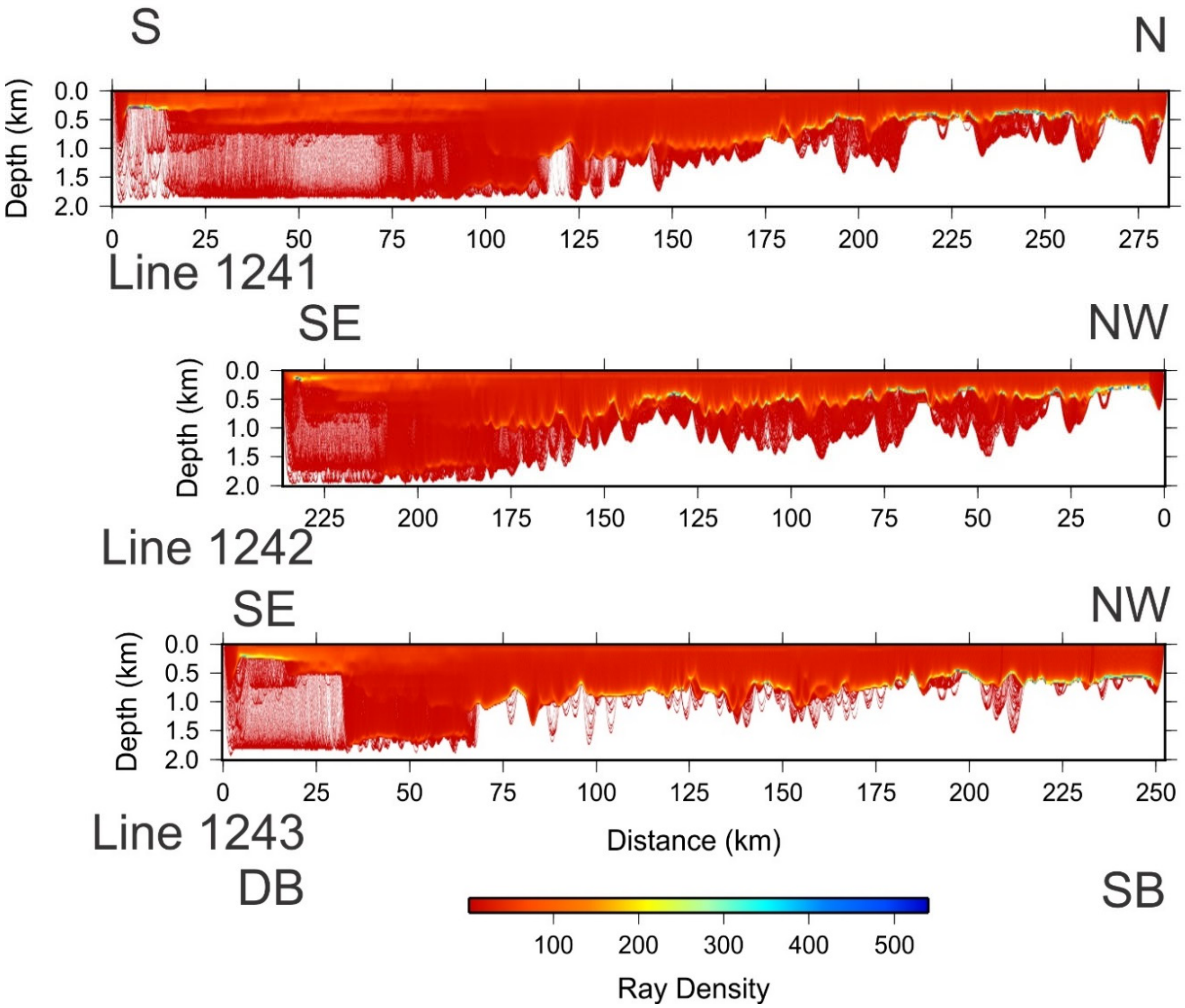
S
N
Depth (km)
0.0
0.5
1.0
1.5
2.0
0
25
50
75
100
125
150
175
200
225
250
275
Line 1241
SE
NW
225
200
175
150
125
100
75
50
25
0
Line 1242
SE
NW
Line 1243
Distance (km)
DB
SB
100
200
300
400
500
Ray Density

Figure A4.

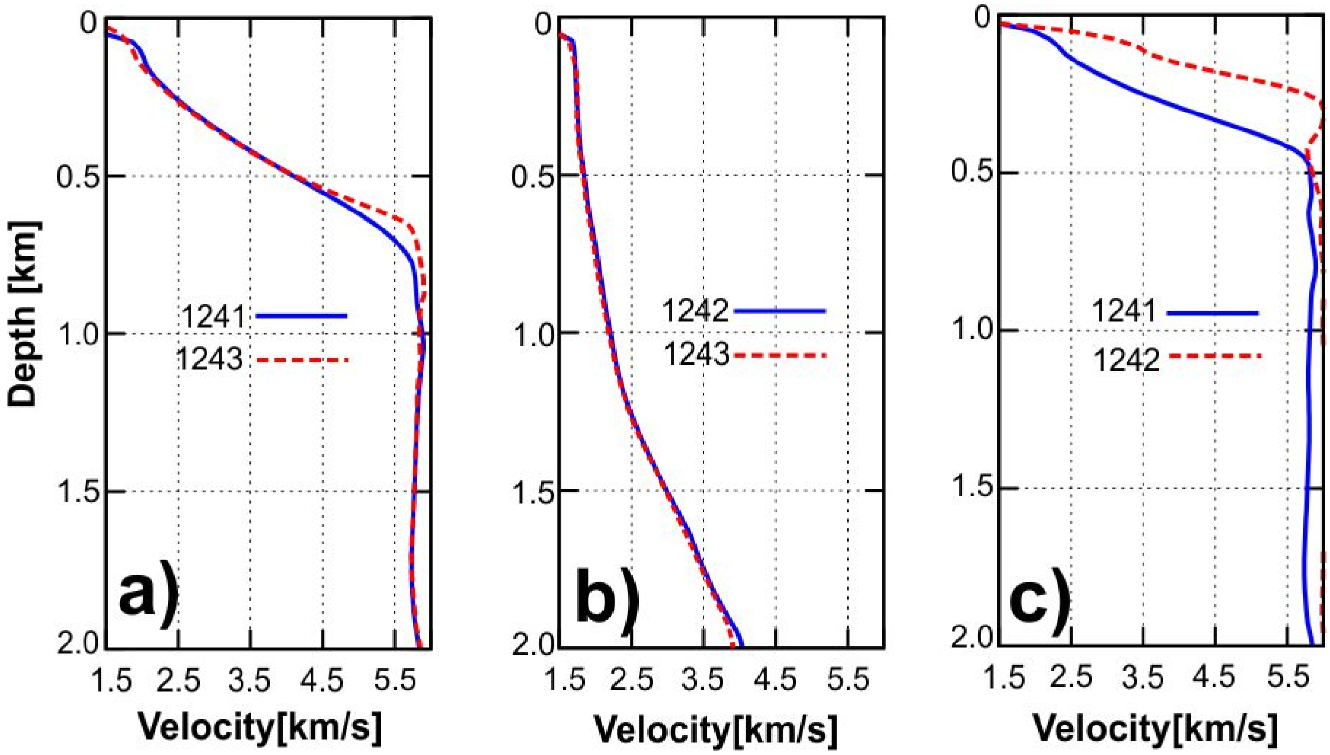

Depth [km]
0
0.5
1.0
1.5
2.0
1241
1243
a)
1.5
2.5
3.5
4.5
5.5
Velocity[km/s]
1242
1243
b)
Velocity[km/s]
1241
1242
c)
Velocity[km/s]

Figure A5.

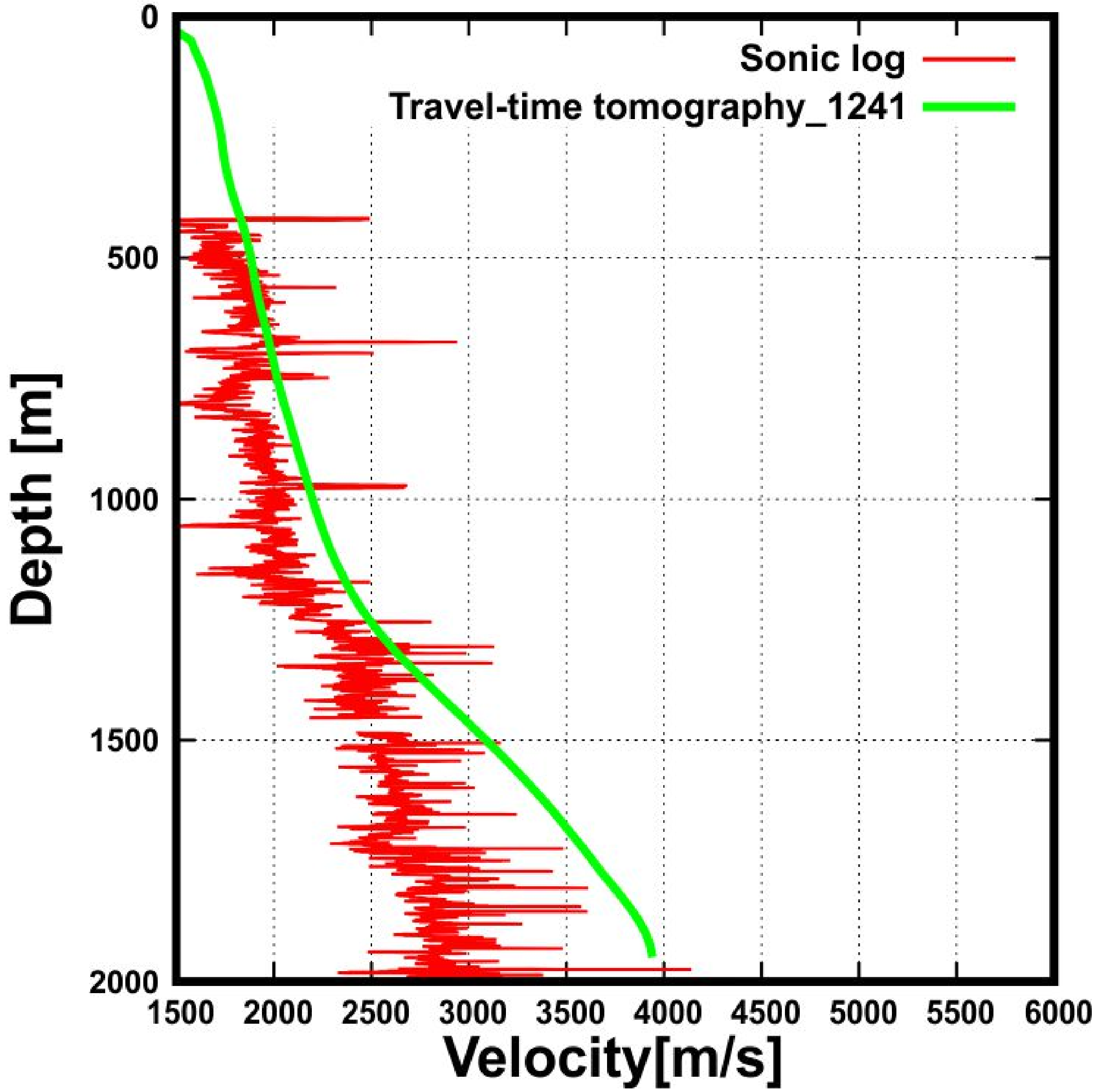

Sonic log
Travel-time tomography_1241
Depth [m]
0
500
1000
1500
2000
1500
2000
2500
3000
3500
4000
4500
5000
5500
6000
Velocity[m/s]

Figure A6.

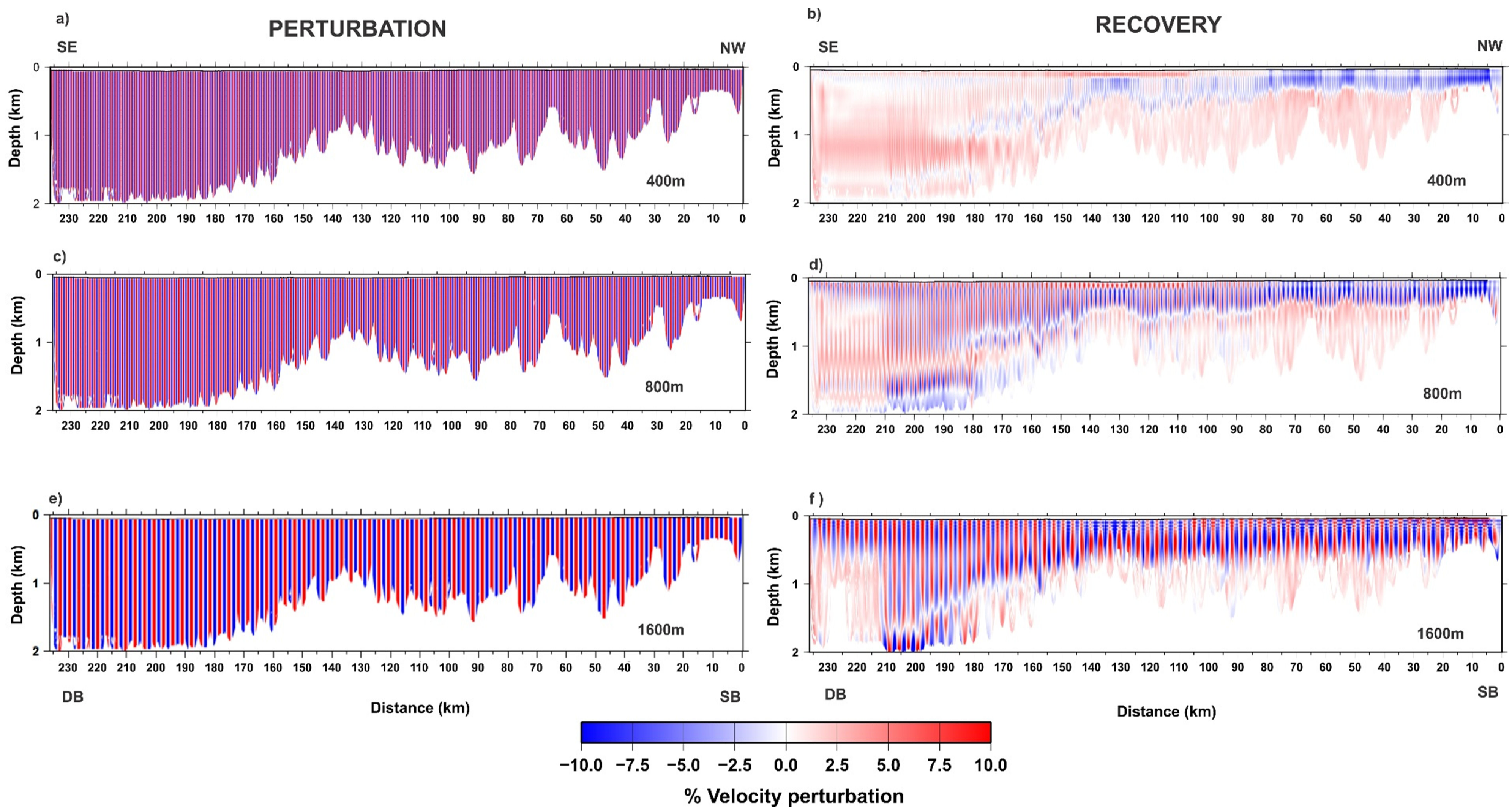
PERTURBATION
RECOVERY
a)
b)
c)
d)
e)
f)
SE
NW
DB
SB
Depth (km)
Distance (km)
400m
800m
1600m
% Velocity perturbation

Figure A7.

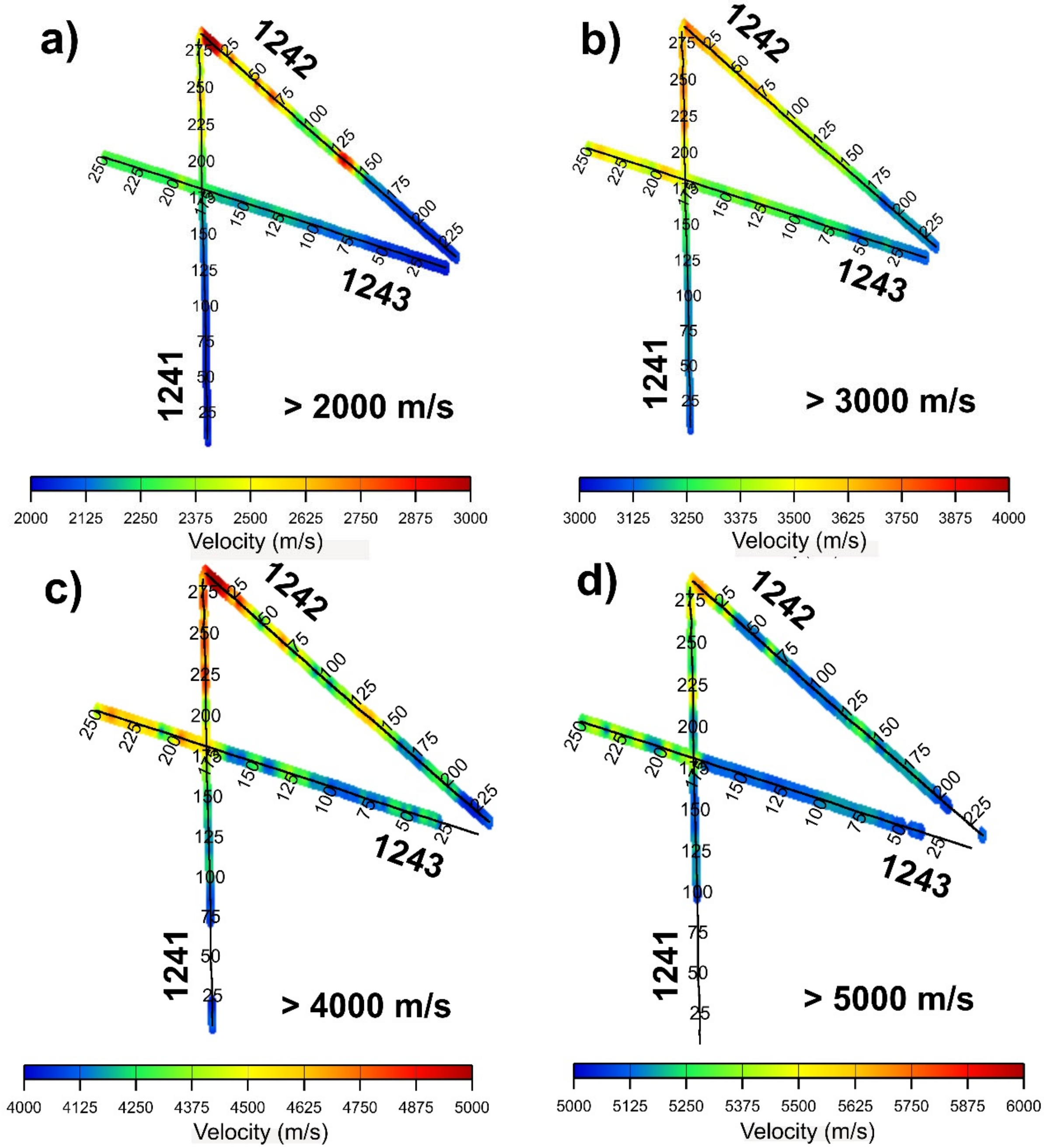
a)
1242
1243
1241
> 2000 m/s
Velocity (m/s)
b)
1242
1243
1241
> 3000 m/s
Velocity (m/s)
c)
1242
1243
1241
> 4000 m/s
Velocity (m/s)
d)
1242
1243
1241
> 5000 m/s
Velocity (m/s)

Figure A8.

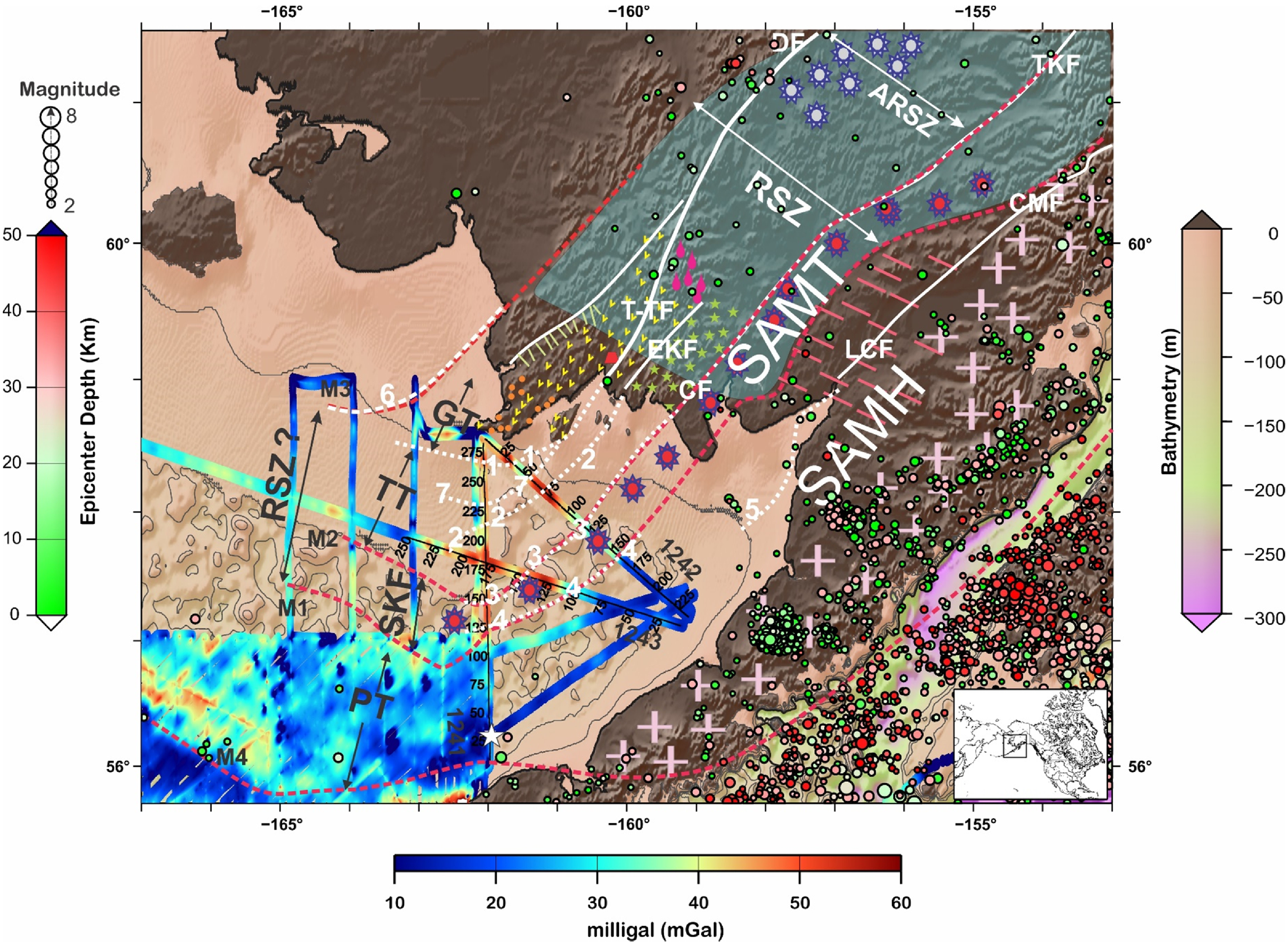
Magnitude
8
2
Epicenter Depth (Km)
0
10
20
30
40
50
−165°
−160°
−155°
60°
56°
RSZ ?
M1
M2
M3
M4
TT
GT
SKF
PT
1241
1242
1243
T-TF
EKF
CF
SAMT
SAMH
LCF
RSZ
ARSZ
DF
TKF
CMF
Bathymetry (m)
0
−50
−100
−150
−200
−250
−300
milligal (mGal)
10
20
30
40
50
60

Figure A9.

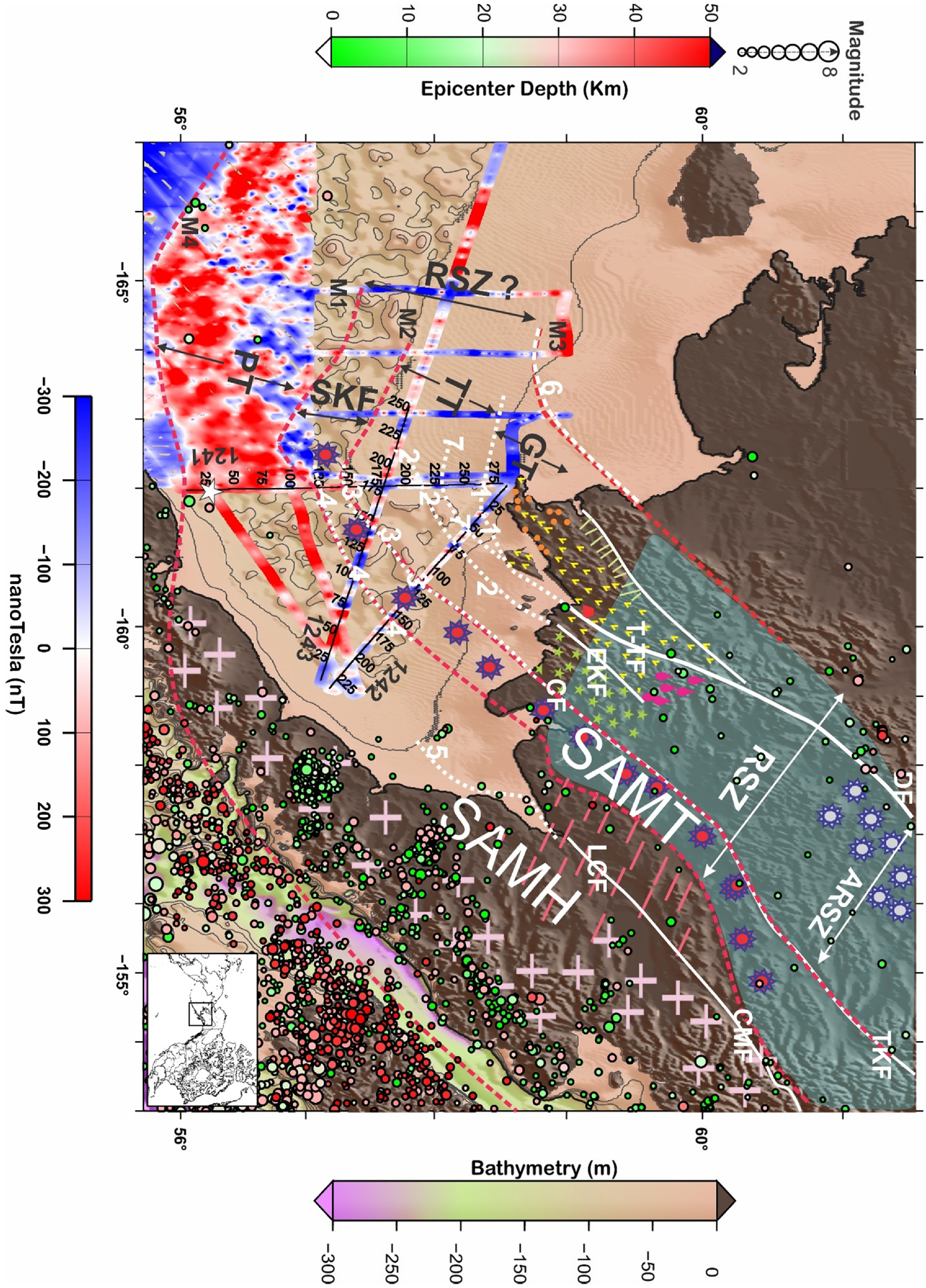

Magnitude
Epicenter Depth (Km)
nanoTesla (nT)
Bathymetry (m)
SAMT
SAMH
RSZ
ARSZ
RSZ ?
PT
SKF
TT
GT
DF
TKF
CMF
LCF
CF
EKF
T-TF
M1
M2
M3
M4
1241
1242
1243